Tests of the standard electroweak model at the energy frontier

John D. Hobbs*

Department of Physics and Astronomy, State University of New York, Stony Brook, New York 11794, USA

Mark S. Neubauer† and Scott Willenbrock‡

Department of Physics, University of Illinois at Urbana-Champaign, Urbana, Illinois, 61801, USA

(published 25 October 2012)

In this review, tests of standard electroweak (EW) theory at the highest available energies as a precursor to the Large Hadron Collider (LHC) era are summarized. The primary focus is on the published results (as of March 2010) from proton-antiproton collisions at $\sqrt{s} = 1.96$ TeV at the Fermilab Tevatron collected using the CDF and D0 detectors. After presenting an overview of the EW sector of the standard model, a summary of experimental tests of EW theory as of March 2010 is provided. These include gauge boson properties and self-couplings, tests of EW physics from the top-quark sector, and searches for the Higgs boson.

DOI: 10.1103/RevModPhys.84.1477 PACS numbers: 12.15.Ji, 13.85.Rm, 14.70.Fm, 14.70.Hp

CONTENTS

I. INTRODUCTION

The goal of particle physics is to explain the nature of the Universe at its most fundamental level, including the basic constituents of matter and their interactions. The standard model (SM) of particle physics is a quantum field theory based on the $SU(3)_C \otimes SU(2)_L \otimes U(1)_Y$ gauge symmetry group which describes the strong, weak, and electromagnetic (EM) interactions among fundamental particles. This theory has been the focus of intense scrutiny by experimental physicists, most notably at high-energy particle colliders, over the last three decades. It has been demonstrated to accurately describe fundamental particles and their interactions up to $O(100)$ GeV, with the existence of nonzero neutrino masses and mixing being the only known exception. Despite the success of the SM, there are many reasons to believe that the SM is an effective theory which is only valid up to $\sim$1 TeV. Some of the shortcomings of the SM will be described in Sec II.

Particle physics is embarking on a unique, and possibly defining, period in its history with the start of particle collisions at the Large Hadron Collider (LHC) at CERN. At the LHC, bunches of protons will be collided with a planned 14 TeV of center-of-mass energy, creating conditions that existed only a small fraction of a second after the big bang. This is 7 times the center-of-mass energy of collisions at the Fermilab Tevatron. For the first time, physicists will be able to directly probe the TeV energy scale in the laboratory, where new physics beyond the SM, with the potential to revolutionize our understanding of the Universe, could be apparent. We can only speculate about what form this will take. It is a tantalizing prospect that on the horizon is a revolution in our understanding of the Universe that includes a more complete

*John.Hobbs@stonybrook.edu
†msn@illinois.edu
‡willen@illinois.edu

theory of particles and their interactions which may explain dark matter and dark energy.

The purpose of this review is to present tests of the electroweak (EW) sector of the SM $[SU(2)_L \otimes U(1)_Y]$ at the highest available energies as a precursor to the LHC era. Our focus is on published results from collider data collected using the CDF (Aaltonen *et al.*, 2007a) and D0 (Abazov *et al.*, 2006a) detectors during Run II at the Fermilab Tevatron as it relates to our understanding of electroweak interactions and spontaneous symmetry breaking. After an overview of electroweak theory (Sec. II), we present current results on gauge boson properties and self-couplings (Sec. III), tests of electroweak physics from top-quark physics (Sec. IV), and searches for the Higgs boson (Sec. V).

II. OVERVIEW

The SM is an extremely successful theory of the strong, weak, and electromagnetic interactions. It is based on three generations of quarks and leptons, interacting via an $SU(3)_C \otimes SU(2)_L \otimes U(1)_Y$ gauge symmetry. The $SU(2)_L \otimes U(1)_Y$ symmetry is spontaneously broken to electromagnetism, $U(1)_{EM}$, by the vacuum-expectation value of the Higgs field. Given this field content and gauge symmetry, the most general theory that follows from writing down every term of dimension four or less is the SM.

In the SM, as usually understood, neutrinos are exactly massless, and do not mix. Since neutrino mixing has been definitively observed, we must go beyond the SM in order to describe this phenomenon. There are two ways to do this. One way is to extend the field content of the model by adding additional fermion and/or Higgs fields (e.g., a right-handed neutrino or a Higgs triplet). The other way is to extend the SM by adding operators of dimensionality greater than four. There is only one operator of dimension five allowed by the gauge symmetries (Weinberg, 1979),

$$\mathcal{L}_5 = \frac{c^{ij}}{\Lambda}(L^{iT}\epsilon\phi)C(\phi^T\epsilon L^j) + \text{H.c.}, \tag{1}$$

where L^i is the lepton doublet field of the ith generation and ϕ is the Higgs-doublet field [the 2×2 matrix ϵ and the 4×4 charge-conjugation matrix C are present to ensure invariance under $SU(2)_L$ and Lorentz transformations, respectively]. When the Higgs doublet acquires a vacuum-expectation value $\langle\phi\rangle = (0, v/\sqrt{2})$ ($v = 246$ GeV), this term gives rise to a (Majorana) mass for neutrinos,

$$\mathcal{L}_5 = -\tfrac{1}{2}M_\nu^{ij}\nu^{iT}C\nu^j + \text{H.c.} \tag{2}$$

where $M_\nu^{ij} = c^{ij}v^2/\Lambda$ is the neutrino mass matrix. Because of the small inferred masses of neutrinos, the scale Λ lies around 10^{15} GeV, assuming c^{ij} is not much less than order unity.

There are other indications that the SM is not a complete description of nature, most of them related to gravitation and cosmology. Even with massive neutrinos included, the SM particles only constitute 4.6% of the present Universe, with the remainder in mysterious dark matter (23%) and dark energy (72%). Neither dark matter nor dark energy are accommodated in the SM. There is no adequate mechanism for baryogenesis (the observed excess of baryons over antibaryons) or inflation, which is the simplest explanation of the observed temperature fluctuations in the cosmic microwave background. The SM also provides no explanation of the strong CP problem: the lack of observed CP violation in the strong interaction, which is allowed by the SM.

If physics beyond the SM lies at an energy scale less than 1 TeV, then we should be able to observe it directly at high-energy colliders. If it lies at a scale greater than 1 TeV, then we can parametrize its effects via higher-dimension operators, suppressed by inverse powers of the scale of new physics Λ exactly as in the case of neutrino masses described above. Other than the dimension-five operator responsible for neutrino masses, the lowest-dimension operators are of dimension six, and are therefore suppressed by two inverse powers of Λ. If Λ is of order 10^{15} GeV, as suggested by neutrino masses, then these operators are so suppressed that they are unobservable, with the possible exception of baryon-number violating operators that mediate nucleon decay. However, there could be more than one scale of new physics, and if this scale is not much greater than 1 TeV, its effects could be observable via dimension-six operators. Operators of a dimension greater than six are suppressed by even more inverse powers of Λ and can be neglected.

There are many dimension-six operators allowed by the SM gauge symmetry (Buchmuller and Wyler, 1986). There are three ways to detect the presence of these operators. The first is to observe phenomena that are absolutely forbidden (or extremely suppressed) in the SM, such as nucleon decay. The second is to make measurements with such great precision that the small effects of the dimension-six operators manifest themselves. The third is to do experiments at such high energy E that the effects of these operators, of order $(E/\Lambda)^2$, become large. If $E > \Lambda$, then one must abandon this formalism, because operators of arbitrarily high dimensionality become significant; however, the new physics should then be directly observable. If no effects beyond the SM are observed, then one can place bounds on the coefficients of the dimension-six operators c/Λ^2, where c is a dimensionless number. These bounds apply only to the product c/Λ^2, not to c and Λ^2 separately; in fact, there could even be two different scales of new physics involved ($\Lambda_1\Lambda_2$ in place of Λ^2).

This approach to physics beyond the SM, dubbed an effective-field-theory approach (Weinberg, 1979), has the advantage of being model independent. Whatever new physics lies at the scale Λ, it will induce dimension-six operators, whose only dependence on the new physics lies in their coefficients, c/Λ^2. Another advantage of this approach is that it is universal; it can be applied to both tree-level and loop-level processes, and any ultraviolet divergences that appear in loop processes can be absorbed into the coefficients of the operators. Thus, one need not make any *ad hoc* assumptions about how the ultraviolet divergences are cut off. This effective-field-theory approach thus provides an excellent framework to parametrize physics beyond the SM (De Rujula *et al.*, 1992; Hagiwara *et al.*, 1993).

Hadron colliders contribute to the study of the electroweak interactions in three distinct ways. First, because they operate at the energy frontier, hadron colliders are uniquely suited to searching for the effects of dimension-six operators that are

suppressed by a factor of $(E/\Lambda)^2$. Second, they are able to contribute to the precision measurement of a variety of electroweak processes, most notably to the measurement of the W boson mass and the top-quark mass. Third, they are able to search for new particles associated with the electroweak interactions, in particular, the Higgs boson. These three virtues of hadron colliders will manifest themselves throughout this review.

A. Electroweak interactions

The electroweak theory is a spontaneously broken gauge theory based on the gauge group $\mathrm{SU(2)_L} \otimes U(1)_Y$. There are three parameters that describe the theory: the gauge couplings g and g', and the order parameter of spontaneous symmetry breaking v. In the SM, this order parameter is the vacuum-expectation value of a fundamental Higgs field. These parameters are not measured directly, but rather inferred from precision electroweak measurements. The three measurements that are used to fix these parameters are the Fermi constant G_F determined from the muon lifetime formula; the fine-structure constant α, determined from a variety of low-energy experiments; and the Z boson mass M_Z. With these three inputs, the predictions of all other electroweak processes can be calculated, at least at tree level.

The level of precision of electroweak measurements is such that a tree-level analysis is insufficient, and one must go to at least one loop. At this level, one finds that predictions depend also on the top-quark mass and the Higgs-boson mass, since these particles appear in loops. In fact, a range for the top-quark mass was correctly predicted by precision electroweak data before the top quark was discovered, and the measured mass falls into this range. We are now following the same tack with the Higgs boson. Remarkably, the precision electroweak data imply that the Higgs-boson mass is not far above the experimental lower bound of $m_H > 114\ \mathrm{GeV}/c^2$, which means that it may be accessible at the Tevatron as well as the LHC.

The electroweak interaction has many other parameters as well. Along with the top-quark mass, there are the masses of all the other quarks and leptons, as well as the elements of the Cabbibo-Kobayashi-Maskawa (CKM) quark-mixing matrix and the Maki-Nakagawa-Sakata lepton-mixing matrix. Most of these mixing parameters are not measured at the energy frontier, with one exception: the CKM element V_{tb} that describes the coupling of a W boson to a top and bottom quark. The only direct measurement of this parameter comes from electroweak production of the top quark at hadron colliders via a process known as single-top production, as discussed in Sec. IV.C.

B. Electroweak symmetry breaking

The strong and electroweak forces are gauge theories, based on the groups $\mathrm{SU(3)}_C$ and $\mathrm{U(1)_{EM}}$, respectively. The associated gauge bosons, the gluon and the photon, are massless as a consequence of the gauge symmetry. We know that the interactions of electroweak bosons with fermions as well as with themselves are also governed by a gauge theory, with gauge group $\mathrm{SU(2)_L} \otimes \mathrm{U(1)}_Y$. Why, then, are the electroweak bosons $W^{\pm}$ and Z not massless, as would be expected of gauge bosons? In the SM, the answer is that the electroweak symmetry is spontaneously broken, and that the electroweak gauge bosons acquire mass through the Higgs mechanism. This is the most plausible explanation of why the interactions appear to be those of a gauge theory, despite the fact that the gauge bosons are not massless. However, this argument leaves completely open the question of how (and why) the electroweak symmetry is broken.

The simplest model of electroweak symmetry breaking, which is also the original proposal, is based on a fundamental scalar field that is an electroweak doublet carrying hypercharge $Y = 1/2$. The potential for this scalar field is chosen such that its minimum is at nonzero field strength. This breaks the electroweak symmetry to $\mathrm{U(1)_{EM}}$, as desired. This simple model, which can be criticized on several grounds, has withstood the test of time. It predicts that there is a scalar particle, dubbed the Higgs boson, of unknown mass but with definite couplings to other particles. The discovery of this Higgs particle is one of the driving ambitions of particle physicists, and was a primary motivation for the LHC.

As mentioned in Sec. II.A, this simple model is consistent with precision electroweak data with a Higgs particle close to the present experimental lower bound of $m_H > 114\ \mathrm{GeV}/c^2$. This consistency does not rule out more exotic possibilities, however, such as two (or more) Higgs doublets, Higgs singlets and triplets, composite Higgs bosons, and other alternative models of electroweak symmetry breaking.

III. ELECTROWEAK GAUGE BOSONS

In the SM, the W and Z bosons mediate the weak force and acquire mass through the Higgs mechanism, as described in Sec. II. The W boson was discovered in 1983 in $p\bar{p}$ collisions at the CERN Super Proton Synchrotron by the UA1 and UA2 experiments (Arnison *et al.*, 1983a; Banner *et al.*, 1983), with discovery of the Z boson soon to follow (Arnison *et al.*, 1983b; Bagnaia *et al.*, 1983). The discovery of these gauge bosons at CERN represents a dramatic validation of Glashow-Salam-Weinberg theory which predicted the existence of neutral currents mediated by a new gauge boson, the Z boson, and predicted the W bosons to describe nuclear β decay and, together with the massless photon, these comprise the gauge bosons of the electroweak interaction. High precision studies of the Z boson properties made by the LEP collaborations and the SLD Collaboration (Abbiendi *et al.*, 2006b) using e^+e^- collisions provided stringent tests of electroweak theory.

The W and Z bosons are copiously produced in $p\bar{p}$ collisions at the Fermilab Tevatron due to their large production cross sections at $\sqrt{s} = 1.96$ TeV and the high integrated luminosity data sets available from the CDF and D0 experiments during Run II. Detailed measurement of the W and Z properties at the Tevatron is not only important to further test Glashow-Salam-Weinberg theory and the electroweak symmetry breaking mechanism in the SM but also to search for new physics beyond the SM using the highest energy collisions currently available. We summarize the current Tevatron measurements of W and Z properties in Sec. III.A–III.D.

The production of heavy vector boson pairs (WW, WZ, and ZZ) is far less common than inclusive W and Z production.

While a W boson is produced in every 3 million $p\bar{p}$ collisions and a Z boson in every 10 million, the production of a WW pair is a once in 6 billion event, WZ a once in 20 billion event, and ZZ a once in 60 billion event. Diboson production is sensitive to the triple gauge couplings (TGCs) between the bosons themselves via an intermediate virtual boson. The boson TGCs are an important consequence of the non-Abelian nature of the SM electroweak gauge symmetry group. At the highest accessible energies available at the Fermilab Tevatron, diboson production provides a sensitive probe of new physics, including anomalous trilinear gauge couplings, new resonances such as the Higgs boson, and large extra dimensions (Kober, Koch, and Bleicher, 2007). Recent results on diboson production from the Tevatron are discussed in Sec. III.E.

A. Heavy gauge boson production

In high-energy proton-antiproton collisions at the Fermilab Tevatron, heavy vector bosons ($V \equiv W, Z$) are produced at tree level via quark-antiquark annihilation ($q\bar{q} \to V$) as shown in Fig. 1. At high transverse momentum,[1] the leading-order QCD subprocesses are $q\bar{q} \to Vg$ and $qg \to Vq$. The production properties of heavy gauge bosons provide tests of perturbative QCD and, under certain circumstances, information about quark and gluon momentum distributions within the proton and antiproton.

The heavy vector boson production cross section in a $p\bar{p}$ collision is given by

$$\sigma(V) = \int \sigma_{0,V} f(x_q) \bar{f}(x_{\bar{q}}) dx_q dx_{\bar{q}}$$

in which $\sigma_{0,V}$ is the cross section for production of a vector boson by a quark, antiquark pair with Feynman x values of x_q and $x_{\bar{q}}$, respectively, and $f(x_q)$ and $\bar{f}(x_{\bar{q}})$ are the parton distribution functions for the proton and antiproton. As defined here, contributions from pure γ^* and Z/γ^* interference terms are not included but are accounted for in comparisons with theory in the measurements we describe.

The remainder of this section includes a summary of current W and Z cross section measurements that the Tevatron and their comparisons with theory. As mentioned, these measurements of W and Z boson production cross sections primarily test QCD rather than electroweak theory. We include them here since detailed study of heavy gauge boson states are central to tests of electroweak theory and, therefore, it is important to consider how well their production in $p\bar{p}$ collisions is understood.

The cross section times branching fraction of W and Z bosons is measured in the fully leptonic decay channels $W \to \ell\nu$ and $Z \to \ell\ell$, where $\ell \equiv e, \mu, \tau$. While the final states involving τ leptons are important for many reasons, we restrict ourselves to the e and μ final states for the cross section discussion since these give the highest precision measurements. The fully leptonic decay channels are chosen over hadronic channels for these measurements, since the latter suffer from large backgrounds to due to the hadronic decay of jets produced by QCD processes.

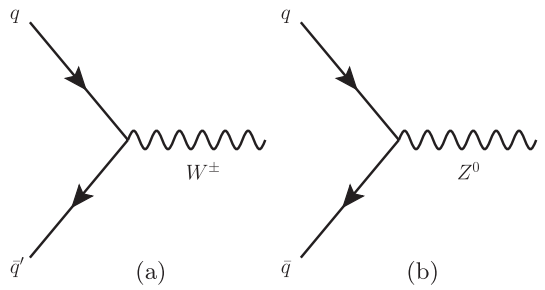

FIG. 1. Leading-order (a) W and (b) Z boson production via quark-antiquark annihilation. The production is dominated by $q = u, d$ valence quarks. The γ^* contribution interferes with the Z diagram but is not shown.

1. W and Z cross sections

Using a next-to-next-to-leading order (NNLO) prediction (Hamberg, van Neerven, and Matsuura, 1991) calculated with the MRST2004 NNLO parton distribution function (Martin *et al.*, 2004) and the SM branching fractions for the W and Z bosons into fully leptonic final states, the cross section times branching fractions are calculated to be

$$\sigma(p\bar{p} \to W) \times B(W \to \ell\nu) = 2687 \pm 54 \text{ pb}$$

and

$$\sigma(p\bar{p} \to Z) \times B(Z \to \ell\ell) = 251.9^{+5.0}_{-11.8} \text{ pb}.$$

The uncertainties are a combination of the MRST2004 uncertainties and the difference between the central value above and that computed using the CTEQ6.1M parton distribution functions (Pumplin *et al.*, 2002).

The W and Z cross sections times branching fractions to fully leptonic final states have been measured by the CDF (Abulencia *et al.*, 2007a) using $\int \mathcal{L} dt = 72$ pb^{-1}. The results for electron and muon channels combined are

$$\sigma(p\bar{p} \to W) \times B(W \to \ell\nu) = 2749 \pm 10(\text{stat}) \pm 53(\text{syst}) \pm 165(\text{lumi}) \text{ pb}$$

and

$$\sigma(p\bar{p} \to Z) \times B(Z \to \ell\ell) = 254.9 \pm 3.3(\text{stat}) \pm 4.6(\text{syst}) \pm 15.2(\text{lumi}) \text{ pb}.$$

The measurements of the Z cross section include additional contributions from $\gamma*$ and $Z/\gamma*$ interference which gives events that are experimentally indistinguishable from the Z process. The size of these contributions depends on the Z/γ^* mass range considered. For the range $60 \leq M(Z/\gamma^*) < 130$ GeV$/c^2$, these contributions increase the cross section by a factor of 1.019 ± 0.001 relative to the Z-only cross section, and for the mass range $66 \leq M(Z/\gamma*) < 116$ GeV$/c^2$, the cross section is increased by a factor of 1.004 ± 0.001.

A precision measurement of the ratio R of W and Z cross section times branching fraction given by

[1]Throughout this paper, "transverse" is taken to be in a plane perpendicular to the beam directions, and unless otherwise noted, quantities with a "T" subscript, e.g., E_T, are values projected onto this plane. Also, charge conjugation is assumed throughout.

TABLE I. The measured integrated luminosity, yield, background, signal acceptance times efficiency, and resulting $\sigma \times \mathrm{Br}$ for each of the four Z cross-section times branching ratio analyses by the CDF Collaboration in Abulencia *et al.* (2007a). The combination of the dielectron and dimuon channels using the BLUE method is also shown. The Z/γ^* results have been corrected to Z only as described in the text.

Channel	Integrated luminosity	Data yield	Predicted background	$A \times \epsilon$	Measured $\sigma \times \mathrm{Br}$
$W \to e\nu$	72 pb^{-1}	37 584	1762 ± 300	$0.1795^{+0.0034}_{-0.0038}$	$2.771 \pm 0.014^{+0.062}_{-0.056} \pm 0.166$ nb
$W \to \mu\nu$	72 pb^{-1}	31 722	3469 ± 151	$0.1442^{+0.0031}_{-0.0034}$	$2.722 \pm 0.015^{+0.066}_{-0.061} \pm 0.163$ nb
$e\nu$ and $\mu\nu$	⋯	⋯	⋯	⋯	$2.749 \pm 0.010 \pm 0.053 \pm 0.165$ nb
$Z \to ee$	72 pb^{-1}	4 242	62 ± 18	$0.2269^{+0.0047}_{-0.0048}$	$255.8 \pm 3.9^{+5.5}_{-5.4} \pm 15.3$ pb
$Z \to \mu\mu$	72 pb^{-1}	1 785	13 ± 13	$0.0992^{+0.0028}_{-0.0031}$	$248.0 \pm 5.9^{+8.0}_{-7.2} \pm 14.8$ pb
ee and $\mu\mu$	⋯	⋯	⋯	⋯	$254.9 \pm 3.3 \pm 4.6 \pm 15.2$ pb

$$R = \frac{\sigma(p\bar{p} \to W) \times B(W \to \ell\nu)}{\sigma(p\bar{p} \to Z) \times B(Z \to \ell\ell)}$$

can be used to test the SM. For example, new high mass resonances decaying to either W or Z bosons could lead to a deviation of the measured value of R from the SM expectation.

Important systematic uncertainties such as the integrated luminosity uncertainty cancel in the measurement of R. The ratio R has been measured by the CDF (Abulencia *et al.*, 2007a) using $\int \mathcal{L} dt = 72$ pb^{-1} to be

$$R = 10.84 \pm 0.15(\mathrm{stat}) \pm 0.14(\mathrm{syst}).$$

This measurement has a precision of 1.9% and is consistent with SM expectation at NNLO of 10.69 ± 0.08 (Hamberg, van Neerven, and Matsuura, 1991).

A summary of the results are shown in Table I. The individual results are in good agreement with each other and with the prediction from theory.

Even with the moderate sample sizes of these measurements, the W and Z cross section results are limited by the systematic uncertainty from the luminosity measurements. Because of this, further improvement in these measurements is not anticipated. CDF and D0 Collaborations continue to use Z-boson production to measure experimental efficiencies acceptances and cross checks on temporal or instantaneous luminosity dependence of detector response. The updated cross section results could be reinterpreted as measurements of the integrated luminosity.

B. W boson mass

At tree level, the W boson mass is fully determined by the electromagnetic fine-structure constant, the weak Fermi coupling, and the cosine of the weak mixing angle. When higher-order EW corrections, like those shown in Fig. 2, are included, the expression is modified to (Sirlin, 1980)

$$M_W^2 = \frac{\hbar^3 \pi \alpha_{EM}}{\sqrt{2} G_F} \frac{1}{(1 - M_W^2/M_Z^2)(1 - \Delta r)}, \tag{3}$$

in which M_W (and later Γ_W) correspond to the parameters of a Breit-Wigner distribution with an s-dependent width. The term Δr includes the effects of radiative corrections and depends on M_t^2 and $\log M_H$, where M_t and M_H are the top-quark and Higgs-boson masses, respectively. Measurement of the W boson mass can be used to constrain the allowed Higgs-boson mass. The precisions of the W boson and top-quark mass measurements are currently the limiting factors in the indirect constraint on the Higgs-boson mass and are shown in Fig. 3. Earlier measurements of the W boson mass have been made by the LEP experiments (Abbiendi *et al.*, 2006a; Achard *et al.*, 2006; Schael *et al.*, 2006; Abdallah *et al.*, 2008) and CDF (Affolder *et al.*, 2001) and D0 (Abazov *et al.*, 2002a) in Run I of the Tevatron.

Signal-to-background and resolution considerations dictate use of the $W \to e\nu$ and $W \to \mu\nu$ decay modes for the W boson mass measurement at the Tevatron. The momentum

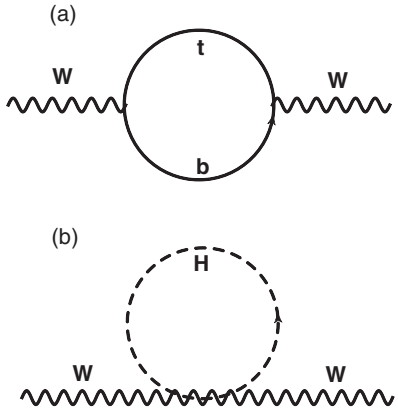

FIG. 2. Feynman diagrams showing corrections to the W boson mass from (a) the top quark and (b) the SM Higgs boson.

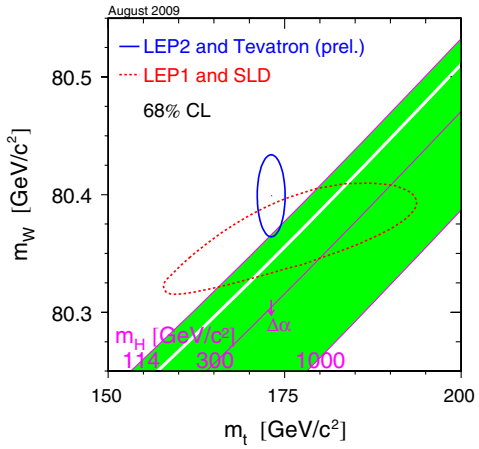

FIG. 3 (color online). The measured top quark and W boson masses and a band of allowed Higgs-boson masses. This includes the recent results summarized in the text. From Alcaraz *et al.*, 2009.

component of the neutrino along the beam direction cannot be inferred in $p\bar{p}$ collision events, so the W invariant mass cannot be reconstructed from its decay products and other variables are used to determine the mass. Three variables are used: (1) the lepton (e or μ) transverse momentum p_T^ℓ, (2) the (inferred) neutrino transverse momentum p_T^ν, and (3) the transverse mass, $m_T \equiv \sqrt{p_T^\ell p_T^\nu [1-\cos(\delta\phi)]}$ in which $\delta\phi$ is the lepton-neutrino opening angle in the plane transverse to the beam. Although these variables are highly correlated, their systematic uncertainties are dominated by different sources, so the results are combined taking their statistical and systematic correlations into account.

The event decay kinematics in the transverse plane are fully characterized by two quantities: (1) the lepton transverse momentum $\vec{p}_T^{\,\ell}$ and (2) the transverse momentum of the hadronic recoil $\vec{u}_T$ required to balance the transverse momentum of the W. The hadronic recoil is defined as the vector sum of all energy measured in the calorimeter excluding that deposited by the lepton. From these two measurements, the neutrino transverse momentum is inferred: $-\vec{p}_T^{\,\nu} = \vec{p}_T^{\,\ell} + \vec{u}_T$. In practice, the recoil is computed using the event transverse missing energy ($\not\!\!E_T$) measured in the calorimeter after removing the contribution to calorimeter energy associated with the lepton. The W boson mass is determined by generating predicted distributions (templates) of the three measurement variables for a range of input W boson mass hypotheses. These are generated using dedicated fast Monte Carlo simulation programs, and the mass is determined by performing a binned maximum likelihood fit of these templates to the distributions observed in data. The Run II measurements use a blinding technique in which an unknown offset is added to the value returned from the fits until the analysis are finished. At that point, the offset is removed to reveal the true value. The results from the different fit variables (p_T^ℓ, p_T^ν, m_T) and final states (e or μ) are combined using the Best Linear Unbiased Estimate (BLUE) algorithm (Lyons, Gibaut, and Clifford, 1988; Valassi, 2003).

Both D0 and CDF reported mass measurements using Run II data. The CDF result (Aaltonen *et al.*, 2007a) uses $\int \mathcal{L}dt = 0.2$ fb^{-1} and results are reported for $W \to e\nu$ and $W \to \mu\nu$ decays. The D0 result (Abazov *et al.*, 2009a) uses $\int \mathcal{L}dt = 1.0$ fb^{-1} and results are reported for the $W \to e\nu$ decay mode only. Candidate events are selected by requiring a single high-p_T isolated charged lepton and large $\not\!\!E_T$. Table II shows the kinematic selection requirements, event yields, and background fraction for the W event selections.

TABLE II. The integrated luminosity, kinematic selection, event yield, and backgrounds for the CDF and D0 W boson mass analyses. The background is given as a percentage of the total yield.

	CDF		D0
	$W \to e\nu$	$W \to \mu\nu$	$W \to e\nu$
$\int \mathcal{L}dt$	0.2 fb^{-1}	0.2 fb^{-1}	1.0 fb^{-1}
E_T^ℓ, cal	>30 GeV	...	>25 GeV
p_T^ℓ, trk	>18 GeV/c	>30 GeV/c	>10 GeV/c
$\lvert\eta_\ell\rvert$			<1.05
$\not\!\!E_T$	>30 GeV/c	>30 GeV/c	>25 GeV/c
u_T	<15 GeV/c	<15 GeV/c	<15 GeV/c
Yield	63 964	51 128	499 830
Background	7.5%	1.1%	4.0%

The backgrounds include $Z \to \ell\ell$ events in which one lepton escapes identification, WW diboson events, and misidentification backgrounds in which the lepton is either a jet misidentified as an electron or a muon from semileptonic decay of hadrons in which the rest of the associated hadronic jet is not reconstructed. An additional source of events are the sequential decays $W \to \tau\nu \to e\nu\nu\nu$ and $W \to \tau\nu \to \mu\nu\nu\nu$. The CDF analysis treats these as signal while the D0 analysis incorporates these into the background template distributions.

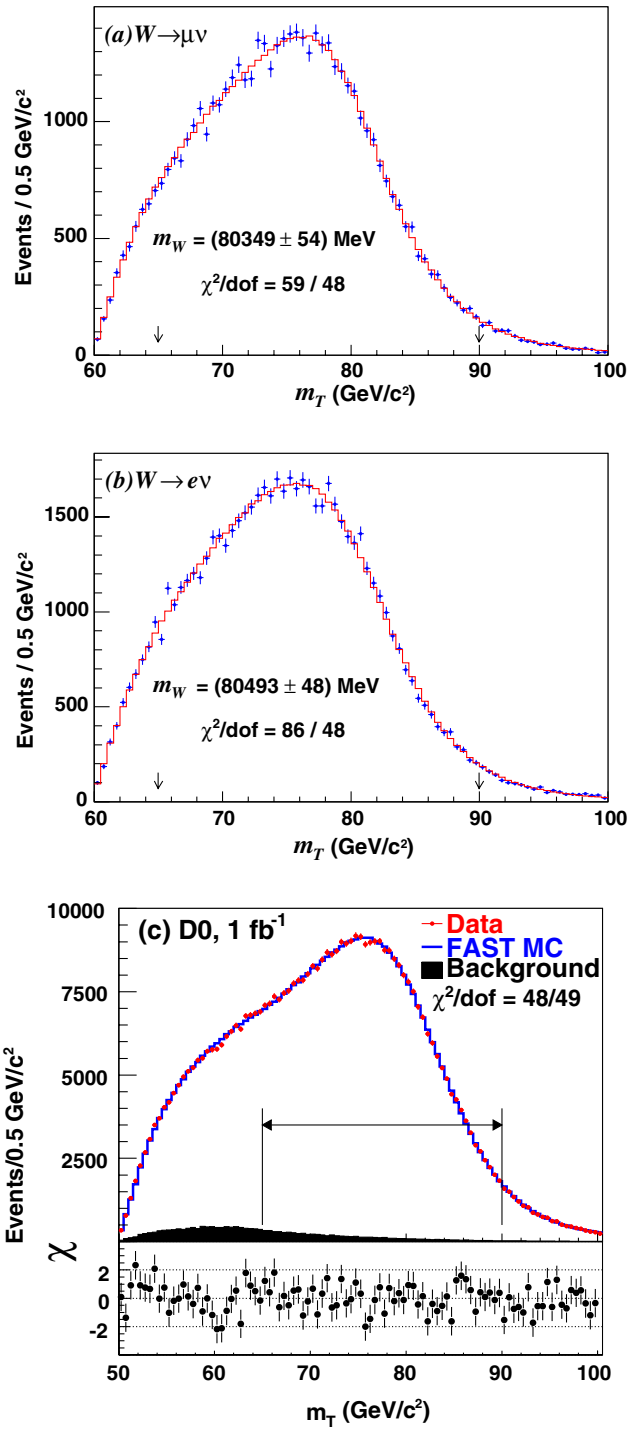

FIG. 4 (color online). The m_T distributions for (a) the CDF $W \to \mu\nu$ channel, (b) the CDF $W \to e\nu$ channel, and (c) the D0 $W \to e\nu$ channel.

The *in situ* calibration of charged particle momenta (CDF) and calorimetric measurement of electron energy (CDF, D0) is of crucial importance to this result. The CDF analysis uses a calibration of the tracker momentum scale (p) determined from dimuon and dielectron decays of J/ψ, Υ, and Z particles. This calibration is then transferred to the calorimeter energy measurement (E) using the E/p ratio. A final improvement is made for the $W \to e\nu$ mode by incorporating an additional calorimeter calibration based on $Z \to ee$ decays. The D0 analysis uses calorimeter energy measurements, and the calibration is based on the mass reconstructed in $Z \to ee$ events and a detailed simulation of the calorimeter response. For both experiments, this calibration is the dominant source of systematic uncertainty. Other sources of systematic uncertainty arise from trigger efficiency, lepton identification efficiency, correlation (in)efficiency such as occurs when the hadronic recoil is near the charged lepton, backgrounds, electroweak, and strong contributions to the production and decay model and the parton distribution functions.

The m_T distributions for each channel are shown in Fig. 4, and the results from each channel and the combinations of the channels for each experiment are shown in Table III. The systematic uncertainties are dominated by the lepton energy calibration. This contributes 17 MeV uncertainty to the CDF p_T^ℓ and p_T^ν channels, 30 MeV to the CDF m_T channel, and 34 MeV to each D0 channel. These results are shown along with previous measurements in Fig. 5. The world average combination (Alcaraz *et al.*, 2009; Tevatron Electroweak Working Group, 2009b) has been updated with these measurements using the BLUE (Lyons, Gibaut, and Clifford, 1988; Valassi, 2003) algorithm including correlations. The result is

$$M_W = 80.420 \pm 0.031 \text{ GeV}/c^2.$$

Because the systematic uncertainties are dominated by the statistical precision of the calibrations determined from control data samples, the systematic uncertainty in future measurements is expected to improve as the integrated luminosity increases. The ultimate limiting systematic is expected to be that introduced by the parton distribution functions. In the current results, this contributes an uncertainty of 11 MeV to all channels with a 100% correlation among the channels.

TABLE III. The individual CDF and D0 W boson mass results and their combinations. When two uncertainties are given, the first is the statistical uncertainty and the second is the systematic uncertainty.

		M_W (MeV)	χ^2/dof
CDF $W \to e\nu$	m_T	80 493 ± 48 ± 39	86/48
	p_T^e	80 451 ± 58 ± 45	63/62
	$\not\!\!E_T$	80 473 ± 57 ± 54	63/62
Combined		80 477 ± 62	
CDF $W \to \mu\nu$	m_T	80 349 ± 54 ± 27	59/48
	p_T^μ	80 321 ± 66 ± 40	72/62
	$\not\!\!E_T$	80 396 ± 66 ± 46	44/63
Combined		80 352 ± 60	
CDF $W \to e\nu + \mu\nu$		80 413 ± 34 ± 34	
D0 $W \to e\nu$	m_T	80 401 ± 23 ± 37	48/49
	p_T^e	80 400 ± 27 ± 40	39/31
	$\not\!\!E_T$	80 402 ± 23 ± 43	32/31
D0 combined		80 401 ± 21 ± 38	

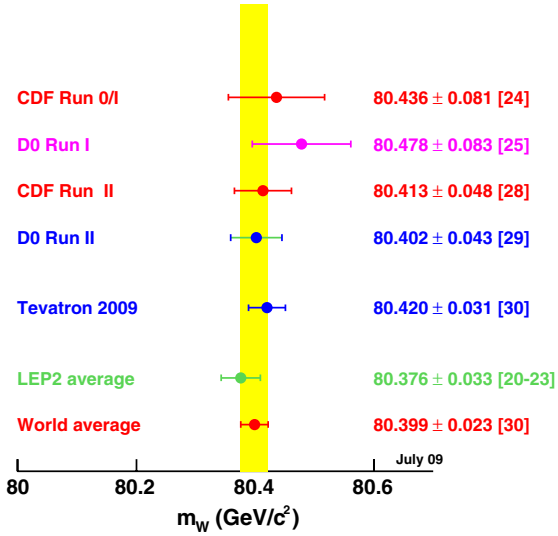

FIG. 5 (color online). Ideogram of previous measurements, the Run-II CDF and D0 measurements and the new world average. The reference is shown to the right of each measurement.

C. *W* Width

Like the W boson mass, the width Γ_W is also predicted by the SM. It is given by

$$\Gamma_W = \left[3 + 2N_C\left(1 + \frac{\alpha_S}{\pi}\right)\right]\frac{G_F M_W^3}{6\sqrt{2}\pi}(1 + \delta) \tag{4}$$

in which $N_C = 3$ is the number of colors, $1 + \alpha_S/\pi$ is the QCD correction factor to first order, and $\delta = 2.1\%$ (Rosner, Worah, and Takeuchi, 1994) is an EW correction factor. Direct measurements of Γ_W were made by CDF (Affolder *et al.*, 2000) and D0 (Abazov *et al.*, 2002b) using Tevatron Run I data and combined (Abazov *et al.*, 2002b). Measurements were also made by the experiments at LEP (Abbiendi *et al.*, 2006a; Achard *et al.*, 2006; Schael *et al.*, 2006; Abdallah *et al.*, 2008).

Because the W boson mass is distributed according to a Breit-Wigner formula, there is a tail at large mass values. The W boson width result is obtained using the m_T distribution in a region where the shape and event yield are dominated by events from the high mass region of the Breit-Wigner formula with limited impact from detector resolution effects. As for the W boson mass measurement, a binned likelihood comparison of the observed spectrum to templates generated for different W boson widths is used to extract the numerical value.

The W width was measured by the CDF (Aaltonen *et al.*, 2008a) and D0 (Abazov *et al.*, 2009b) using Run II data. The CDF result uses a data set of $\int \mathcal{L}dt = 0.35$ fb^{-1} and the electron and muon final states. The D0 result uses $\int \mathcal{L}dt = 1$ fb^{-1} and the electron final state. The D0 data set is the same one used for the W boson mass measurement. Similar dedicated simulations and processing were used for the W width measurement as were used for the W boson mass measurement. D0 used a different hadronic recoil procedure

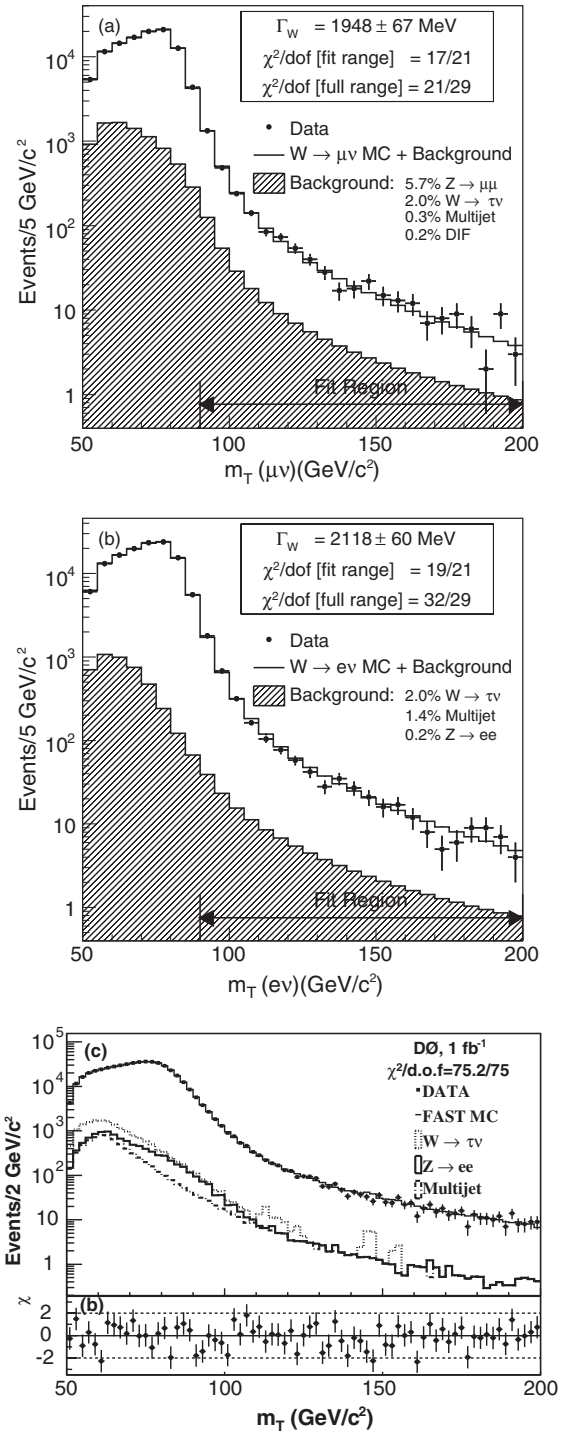

FIG. 6. The m_T distributions used for the Γ_W measurement. (a) The CDF $W \to \mu\nu$ channel. (b) The CDF $W \to e\nu$ channel. (c) The D0 $W \to e\nu$ channel.

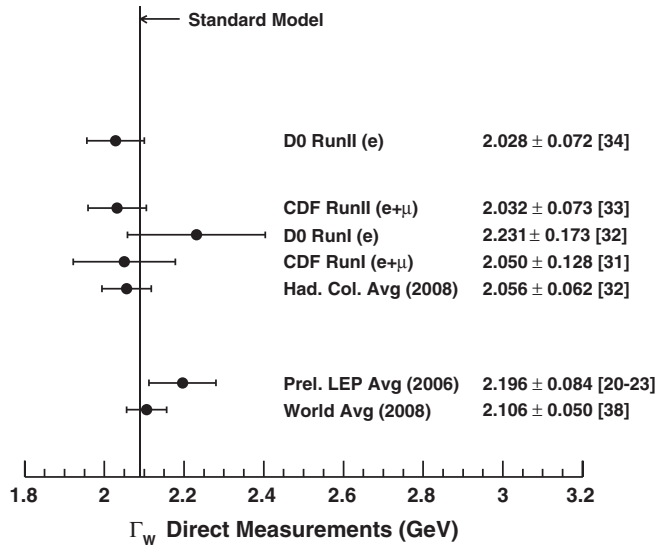

FIG. 7. Summary of the Γ_W measurements. The hadron collider average and world average results do not include the D0 result. From Abazov *et al.*, 2009b.

(Aaltonen *et al.*, 2009c). The new procedure gives a W boson mass result consistent with the standard method. Figure 6 shows the high mass region of the m_T distribution for the three channels analyzed: the CDF $W \to \mu\nu$ channel, the CDF $W \to e\nu$ channel, and the D0 $W \to e\nu$ channel. The Γ_W results are given in Table IV and shown in Fig. 7. The systematic uncertainties are dominated by a hadronic recoil scale and resolution uncertainties. These contribute 54 (49) MeV for the CDF $W \to e\nu$ ($W \to \mu\nu$) channel and 41 MeV to the D0 result. Other important sources include the lepton scale uncertainty and background uncertainty which are one half to two thirds the size of the hadronic recoil uncertainty.

D. Forward-backward asymmetry A_{FB}

Production of Z bosons at the Tevatron is dominated by the process $q\bar{q} \to Z/\gamma^*$ in which $q = u$, d are proton valence quarks. The SM couplings of the Z and γ to quarks depend on the quark charge Q, the isospin I_3, and the sine of the weak mixing angle $\sin^2\theta_W$. The differential cross section as a function of the direction of the fermion resulting from the Z/γ^* decay is given by

$$\frac{d\sigma}{d\cos\theta} = a(1 + \cos^2\theta) + b\cos\theta \tag{5}$$

in which θ is the angle of the fermion from the Z/γ^* decay measured relative to the incoming quark direction in the Z/γ^*

TABLE IV. The Γ_W measurements. For the result, the first uncertainty is the statistical uncertainty and the second is the systematic uncertainty.

Channel	Yield	Fit range (GeV/c^2)	Γ_W (MeV)	χ^2/dof
CDF $W \to \mu\nu$	2619	$90 < m_T < 200$	1948 ± 67 ± 71	17/21
CDF $W \to e\nu$	3436	$90 < m_T < 200$	2118 ± 60 ± 79	19/21
CDF combined			2032 ± 45 ± 57	
D0 $W \to e\nu$	5272	$100 < m_T < 200$	2028 ± 39 ± 61	75.2/75

rest frame. The relative Z and γ^* contributions to the cross section vary as a function of the Z/γ^* mass, and differences in the Z and γ couplings to quarks result in different angular distributions for the decay products for up-type ($I_3 = +1/2$) and down-type ($I_3 = -1/2$) quarks. Together, these two effects produce mass and flavor dependence in the coefficients a and b which can be calculated assuming the SM.

The forward-backward Z/γ^* production charge asymmetry is defined as

$$A \equiv \frac{\sigma_+ - \sigma_-}{\sigma_+ + \sigma_-}$$

in which σ_+ and σ_- are the integrated cross sections for the cases $\cos\theta > 0$ and $\cos\theta < 0$, respectively. The asymmetry extracted experimentally is given by

$$A_{FB} = \frac{N_+ - N_-}{N_+ + N_-} \tag{6}$$

in which N_+ and N_- are the acceptance, efficiency, and background corrected fermion yields in the forward ($\cos\theta > 0$) and backward ($\cos\theta < 0$) directions, respectively. Measuring the asymmetry rather than differential cross sections allows cancellation of many systematic uncertainties, particularly those affecting the overall normalization.

Measurements of the asymmetry as a function of dielectron mass have been made by both the CDF (Acosta *et al.*, 2005a) and D0 (Abazov *et al.*, 2008a) using the dielectron final state. The CDF result uses a sample with $\int \mathcal{L}dt = 72$ pb^{-1}, and the D0 measurement uses $\int \mathcal{L}dt = 1.1$ fb^{-1}. The selection criteria are similar to those for the Z cross section measurements although a larger dielectron mass range was selected for the asymmetry measurements. Two experimental issues of particular importance to these measurements are (1) controlling asymmetries in either detector acceptance or selection efficiency as a function of dielectron mass and (2) limiting the impact of electron charge misidentification.

In Table V, the dielectron mass range and the predicted and measured values of A_{FB} for each mass bin from the D0 measurements are shown, and Figs. 8 and 9 show the measured asymmetries and the SM predictions as a function of mass for the CDF and D0 results, respectively.

TABLE V. The expected and measured asymmetries as a function of dielectron mass (D0). For the measured values, the first uncertainty is statistical and the second is systematic.

Dielectron mass range [(GeV/c)^2]	A_{FB} PYTHIA	A_{FB} ZGRAD	A_{FB} Measured
50–60	−0.293	−0.307	−0.262 ± 0.066 ± 0.072
60–70	−0.426	−0.431	−0.434 ± 0.039 ± 0.040
70–75	−0.449	−0.452	−0.386 ± 0.032 ± 0.031
75–81	−0.354	−0.354	−0.342 ± 0.022 ± 0.022
81–86.5	−0.174	−0.166	−0.176 ± 0.012 ± 0.014
86.5–89.5	−0.033	−0.031	−0.034 ± 0.007 ± 0.008
89.5–92	0.051	0.052	0.048 ± 0.006 ± 0.005
92–97	0.127	0.129	0.122 ± 0.006 ± 0.007
97–105	0.289	0.296	0.301 ± 0.013 ± 0.015
105–115	0.427	0.429	0.416 ± 0.030 ± 0.022
115–130	0.526	0.530	0.543 ± 0.039 ± 0.028
130–180	0.593	0.603	0.617 ± 0.046 ± 0.013
180–250	0.613	0.600	0.594 ± 0.085 ± 0.016
250–500	0.616	0.615	0.320 ± 0.150 ± 0.018

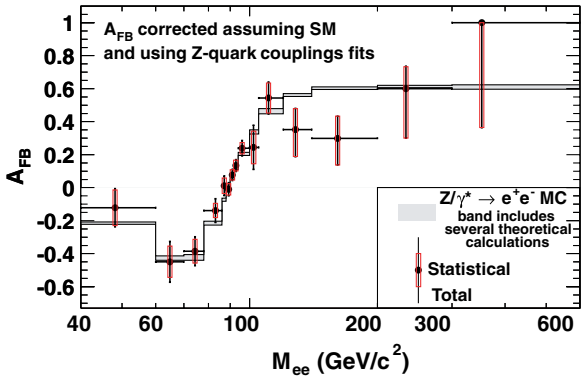

FIG. 8 (color online). Dielectron forward-backward asymmetry as a function of dielectron mass (CDF).

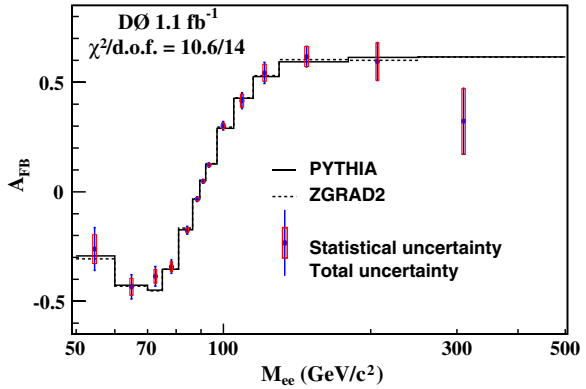

FIG. 9 (color online). Dielectron forward-backward asymmetry as a function of dielectron mass (D0).

Using these measurements and the SM prediction for the coefficients a and b, $\sin^2\theta_W^{\text{eff}}$ can be determined. Here θ_W^{eff} is the weak mixing angle including higher-order corrections. The current world average is

$$\sin^2\theta_W^{\text{eff}} = 0.231\,49 \pm 0.000\,13$$

using the modified minimal subtraction ($\overline{\text{MS}}$) scheme (Amsler *et al.*, 2008). Among the measurements used for the world average are two, the charge asymmetry for b-quark production (Abbiendi *et al.*, 2006b) from LEP and SLD and the measurement from NuTeV (Zeller *et al.*, 2002), which differ from the world average by more than 2 standard deviations.

The values for $\sin^2\theta_W^{\text{eff}}$ extracted using fits to the A_{FB} distributions are

$$\sin^2\theta_W^{\text{eff}} = 0.2238 \pm 0.0040(\text{stat}) \pm 0.0030(\text{syst})$$

for CDF and

$$\sin^2\theta_W^{\text{eff}} = 0.2327 \pm 0.0018(\text{stat}) \pm 0.0006(\text{syst})$$

for D0. Figure 10 shows these results compared to other measurements. The results from D0 are comparable in precision to other measurements for light quarks. The current Tevatron results are limited by sample statistics, but by the end of the Tevatron running, CDF and D0 are expected to

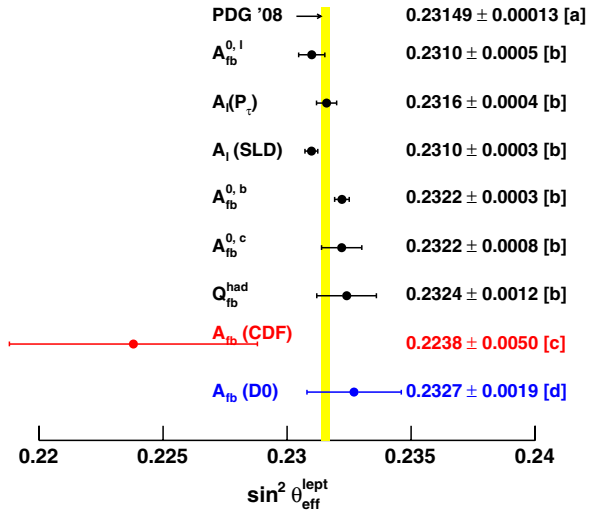

FIG. 10 (color online). Comparison of the Tevatron asymmetry results with those from other experiments. [a] Amsler *et al.* (2008); [b] Abbiendi *et al.* (2006a); [c] Acosta *et al.* (2005a); [d] Abazov *et al.* (2008a).

have the most precise measurements of $\sin^2\theta_W^{\text{eff}}$ for light quarks.

CDF also removed the assumption of SM quark couplings and determined values from a four parameter fit of A_{FB} measurements to the SM prediction as function of the vector and axial vector couplings for u and d quarks. The fit has a $\chi^2/\text{dof} = 10.4/11$, and the resulting coupling values are shown (with the SM values) in Fig. 11. No evidence of deviation from the SM is observed.

E. Dibosons

1. Trilinear gauge couplings

The non-Abelian nature of the gauge theory describing the electroweak interactions leads to a striking feature of the theory. In quantum electrodynamics, the photons carry no electric charge and thus lack photon-to-photon couplings and do not self-interact. In contrast, the weak vector bosons carry weak charge and do interact among themselves through trilinear and quartic gauge boson vertices. Figure 12 shows the tree-level diagram for diboson production involving trilinear gauge couplings.

The SM Lagrangian that describes the $WWV(V = Z, \gamma)$ interaction is given by

$$\mathcal{L}_{WWV}^{\text{SM}} = ig_{WWV}[(W_{\mu\nu}^{+}W^{-\mu} - W^{+\mu}W_{\mu\nu}^{-})V^{\nu} + W_{\mu}^{+}W_{\nu}^{-}V^{\mu\nu}],$$

where W^{μ} denotes the W field, $W_{\mu\nu} = \partial_\mu W_\nu - \partial_\nu W_\mu$, $V_{\mu\nu} = \partial_\mu V_\nu - \partial_\nu V_\mu$, the overall couplings are $g_{WW\gamma} = -e$ and $g_{WWZ} = -e\cot\theta_W$, and θ_W is the weak mixing angle (Hagiwara *et al.*, 1987). At tree level in the SM, the trilinear boson couplings involving only neutral gauge bosons (γ and Z) vanish because neither the photon nor the Z boson carry electric charge or weak hypercharge.

A common approach used to parametrize the low-energy effects from high-scale new physics is the effective

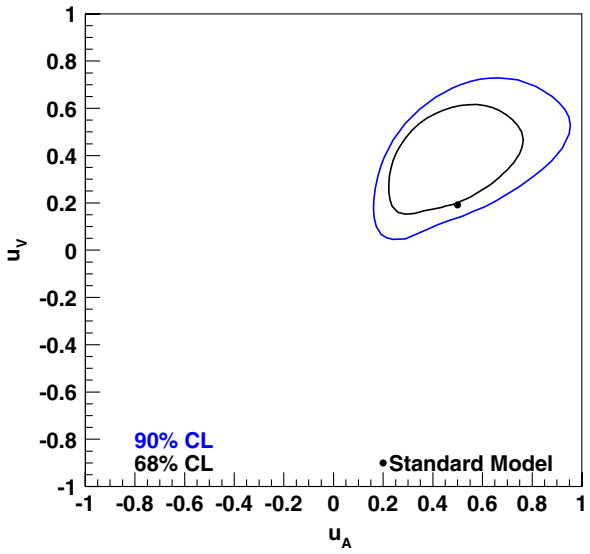

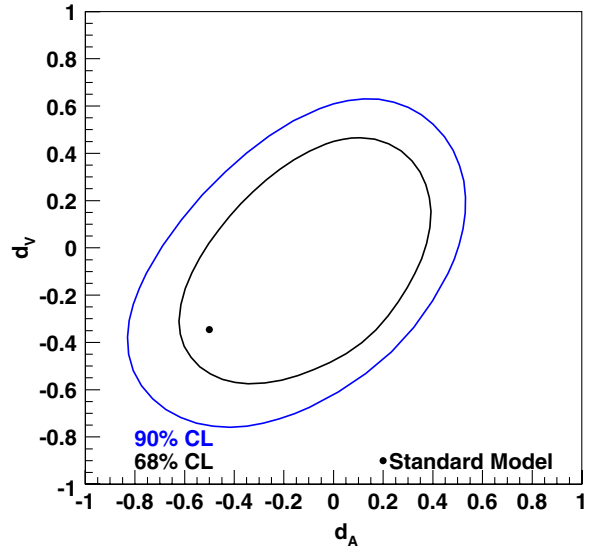

FIG. 11 (color online). The Zuu and Zdd coupling constants. From Acosta *et al.*, 2005a.

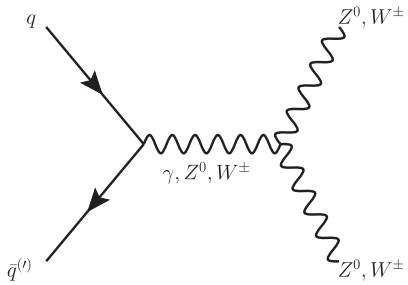

FIG. 12. Leading-order diagram for diboson production via quark-antiquark annihilation involving the trilinear gauge coupling.

Lagrangian approach that involves additional terms not present in the SM Lagrangian (Hagiwara *et al.*, 1987). This approach is convenient because it allows for diboson production properties measured in experiments to be interpreted as model-independent constraints on anomalous

coupling parameters which can be compared with the predictions of new physics models.

A general form for the WWV Lorentz-invariant interaction Lagrangian with anomalous coupling parameters g_1^V, κ_V, and λ_V is given by (Hagiwara *et al.*, 1987; Hagiwara, Woodside, and Zeppenfeld, 1990)

$$\mathcal{L}_{WWV}^{\text{eff}} = ig_{WWV}\Big[g_1^V(W_{\mu\nu}^+W^{-\mu} - W^{+\mu}W_{\mu\nu}^-)V^\nu + \kappa_V W_\mu^+ W_\nu^- V^{\mu\nu} + \frac{\lambda_V}{M_W^2} W_\mu^{+\nu} W_\nu^{-\rho} V_\rho^\mu\Big].$$

Note that $\mathcal{L}^{\text{eff}}$ reduces to $\mathcal{L}^{\text{SM}}$ for the values $\lambda_\gamma = \lambda_Z = 0$ and $g_1^\gamma = g_1^Z = \kappa_\gamma = \kappa_Z = 1$. Deviations from the SM values of the coupling parameters are denoted by Δg_1^V, $\Delta\kappa_V$, and $\Delta\lambda_V$. We have assumed that C and P are conserved in the interaction Lagrangian. There is no reason to believe that this assumption is valid unless the physics that leads to anomalous couplings respects these symmetries. It is straightforward to include additional terms that violate C and P, but we refrain from doing so in order to keep the discussion simple.

Electromagnetic gauge invariance requires $\Delta g_1^\gamma = 0$. The W boson magnetic moment μ_W and the electric quadrupole moment Q_W are related to the coupling parameters by

$$\mu_W = \frac{e}{2m_W}(1 + \kappa_\gamma + \lambda_\gamma)$$

and

$$Q_W = -\frac{e}{m_W^2}(\kappa_\gamma - \lambda_\gamma).$$

The anomalous couplings (aside from g_1^γ) are usually assumed to have some dependence on an energy scale (form factors) which suppresses them at large scales to avoid violation of tree-level unitarity in the diboson production amplitude (Baur and Zeppenfeld, 1988; Zeppenfeld and Willenbrock, 1988). The parametrization generally used for the energy dependence of a given coupling parameter α is

$$\alpha(\hat{s}) = \frac{\alpha_0}{(1 + \hat{s}/\Lambda^2)^2},$$

where $\sqrt{\hat{s}}$ is the partonic center-of-mass collision energy, α_0 is the value of the coupling parameter in the limit $\hat{s} \to 0$, and Λ is the cutoff scale.

The $\sqrt{\hat{s}}$ distribution used in the measurements described in this section is obtained through Monte Carlo simulation of the collision physics. With the substantially increased diboson statistics that will be available at the LHC, anomalous TGC searches can be reported as a function of $\sqrt{\hat{s}}$ in diboson decay channels resuting in fewer than two neutrinos, where the $\sqrt{\hat{s}}$ can be estimated on an event-by-event basis. This approach would lead to improved sensitivity and less dependence on *ad hoc* form factors as compared to the standard approach.

When reporting coupling limits from hadron collider data, the value of Λ is taken to be close to the hadron collision energy; even large variations (e.g., 50%) of Λ around this scale have minimal impact on the results. Physically, the scale Λ can be considered the scale at which the new physics responsible for the anomalous coupling is directly accessible (e.g., through pair production of new particles). This approach is different from the effective-field-theory approach discussed in Sec. II, where the coefficients of higher-dimension operators are constants. While in the same spirit as effective field theory, the effective Lagrangian approach to anomalous couplings is different in practice. In particular, the form factors invoked in the effective Lagrangian approach are unnecessary in an effective-field-theory approach.

In the presence of new physics, neutral TGCs (those involving only γ and Z bosons) can contribute to $Z\gamma$ and ZZ production. As described, neutral TGCs are anomalous by their very nature since these couplings are absent in the SM. For each of the diboson final states $Z\gamma$ and ZZ, one can follow an analogous procedure to the anomalous charged TGCs (those involving a W boson) by writing down the most general effective Lagrangian that respects Lorentz invariance and electromagnetic gauge invariance (Baur and Berger, 1993; Baur and Rainwater, 2000). Using prescriptions detailed by Baur and Berger (1993) and Baur and Rainwater (2000), the effective Lagrangians introduce anomalous coupling parameters $h_{i0}^V (V = \gamma, Z \text{ and } i = 3, 4)$ and $f_{j0}^V (V = \gamma, Z \text{ and } j = 4, 5)$, respectively, which can be constrained through an analysis of $Z\gamma$ and ZZ production in high-energy collider data. It is important to note that, under the assumption of on-shell Z bosons, the $Z\gamma Z$ couplings contributing to $Z\gamma$ production and $ZZ\gamma$ couplings contributing to ZZ production are completely independent (Baur and Rainwater, 2000).

In general, the effects on observables from turning on anomalous TGCs are correlated. When we refer to "1D limits," we refer to the limits derived on one parameter when the others are set to their SM values.

There are a few important differences regarding the study of diboson physics in particle collisions at LEP, Tevatron, and the LHC that are worth pointing out at this stage:

- At LEP, e^+e^- collisions occur at a well-defined energy that is set by the accelerator. Therefore, the center-of-mass energy is known with good precision and there are no form factors in anomalous coupling analyses.
- In e^+e^- collisions, the initial state has zero electric charge. Therefore, exclusive states with net charge, such as WZ and $W\gamma$, cannot be produced at LEP. The WW and ZZ states can and have been produced and studied at LEP. A measurement of the WW cross section over a scan in beam energy dramatically illustrates the existence of the WWZ coupling in electroweak theory (Quigg, 2009).
- At hadron colliders, $\sqrt{s}$ is fixed for long periods of time (defining different periods of the accelerator operation that change very infrequently), but $\sqrt{\hat{s}}$ varies collision by collision. Any anomalous couplings are likely to be $\sqrt{\hat{s}}$ dependent. The form factor ansatz used to cut off the anomalous coupling parameters at large $\sqrt{\hat{s}}$ to preserve S-matrix unitary of the amplitude reflects this dependence. For this reason, it is reasonable to expect that, once a sufficient amount of integrated luminosity has been acquired, the higher-energy reach afforded by high-energy hadron collisions will lead to better sensitivity to anomalous couplings as compared to the limits from LEP, despite larger backgrounds in a typical hadron collision event. In other words, hadron collisions at

the Tevatron and LHC sample events with a larger average $\sqrt{\hat{s}}$ as compared to LEP collision energies and it is exactly those high $\sqrt{\hat{s}}$ events that are most sensitive to effects of anomalous couplings from new physics at higher-energy scale.

- Because the Tevatron is a $p\bar{p}$ collider, the production cross sections for W^+Z and W^-Z are equal. The same is true for $W^+\gamma$ and $W^-\gamma$ production. When produced in a pp collider such as the LHC, positive and negative net charge diboson states have different production cross sections [e.g., $\sigma(pp \to W^+Z) > \sigma(pp \to W^-Z)$].

2. $W\gamma$

The $W\gamma$ final state observed at hadron colliders provides a direct test of the $WW\gamma$ TGC. Anomalous $WW\gamma$ couplings lead to an enhancement in the production cross section and an excess of large E_T photons. Both CDF and D0 published measurements of the $W\gamma$ cross section using leptonic decays of the W bosons and $\int \mathcal{L}dt = 0.2$ fb^{-1} (Abazov *et al.*, 2005a; Acosta *et al.*, 2005a). The signature of the $W\gamma$ signal is an isolated high E_T lepton, an isolated high E_T photon, and large $\not{E}_T$ due to the neutrino from the W decay. The dominant background is from W + jets where a jet mimics an isolated photon. A lepton-photon separation requirement in $\eta - \phi$ space of $\Delta R = \sqrt{(\Delta\eta)^2 + (\Delta\phi)^2} > 0.7$ is made by both CDF and D0 to suppress events with final-state radiation of the photon from the outgoing lepton and to avoid collinear singularities in theoretical calculations. A kinematic requirement on photon E_T of $E_T > 7$ (8) GeV is made by CDF (D0) in the analysis.

CDF measures

$$\sigma(p\bar{p} \to W\gamma + X) \times \mathrm{BR}(W \to l\nu) = 18.1 \pm 1.6(\mathrm{stat}) \pm 2.4(\mathrm{syst}) \pm 1.2(\mathrm{lum})\ \mathrm{pb}$$

(Acosta *et al.*, 2005b) in agreement with the next-to-leading-order (NLO) theoretical expectation ($E_T > 7$ GeV) (Baur and Berger, 1993) of 19.3 ± 1.4 pb. D0 measures

$$\sigma(p\bar{p} \to W\gamma + X) \times \mathrm{BR}(W \to l\nu) = 14.8 \pm 1.6(\mathrm{stat}) \pm 1.0(\mathrm{syst}) \pm 1.0(\mathrm{lum})\ \mathrm{pb}$$

(Abazov *et al.*, 2005a) also in agreement with the NLO expectation ($E_T > 8$ GeV) (Baur and Berger, 1993) of 16.0 ± 0.4 pb. Table VI summarizes the $W\gamma$ cross-section measurement results.

Both CDF and D0 $W\gamma$ cross-section measurement are consistent with the SM expectations at NLO. In a more recent analysis (Abazov *et al.*, 2008b), D0 uses 4 times more integrated luminosity as compared to Abazov *et al.* (2005a) and adds photons reconstructed in their end cap calorimeters ($1.5 < |\eta_{\mathrm{det}}| < 2.5$) to search for anomalous $WW\gamma$ couplings based on the observed photon E_T spectrum (Abazov *et al.*, 2008b) for photons with $E_T > 9$ GeV. Additionally, the three-body transverse mass of the photon, lepton, and $\not{E}_T$ must exceed 120 GeV/c (110 GeV/c) for the electron (muon) channel in order to suppress final-state radiation. The photon E_T spectrum and anomalous TGC limits are shown in Fig. 13. A LO simulation (Baur and Berger, 1990) of the $W\gamma$ signal is used with NLO corrections (Baur and Berger, 1993) applied to the photon E_T spectrum. The one-dimensional limits at 95% confidence level (C.L.) are $-0.51 < \Delta\kappa_\gamma < 0.51$ and $-0.12 < \lambda_\gamma < 0.13$ for $\Lambda = 2.0$ TeV.

The SM $W\gamma$ production involves interference between the amplitudes for a photon radiated off of an incoming quark (QED initial-state radiation) and the photon produced from the $WW\gamma$ vertex. This interference leads to a zero amplitude for the SM in the photon angular distribution (Brown, Sahdev, and Mikaelian, 1979; Mikaelian, Samuel, and Sahdev, 1979; Goebel, Halzen, and Leveille, 1981; Brodsky and Brown, 1982). In $W\gamma$ production, the radiation amplitude zero (RAZ) manifests itself as a dip at $\sim -1/3$ in the charged-signed rapidity difference $Q_\ell \times \Delta y$ between the observed photon and the charged lepton from decay of the W boson (Baur, Errede, and Landsberg, 1994). Experimentally, the pseudorapidity difference $\Delta\eta$ is used in place of the rapidity difference Δy, since it involves only the production angle θ with respect to the beam line [$\eta = -\ln(\tan(\theta/2))$] and is a very good approximation to Δy in the limit of massless particles. Using the same data they used to limits on $WW\gamma$ anomalous TGCs, D0 made the first detailed study of the $Q_\ell \times \Delta y$ to search for the RAZ effect (Abazov *et al.*, 2008b).

Figure 14(a) shows the $Q_\ell \times \Delta y$ distribution of data compared with the SM expectation, which has a 15% χ^2

TABLE VI. Summary of the $W\gamma \to \ell\nu\gamma$ CDF (Acosta *et al.*, 2005b) and D0 (Abazov *et al.*, 2005a) cross-section analyses compared with the theory (Baur and Berger, 1993). For the CDF analysis, the luminosities with and without parentheses correspond to central and forward leptons, respectively. The theory cross section is the NLO calculation (in pb) from Baur and Berger, 1993.

	D0 analysis		CDF analysis	
	$e\nu\gamma$	$\mu\nu\gamma$	$e\nu\gamma$	$\mu\nu\gamma$
$\int \mathcal{L}dt$ (fb^{-1})	0.16	0.13	0.20 (0.17)	0.19 (0.18)
W + jet(s)	59 ± 5	62 ± 5	60 ± 18	28 ± 8
ℓeX	1.7 ± 0.5	0.7 ± 0.2	...	...
$W\gamma \to \tau\nu\gamma$	0.42 ± 0.02	1.9 ± 0.2	1.5 ± 0.2	2.3 ± 0.2
$Z\gamma \to \ell\ell\gamma$	...	6.9 ± 0.7	6.3 ± 0.3	17.4 ± 1.0
Total background	61 ± 5	71 ± 5	67 ± 18	47 ± 8
N_{observed}	112	161	195	128
$\sigma \times$ BR (pb)	13.9 ± 3.4	15.2 ± 2.5	19.4 ± 3.6	16.3 ± 2.9
Theory $\sigma \times$ BR	16.0 ± 0.4		19.3 ± 1.4	

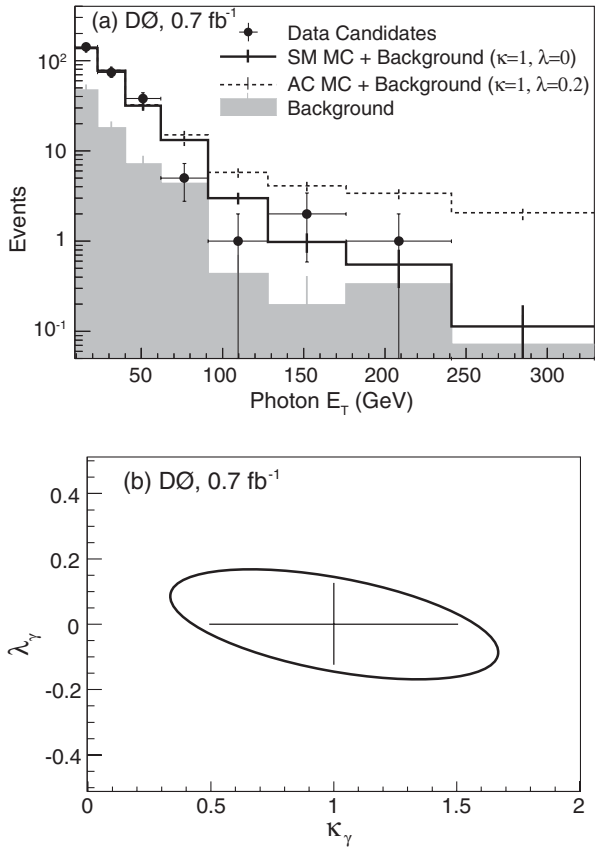

FIG. 13. The (a) photon E_T distribution for the D0 $W\gamma$ analysis. From Abazov *et al.*, 2008b. The photon E_T distribution of events is used to constrain anomalous coupling parameters shown in (b).

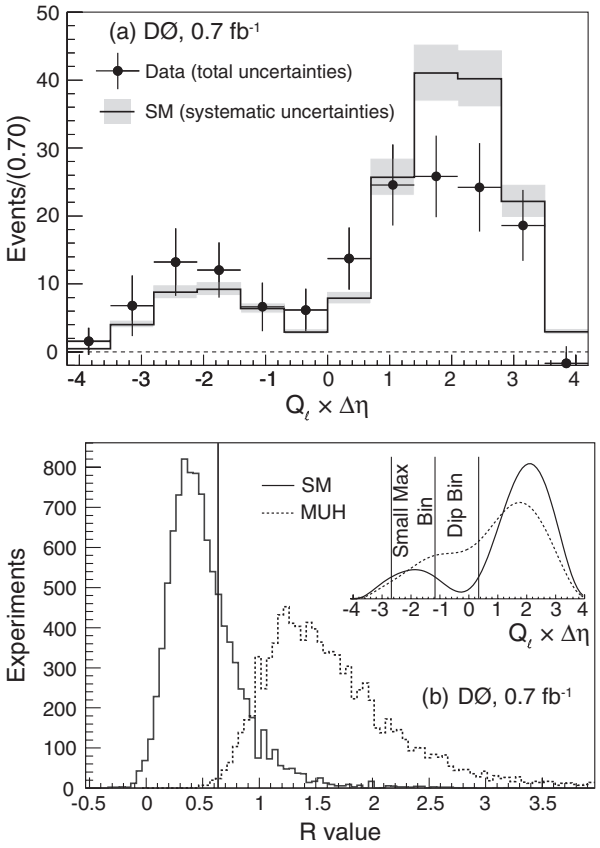

FIG. 14. (a) The background-subtracted charge-signed rapidity difference of events is shown along with the SM expectation from Abazov *et al.* (2008b). Consideration of the full covariance matrix gives a 15% χ^2 probability for compatibility between the data and the SM expectation. (b) Distributions of the R-test statistic for the SM (solid line) and "no-dip" (dashed line) hypothesis pseudoexperiments from Abazov *et al.* (2008b). The data result is 0.64 shown by the vertical line where only 45 out of 10^4 no-dip pseudoexperiments had a value smaller as small or smaller than 0.64. The R-test statistic is defined as the ratio of events in the "Dip Bin" to the "Small Max Bin," as shown in the inset where the solid line is the SM expectation and the dashed line is for the no-dip hypothesis.

probability for compatibility between the data and the SM expectation, demonstrating a reasonable level of agreement. To specifically investigate the dip region around $Q_\ell \times \Delta y = -1/3$ indicative of the RAZ effect, a simple test statistic R is constructed which is the ratio of the number events observed in a bin including the dip region to the number of events observed in a bin with more negative $Q_\ell \times \Delta y$ where a maximum is expected, based on Monte Carlo simulation, from the SM including the total D0 acceptance in this analysis. A value of $R = 0.64$ is observed in the data and it is determined that 28% of SM pseudoexperiments give a value as large or larger than 0.64.

A particular anomalous coupling hypothesis corresponding to $\kappa_\gamma = 0$, $\lambda_\gamma = -1$ is chosen to test against as a null hypothesis since it is a specific model which leads to a $Q_\ell \times \Delta y$ distribution without a dip as shown in the inset of Fig. 14(b). Only the shape is tested such that the null "no-dip" distribution is normalized to the yield expected from the SM. The R distribution for the SM and no-dip hypotheses are shown in Fig. 14(b) along with the value (0.64) observed in the data. From this analysis, the no-dip hypothesis is excluded at 2.6σ Gaussian significance.

3. $Z\gamma$

As mentioned in Sec. III.E.1, photons do not directly couple to Z bosons at tree level in the SM. Therefore, observation of such a coupling constitutes evidence for new phenomena. The $Z\gamma$ final state at hadron colliders involves a combination of $ZZ\gamma$ and $Z\gamma\gamma$ couplings. Both CDF and D0 made measurements of the $Z\gamma$ cross section in leptonic decay channels of the Z boson. The signature of the $Z\gamma$ signal is two isolated high E_T charged leptons having the same flavor and opposite charge with invariant mass consistent with decay of a Z boson, and an isolated high E_T photon. The dominant background is from Z + jets, where a jet mimics an isolated photon. As in the $W\gamma$ analyses described in Sec. III.E.2, a lepton-photon separation requirement is imposed. A requirement of $\Delta R > 0.7$ is made by both CDF and D0. Kinematic requirements on the photon E_T of $E_T > 7(8)$ GeV/c^2 and the dilepton invariant mass of $M_{\ell\ell} > 40(30)$ GeV/c^2 are made by CDF (D0) in the analysis.

Using $\int \mathcal{L}dt = 0.2$ fb^{-1}, CDF measures

$$\sigma(p\bar{p} \to Z\gamma + X) \times \mathrm{BR}(Z \to ll) = 4.6 \pm 0.5(\mathrm{stat}) \pm 0.2(\mathrm{syst}) \pm 0.3(\mathrm{lum})\ \mathrm{pb}$$

(Acosta *et al.*, 2005b) in agreement with the NLO theoretical expectation using Baur and Berger (1993) of 4.5 ± 0.3 pb

TABLE VII. Summary of the $Z\gamma \to \ell\ell\gamma$ CDF (Acosta *et al.*, 2005b) and D0 (Abazov *et al.*, 2007a) cross-section analyses compared with the theory (Baur, Han, and Ohnemus, 1998). For the CDF analysis, the luminosities with and without parentheses correspond to central and forward leptons, respectively. The theory cross section is the NLO calculation (in pb) from Baur, Han, and Ohnemus, 1998.

	D0 analysis		CDF analysis	
	$ee\gamma$	$\mu\mu\gamma$	$ee\gamma$	$\mu\mu\gamma$
$\int \mathcal{L}dt$ (fb^{-1})	1.1	1.0	0.20 (0.17)	0.19 (0.18)
Z + jets background	55 ± 8	61 ± 9	2.8 ± 0.9	2.1 ± 0.6
N_{observed}	453	515	36	35
$\sigma \times$ BR (pb)	5.0 ± 0.4		4.8 ± 0.9	4.4 ± 0.8
Theory $\sigma \times$ BR	4.7 ± 0.2		4.5 ± 0.3	

using the CDF acceptance. Using $\int \mathcal{L}dt = 1.1$ fb^{-1}, D0 measures

$$\sigma(p\bar{p} \to Z\gamma + X) \times \text{BR}(Z \to ll) = 5.0 \pm 0.3(\text{stat} + \text{syst}) \pm 0.3(\text{lum})\ \text{pb}$$

(Abazov *et al.*, 2007a) also in agreement with the NLO expectation using the generator described by Baur, Han, and Ohnemus (1998) of 4.7 ± 0.2 pb and the D0 acceptance. Table VII summarizes the $Z\gamma$ cross-section measurement results. Figure 15 shows the three-body mass $M_{\ell\ell\gamma}$ versus the dilepton mass $M_{\ell\ell}$ for $Z\gamma$ candidate events in the D0 analysis (Abazov *et al.*, 2007a).

Using $\int \mathcal{L}dt = 3.6$ fb^{-1}, the D0 Collaboration observed (5.1σ) the $Z\gamma \to \nu\nu\gamma$ process for the first time at a hadron collider (Abazov *et al.*, 2009d) and used these events to search for $Z\gamma\gamma$ and $ZZ\gamma$ couplings that are absent at tree level in the SM. The experimental signature for $Z\gamma \to \nu\nu\gamma$ is a high-energy photon and large $\not{E}_T$. In the analysis, events are required to have a single photon candidate with $E_T > 90$ GeV and $\not{E}_T > 70$ GeV$/c$. The primary backgrounds are from $W \to e\nu$ and events unrelated to the collision in which muons from beam halo or cosmic rays produce energetic photons

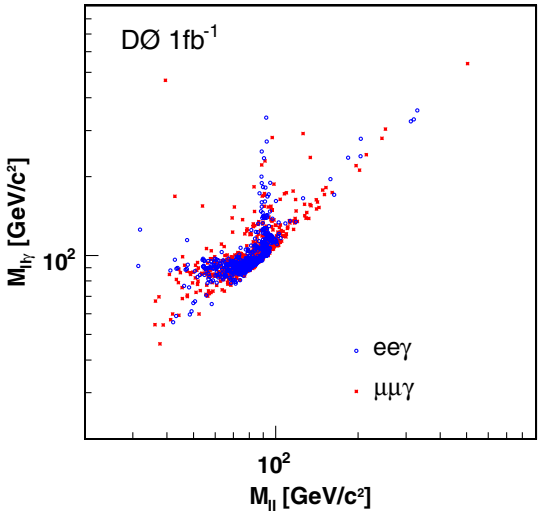

FIG. 15 (color online). The three-body mass $M_{\ell\ell\gamma}$ vs the dilepton mass $M_{\ell\ell}$ for $Z\gamma$ candidate events in the D0 analysis. From Abazov *et al.*, 2007a.

TABLE VIII. Summary of background estimates, and the number of observed and SM predicted events for the D0 analysis of the $Z\gamma \to \nu\nu\gamma$ channel (Abazov *et al.*, 2009d).

	No. of events
$W \to e\nu$	$9.67 \pm 0.30(\text{stat}) \pm 0.48(\text{syst})$
Noncollision	$5.33 \pm 0.39(\text{stat}) \pm 1.91(\text{syst})$
W/Z + jet	$1.37 \pm 0.26(\text{stat}) \pm 0.91(\text{syst})$
$W\gamma$	$0.90 \pm 0.07(\text{stat}) \pm 0.12(\text{syst})$
Total background	$17.3 \pm 0.6(\text{stat}) \pm 2.3(\text{syst})$
$N^{\text{SM}}_{\nu\bar{\nu}\gamma}$	33.7 ± 3.4
N_{obs}	51

through bremsstrahlung. The $W \to e\nu$ is suppressed by removing events with high-p_T tracks and the noncollision events are removed using available z_0 production information from the EM calorimeter and preshower detectors. A summary of the background estimates and observed events is shown in Table VIII. The measured cross section is

$$\sigma(p\bar{p} \to Z\gamma + X) \times \text{BR}(Z \to \nu\nu) = 32 \pm 9(\text{stat} + \text{syst}) \pm 2(\text{lum})\ \text{fb}$$

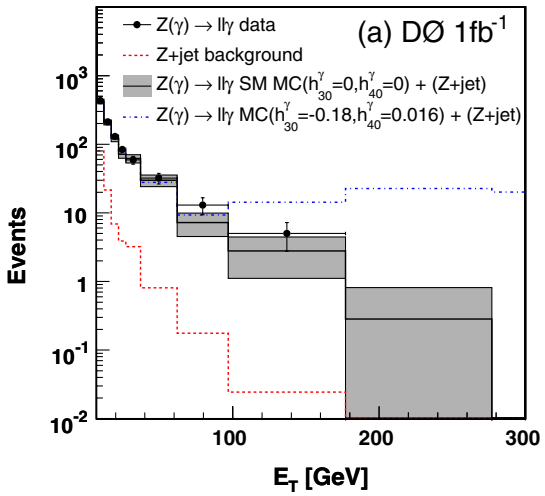

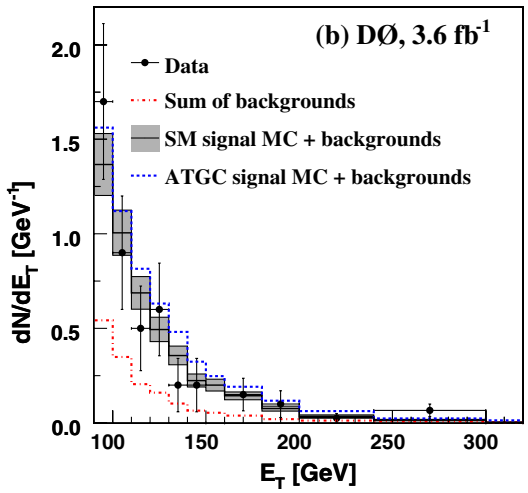

FIG. 16 (color online). The observed photon E_T spectrum along with the SM expectation and possible anomalous TGC scenarios for (a) $Z\gamma \to \ell\ell\gamma$ (Abazov *et al.*, 2007a) and (b) $Z\gamma \to \nu\nu\gamma$ (Abazov *et al.*, 2009d) channels.

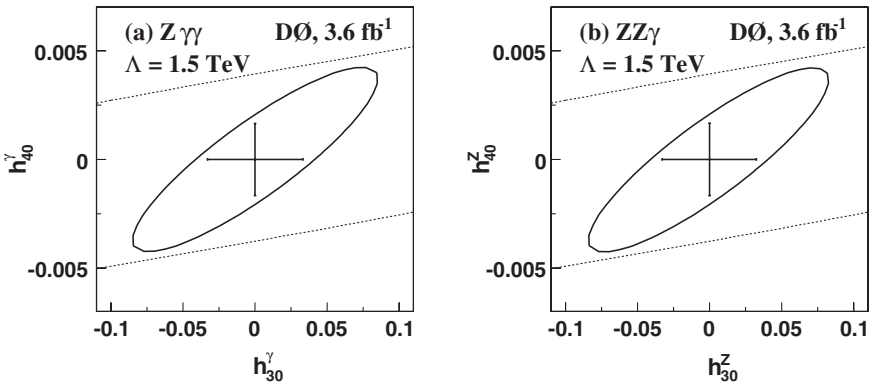

FIG. 17. Two-dimensional bounds (ellipses) at 95% C.L. on *CP*-conserving (a) $Z\gamma\gamma$ and (b) $ZZ\gamma$ couplings. The crosses represent the one-dimensional bounds at the 95% C.L. setting all other couplings to zero. The dashed lines indicate the unitarity limits for $\Lambda = 1.5$ TeV. From Abazov *et al.*, 2009d.

for the photon $E_T > 90$ GeV, consistent with the NLO cross section of 39 ± 4 fb (Baur, Han, and Ohnemus, 1998).

Both of the CDF and D0 $Z\gamma$ cross-section measurements are consistent with the SM expectations at NLO. D0 searches for anomalous $Z\gamma\gamma$ and $ZZ\gamma$ couplings using the observed photon E_T spectrum in the $Z\gamma \to \ell\ell\gamma$ (Abazov *et al.*, 2007a) and $Z\gamma \to \nu\nu\gamma$ (Abazov *et al.*, 2009d). A LO simulation (Baur and Berger, 1993; Baur, Han, and Ohnemus, 1998) of the $Z\gamma$ signal is used with NLO corrections (Baur, Han, and Ohnemus, 1998) applied to the photon E_T spectrum. The observed photon E_T spectrum along with the SM expectation and possible anomalous TGC scenarios for two channels is shown in Fig. 16. The $Z\gamma \to \ell\ell\gamma$ and $Z\gamma \to \nu\nu\gamma$ combined limits on the *CP*-conserving $Z\gamma\gamma$ and $ZZ\gamma$ couplings are shown in Fig. 17. The 1D combined limits at 95% C.L. are $|h_{30}^{\gamma}| < 0.033$, $|h_{40}^{\gamma}| < 0.0017$, $|h_{30}^{Z}| < 0.033$, and $|h_{40}^{Z}| < 0.0017$ for $\Lambda = 1.5$ TeV.

4. *WW*

Production of W boson pairs in hadron (and lepton) collisions involves both the $WW\gamma$ and WWZ couplings. First evidence for W boson pair production was reported by CDF using Tevatron Run-I data (Abe *et al.*, 1997). This process was later measured with greater significance by D0 and CDF using $\int \mathcal{L}dt = 224$–252 and $\int \mathcal{L}dt = 184$ pb^{-1}, respectively, from Run-II of the Tevatron (Abazov *et al.*, 2005b; Acosta *et al.*, 2005c). At LEP, WW production has been extensively studied and stringent limits on anomalous TGC were determined. At the Tevatron, much higher WW invariant masses are probed compared to LEP because of the higher accessible energies. Also, the WW final state is a promising discovery channel for the Higgs boson at both the Tevatron and the LHC. In hadron collisions, the production of W boson pairs is most easily observed in the fully leptonic decay mode $WW \to \ell\nu\ell\nu$. The experimental signature of the WW signal in leptonic decay is two isolated high E_T charged leptons with opposite charge and large $\not{E}_T$ from the neutrinos.

Both CDF and D0 measured the WW production cross section in fully leptonic decay and used their data to search for anomalous $WW\gamma$ and WWZ couplings. In both analyses, the dominant backgrounds are from $t\bar{t}$, Drell-Yan processes (DY), other diboson decays, and W + jets where the jet fakes an isolated lepton. In the CDF analysis (Aaltonen *et al.*, 2010a), $t\bar{t}$ is suppressed by requiring no reconstructed jets with $E_T > 15$ GeV and $|\eta| < 2.5$. In the D0 analysis (Abazov *et al.*, 2009e), the p_T of the WW system, estimated from the observed charged-lepton momenta and the $\not{E}_T$, is required to be small [< 20 GeV/c (ee), 25 GeV/c ($e\mu$), or 16 GeV/c ($\mu\mu$)] in order to suppress $t\bar{t}$ decays.

The strategy for measuring the cross section for $p\bar{p} \to WW + X$ differs between the CDF and D0 analyses. In the D0 analysis, the WW signal yield is determined from counting the number of events in excess of the expected SM backgrounds using $\int \mathcal{L}dt = 1.1$ fb^{-1}, as shown in Table IX. D0 measures

$$\sigma(p\bar{p} \to WW + X) = 11.5 \pm 2.1(\text{stat} + \text{syst}) \pm 0.7(\text{lum})\ \text{pb}$$

(Abazov *et al.*, 2009e), in agreement with the NLO expectation of 12.0 ± 0.7 pb (Campbell and Ellis, 1999).

In the CDF analysis, the WW signal yield is extracted from a fit to the distribution of a matrix element likelihood ratio (LR_{WW}) discriminant for events using $\int \mathcal{L}dt = 3.6$ fb^{-1}. The events which are fit are required to pass relatively loose selection criteria as compared to the selection CDF would use for a cross-section measurement based on the event yield

TABLE IX. Numbers of signal and background events expected and number of events observed after the final event selection in each channel for the D0 WW cross-section measurement (Abazov *et al.*, 2009e).

Process	ee	$e\mu$	$\mu\mu$
$Z/\gamma^* \to ee/\mu\mu$	0.27 ± 0.20	2.52 ± 0.56	0.76 ± 0.36
$Z/\gamma^* \to \tau\tau$	0.26 ± 0.05	3.67 ± 0.46	⋯
$t\bar{t}$	1.10 ± 0.10	3.79 ± 0.17	0.22 ± 0.04
WZ	1.42 ± 0.14	1.29 ± 0.14	0.97 ± 0.11
ZZ	1.70 ± 0.04	0.09 ± 0.01	0.84 ± 0.03
$W\gamma$	0.23 ± 0.16	5.21 ± 2.97	⋯
W + jet	6.09 ± 1.72	7.50 ± 1.83	0.12 ± 0.24
Multijet	0.01 ± 0.01	0.14 ± 0.13	⋯
$WW \to \ell\ell'$	10.98 ± 0.59	39.25 ± 0.81	7.18 ± 0.34
$WW \to \ell\tau/\tau\tau \to \ell\ell'$	1.40 ± 0.20	5.18 ± 0.29	0.71 ± 0.10
Total expected	23.46 ± 1.90	68.64 ± 3.88	10.79 ± 0.58
Data	22	64	14

TABLE X. Expected number of signal (WW) and background events along with the total number of expected and observed events in the data for the CDF WW cross-section measurement (Aaltonen *et al.*, 2010a).

Process	Events
Z/γ^* (Drell-Yan)	79.8 ± 18.4
WZ	13.8 ± 1.9
$W\gamma$	91.7 ± 24.8
$W + 1 -$ jet	112.7 ± 31.2
ZZ	20.7 ± 2.8
$t\bar{t}$	1.3 ± 0.2
Total background	320.0 ± 46.8
W^+W^-	317.6 ± 43.8
Total expected	637.6 ± 73.0
Data	654

alone. Table X shows the expected number of signal and background events along with the observed events in the data used to fit for the signal. For each event passing the signal selection criteria, four matrix-element-based (ME) event probabilities are calculated corresponding to the production and decay processes $WW \to \ell\nu\ell\nu$, $ZZ \to \ell\ell\nu\nu$, $W + 1 -$ jet $\to \ell\nu + 1 -$ jet, and $W\gamma \to \ell\nu + \gamma$. In the latter two processes, the jet or γ is assumed to have been reconstructed as a charged-lepton candidate. The event probability for a process X is given by

$$P_X(\vec{x}) = \frac{1}{\langle\sigma\rangle}\int \frac{d\sigma(\vec{y})}{d\vec{y}}\epsilon(\vec{y})G(\vec{x},\vec{y})d\vec{y}, \tag{7}$$

where $\vec{x}$ represents the observed lepton momenta and $\not{E}_T$ vectors, $G(\vec{x},\vec{y})$ is a transfer function representing the detector resolution, and $\epsilon(\vec{y})$ is an efficiency function parametrized by η which quantifies the probability for a particle to be reconstructed as a lepton. The differential cross section $d\sigma(\vec{y})/d\vec{y}$ is calculated using leading-order matrix elements from the MCFM program (Campbell and Ellis, 1999) and integrated over all possible true values of the final-state particle four-vectors $\vec{y}$. The normalization factor $\langle\sigma\rangle$ is determined from the leading-order cross section and detector acceptance for each process. These event probabilities are combined into a likelihood ratio

$$LR_{WW} = \frac{P_{WW}}{P_{WW} + \sum_j k_j P_j}, \tag{8}$$

where $j = \{ZZ, W + 1 -$ jet, $W\gamma\}$ and k_j is the relative fraction of the expected number of events for the jth process such that $\sum_j k_j = 1$. The templates of the LR_{WW} distribution are created for signal and each background process given in Table X.

A binned maximum likelihood is used to extract the WW production cross section from the shape and normalization of the LR_{WW} templates. The likelihood is formed from the Poisson probabilities of observing n_i events in the ith bin when μ_i are expected. Variations corresponding to the systematic uncertainties described previously are included as normalization parameters for signal and background, constrained by Gaussian terms. The likelihood is given by

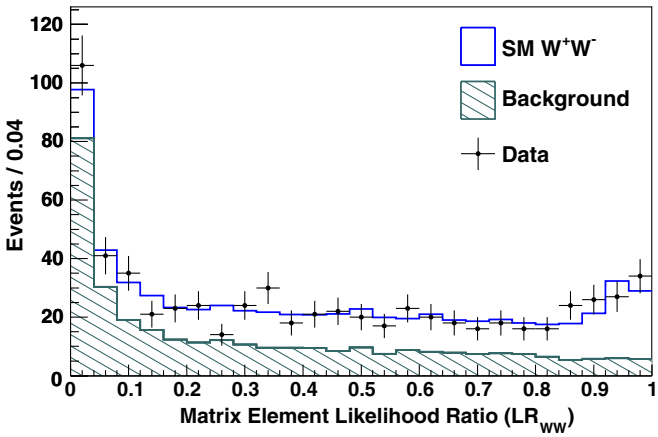

FIG. 18 (color online). The LR_{WW} distributions for the signal (W^+W^-) and background processes after a maximum likelihood fit to the data for the CDF WW cross-section measurement. From Aaltonen *et al.*, 2010a.

$$\mathcal{L} = \left(\prod_i \frac{\mu_i^{n_i} e^{-\mu_i}}{n_i!}\right)\cdot\prod_c e^{-S_c^2/2}, \tag{9}$$

where

$$\mu_i = \sum_k \alpha_k\left[\prod_c (1 + f_k^c S_c)\right](N_k^{\mathrm{Exp}})_i, \tag{10}$$

f_k^c is the fractional uncertainty for the process k due to the systematic c, and S_c is a floating parameter associated with the systematic uncertainty c. The correlations of systematic uncertainties between processes are accounted for in the definition of μ_i. The expected number of events from process k in the ith bin is given by $(N_k^{\mathrm{Exp}})_i$. The parameter α_k is an overall normalization parameter for process k and is fixed to unity for all processes other than WW, for which it is freely floating. The likelihood is maximized with respect to the systematic parameters S_c and α_{WW}. The WW cross section is then given by the fitted value of α_{WW} multiplied by $\sigma^{\mathrm{NLO}}(p\bar{p} \to WW)$.

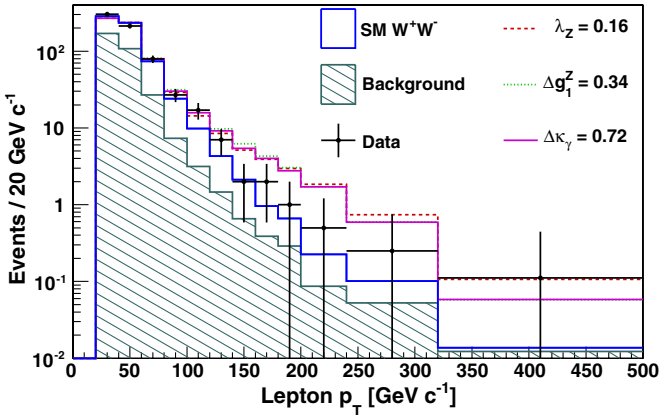

FIG. 19 (color online). Leading-lepton p_T distribution for data compared to the SM expectation for the CDF $WW \to \ell\nu\ell\nu$ analysis (Aaltonen *et al.*, 2010a). Also shown is how the expectation would be modified by anomalous couplings near the observed limits.

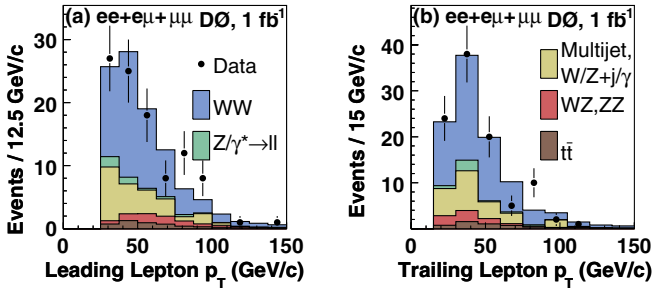

FIG. 20 (color online). Distributions of the (a) leading and (b) trailing lepton p_T for the D0 $WW \to \ell\nu\ell\nu$ analysis (Abazov *et al.*, 2009e). Data are compared to the estimated signal $\sigma(WW) = 12$ pb and the background sum.

The fit to the data of the signal and sum of the individually fitted background templates is shown in Fig. 18. The measured WW production cross section is

$$\sigma(p\bar{p} \to WW + X) = 12.1 \pm 0.9(\text{stat})^{1.6}_{-1.4}(\text{syst})\ \text{pb}$$

(Aaltonen *et al.*, 2010a) in agreement with the NLO theoretical expectation of 11.7 ± 0.7 pb (Campbell and Ellis, 1999).

Both of the CDF and D0 WW cross-section measurements are consistent with the SM expectations at NLO. CDF searches for anomalous $WW\gamma$ and WWZ couplings using the observed leading charged-lepton p_T spectrum (see Fig. 19). In the D0 analysis, the subleading (trailing) lepton p_T is also included in a 2D histogram with the leading lepton

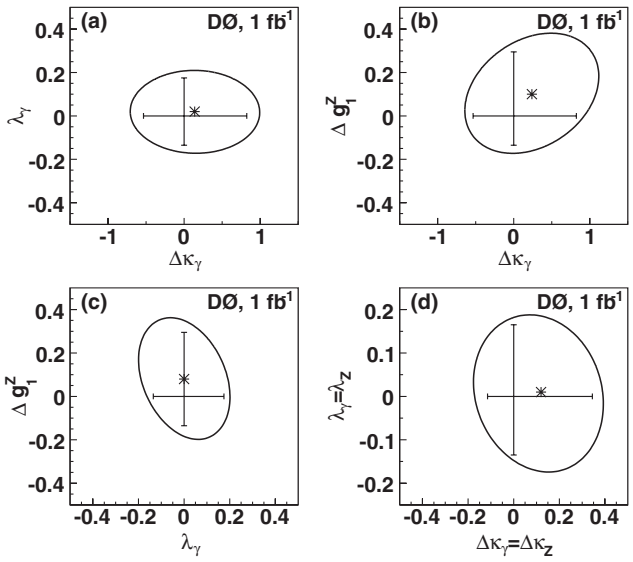

FIG. 21. One- and two-dimensional 95% C.L. limits for the D0 $WW \to \ell\nu\ell\nu$ analysis (Abazov *et al.*, 2009e) when enforcing $SU(2)_L \otimes U(1)_Y$ symmetry at $\Lambda = 2$ TeV, for (a) $\Delta\kappa_\gamma$ vs λ_γ, (b) $\Delta\kappa_\gamma$ vs Δg_1^Z, and (c) λ_γ vs Δg_1^Z, each when the third free coupling is set to its SM value; limits when enforcing the $WW\gamma = WWZ$ constraints are shown in (d). The curve represents the two-dimensional 95% C.L. contour and the ticks along the axes represent the one-dimensional 95% C.L. limits. An asterisk (*) marks the point with the highest likelihood in the two-dimensional plane.

TABLE XI. Expected and observed limits from the CDF $WW \to \ell\nu\ell\nu$ analysis searching for anomalous TGCs assuming two different values of the form factor scale Λ (Aaltonen *et al.*, 2010a). For each coupling limit set, the two other couplings are fixed at their SM values. Values of the couplings outside of the given observed range are excluded at the 95% confidence level (C.L.).

	Λ (TeV)	$\lambda_\gamma = \lambda_Z$	$\Delta\kappa_\gamma$	Δg_1^Z
Expected	1.5	$(-0.05, 0.07)$	$(-0.23, 0.31)$	$(-0.09, 0.17)$
Observed	1.5	$(-0.16, 0.16)$	$(-0.63, 0.72)$	$(-0.24, 0.34)$
Expected	2.0	$(-0.05, 0.06)$	$(-0.20, 0.27)$	$(-0.08, 0.15)$
Observed	2.0	$(-0.14, 0.15)$	$(-0.57, 0.65)$	$(-0.22, 0.30)$

p_T to constrain possible anomalous couplings (see Fig. 20 for the 1D projections).

There are several ways to relate the $WW\gamma$ and WWZ couplings in the presence of new physics. This is a convenient prescription to reduce the number of parameters since WW production involves both $WW\gamma$ and WWZ couplings. Enforcing $SU(2)_L \otimes U(1)_Y$ symmetry introduces two relationships between the remaining parameters: $\kappa_Z = g_1^Z - (\kappa_\gamma - 1)\tan^2\theta_W$ and $\lambda_Z = \lambda_\gamma$, reducing the number of free parameters to three (De Rujula *et al.*, 1992; Hagiwara *et al.*, 1993). Alternatively, enforcing equality between the $WW\gamma$ and WWZ vertices ($WW\gamma = WWZ$) such that $\kappa_\gamma = \kappa_Z$, $\lambda_\gamma = \lambda_Z$, and $g_1^Z = 1$ reduces the number of free parameters to two.

In the D0 analysis, the one-dimensional 95% C.L. limits for $\Lambda = 2$ TeV are determined to be $-0.54 < \Delta\kappa_\gamma < 0.83$, $-0.14 < \lambda_\gamma = \lambda_Z < 0.18$, and $-0.14 < \Delta g_1^Z < 0.30$ under the $SU(2)_L \otimes U(1)_Y$ conserving constraints, and $-0.12 < \Delta\kappa_\gamma = \Delta\kappa_Z < 0.35$, with the same λ limits as above, under the $WW\gamma = WWZ$ constraints. One- and two-dimensional 95% C.L. limits are shown in Fig. 21. In the CDF analysis, only 1D limits on the anomalous coupling parameters under the assumption of $SU(2)_L \otimes U(1)_Y$ invariance are reported. The expected and observed 95% confidence limits are shown in Table XI where it is evident that the limits are weaker than expected. The probability of observing these limits in the presence of only SM WW production ranges from 7.1% to 7.6% depending on the coupling parameters (λ_Z, $\Delta\kappa_\gamma$, Δg_1^Z) and are consistent with a statistical fluctuation of SM physics.

5. WZ

The WZ final state is not available in e^+e^- collisions at LEP but can be produced in $p\bar{p}$ collisions at the Tevatron. The study of associated production of a W and Z boson is

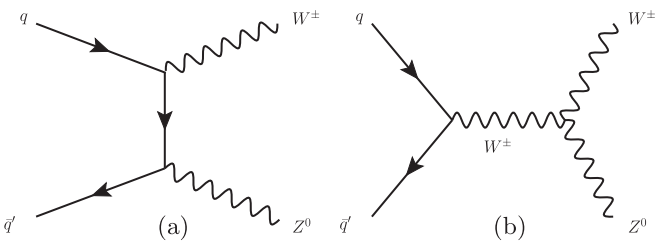

FIG. 22. Leading-order (a) t-channel and (b) s-channel diagrams for WZ production at the Tevatron.

TABLE XII. Expected number of events in the signal region for WZ and the background contributions for the CDF $WZ \to \ell\ell\ell\nu$ analysis (Abulencia *et al.*, 2007b). "Lumi" refers to the integrated luminosity uncertainty, which is absent for the Z + jets because it is determined from the same data set.

Source	Expectation ± stat ± syst ± lumi
Z + jets	$1.21 \pm 0.27 \pm 0.28 \pm -$
ZZ	$0.88 \pm 0.01 \pm 0.09 \pm 0.05$
$Z\gamma$	$0.44 \pm 0.05 \pm 0.15 \pm 0.03$
$t\bar{t}$	$0.12 \pm 0.01 \pm 0.02 \pm 0.01$
Total background	$2.65 \pm 0.28 \pm 0.33 \pm 0.09$
WZ	$9.75 \pm 0.03 \pm 0.31 \pm 0.59$
Total expected	$12.41 \pm 0.28 \pm 0.45 \pm 0.67$
Observed	16

important for a number of reasons. The production of WZ involves the WWZ TGC as shown in the s-channel diagram in Fig. 22. Unlike WW production which involves a combination of the $WW\gamma$ and WWZ couplings such that assumptions regarding their relation must be invoked to interpret any anomalies observed in the data, the WZ production characteristics can be used to make a model-independent test of the SM WWZ coupling. Stated differently, in WZ production measurements, a direct measure of the WZ coupling independent of the $W\gamma$ coupling can be made and compared to the SM predictions. The fully leptonic decay mode of WZ provides a clean SM trilepton signal which is analogous to the so-called *golden mode* for discovering supersymmetry (SUSY) at the Tevatron via chargino-neutralino production $(\tilde{\chi}_1^{\pm}\tilde{\chi}_2^0)$ and decay. Therefore, an observation of the SM WZ trilepton signal represents an important experimental milestone in demonstrating sensitivity to the SUSY golden mode and other new physics signatures in multileptons.

Prior to the start of Run II at the Tevatron, WZ production had not been observed. The NLO WZ cross-section prediction for $p\bar{p}$ collisions at $\sqrt{s} = 1.96$ TeV is 3.7 ± 0.3 pb (Campbell and Ellis, 1999). In October 2006, WZ production was first observed by the CDF Collaboration in the three charged lepton + $\not\!\!E_T$ final state using 1.1 fb^{-1} of integrated luminosity (Abulencia *et al.*, 2007b). The most sensitive previous search for WZ production was reported by the D0 Collaboration using $\int \mathcal{L}dt = 0.3$ fb^{-1}, where three $WZ \to \ell'\nu_{\ell'}\ell\ell$ candidates were found (Abazov *et al.*, 2005c). The observed candidates had a probability of 3.5% to be due to background fluctuations, corresponding to $\sigma(WZ) < 13.3$ pb at 95% C.L. The D0 Collaboration published an update to Abazov *et al.* (2005c) with additional data to measure the WZ production cross section and search for anomalous WWZ couplings (Abazov *et al.*, 2007b).

As with other diboson processes, the signal for WZ production is most easily measured in fully leptonic decay. The experimental signature of WZ production is three isolated high E_T charged leptons, at least two of which have the same flavor and opposite charge with invariant mass consistent with decay of a Z boson, and large $\not\!\!E_T$ consistent with a neutrino from W decay. To observe WZ in fully leptonic decay, high acceptance for charged leptons is required since all three must be detected to suppress backgrounds from larger cross-section processes. In the CDF analysis (Abulencia *et al.*, 2007b), a novel lepton identification strategy was developed to maximize charged-lepton acceptance while keeping the backgrounds comparatively low by exploiting the charge and flavor correlation of identified leptons in the events. The standard electron and muon identification was combined with forward electron candidates beyond the tracking acceptance and a "track-only" lepton category consisting of high-quality tracks that neither project to the fiducial regions of the calorimeters nor are identified as muons by the muon chambers. Because of the lack of calorimeter information, electrons and muons cannot be reliably differentiated for this category and are therefore treated as having either flavor in the WZ candidate selection. For forward electrons without a matched track, both charge hypotheses are considered when forming WZ candidates, since the charge is determined from the track curvature.

Other SM processes that can lead to three high-p_T leptons include dileptons from the DY Z/γ^* process, with an additional lepton from a photon conversion ($Z\gamma$) or a misidentified jet (Z + jets) in the event; ZZ production where only three leptons are identified and the unobserved lepton results in $\not\!\!E_T$; and a small contribution from $t\bar{t} \to WbW\bar{b}$, where two charged leptons result from the W boson decays and one or more from decay of the b quarks. Except for $t\bar{t}$, these

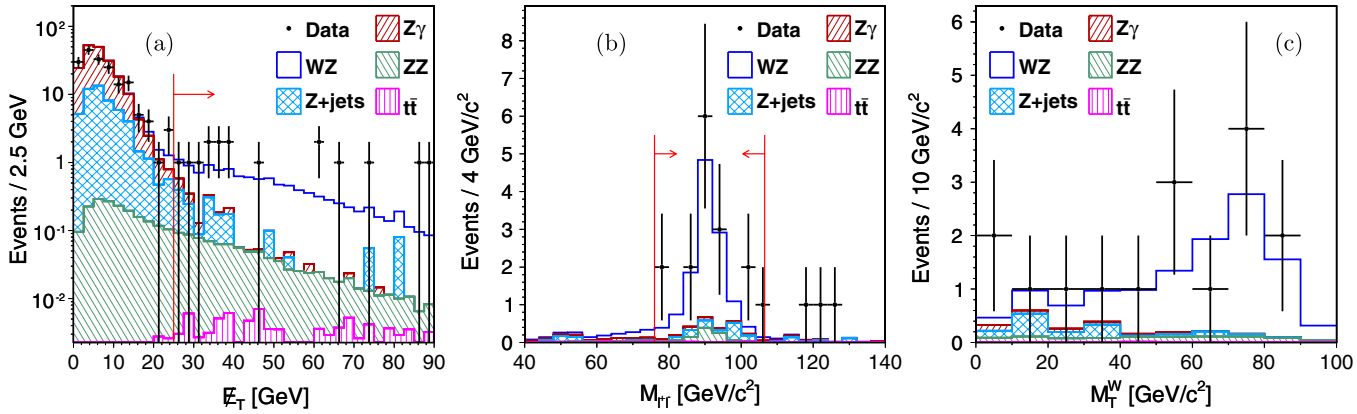

FIG. 23 (color online). Distributions for WZ candidates of (a) the $\not\!\!E_T$, (b) the dilepton invariant mass for the same-flavor opposite-sign dilepton pair closest to the Z mass, and (c) the W transverse mass calculated from the remaining lepton and the $\not\!\!E_T$, for the CDF $WZ \to \ell\ell\ell\nu$ analysis. In (a) and (b), the arrows indicate the signal region. From Abulencia *et al.*, 2007b.

TABLE XIII. Summary of the expected and observed yields for the CDF (Abulencia *et al.*, 2007b) and D0 (Abazov *et al.*, 2007b) $WZ \to \ell\ell\ell\nu$ analyses. In the classification column, ℓ_t denotes a track-only lepton candidate having unknown flavor which is only relevant for the CDF analysis.

Flavor classification	CDF analysis Expected	CDF analysis Data	D0 analysis Expected	D0 analysis Data
$e\ e\ e$	2.7 ± 0.2	6	3.5 ± 0.2	2
$e\ e\ \mu$	2.0 ± 0.2	0	2.7 ± 0.2	1
$e\ \mu\ \mu$	1.5 ± 0.1	1	4.2 ± 0.5	8
$\mu\ \mu\ \mu$	1.2 ± 0.1	1	3.4 ± 0.4	2
$e\ e\ \ell_t$	2.0 ± 0.2	5	⋯	⋯
$e\ \mu\ \ell_t$	1.3 ± 0.1	2	⋯	⋯
$\mu\ \mu\ \ell_t$	1.1 ± 0.1	1	⋯	⋯
$e\ \ell_t\ \ell_t$	0.5 ± 0.1	0	⋯	⋯
$\mu\ \ell_t\ \ell_t$	0.2 ± 0.1	0	⋯	⋯

backgrounds are suppressed by requiring $\not\!\!E_T > 25$ GeV in the event, consistent with the unobserved neutrino from the leptonic decay of a W boson.

Using $\int \mathcal{L}dt = 1.1$ fb^{-1}, 16 events with an expected background of 2.7 ± 0.4 events are observed in the CDF analysis, as shown in Table XII. This corresponds to a 6.0σ observation of WZ production when $\not\!\!E_T$ shape information is included. The measured cross section is

$$\sigma(p\bar{p} \to WZ + X) = 5.0^{+1.8}_{-1.6}(\text{stat} + \text{syst})\ \text{pb},$$

consistent with the NLO expectation. Figure 23 shows some important kinematic distributions for the 16 WZ candidates, which are in good agreement with the SM.

In the D0 analysis (Abazov *et al.*, 2007b), events with three reconstructed, isolated charged leptons (electrons or muons) and $\not\!\!E_T > 20$ GeV were used to measure the WZ production cross section and search for anomalous WWZ couplings using the observed Z boson p_T (p_T^Z) distribution. Each WZ candidate event must contain a like-flavor lepton pair with invariant mass close to the Z boson mass. For eee and $\mu\mu\mu$ decay channels, the lepton pair with invariant mass closest to that of the Z boson mass is chosen to define the Z boson daughter particles. Using $\int \mathcal{L}dt = 1.0$ fb^{-1}, a total of 13 WZ candidates are observed with 4.5 ± 0.6 expected background events and 9.2 ± 1.0 expected WZ signal events, corresponding to a 3.0σ signal significance. The breakdown by trilepton flavor classification for both the CDF and D0 analyses is shown in Table XIII. Figure 24 shows $\not\!\!E_T$ versus the dilepton invariant mass for the background, the expected WZ signal, and the data, including the candidates for the D0 analysis. The WZ production cross section measured by D0 is

$$(p\bar{p} \to WZ + X) = 2.7^{+1.7}_{-1.3}(\text{stat} + \text{syst})\ \text{pb},$$

where the $\pm 1\sigma$ uncertainties are the 68% C.L. limits from the minimum of the negative log likelihood. The uncertainty is dominated by the statistics of the number of observed events.

The three CP-conserving WWZ coupling parameters λ_Z, Δg_1^Z, and $\Delta\kappa_Z$ are constrained in the D0 analysis by comparing the measured cross section and p_T^Z distribution to models with anomalous couplings. A comparison of the observed Z boson p_T distribution with predictions from Monte Carlo simulation is shown in Fig. 25. Table XIV presents the one-dimensional 95% C.L. limits on λ_Z, Δg_1^Z, and $\Delta\kappa_Z$. Figure 26 presents the two-dimensional 95% C.L. limits under the assumption $\Delta g_1^Z = \Delta\kappa_Z$ for $\Lambda = 2$ TeV.

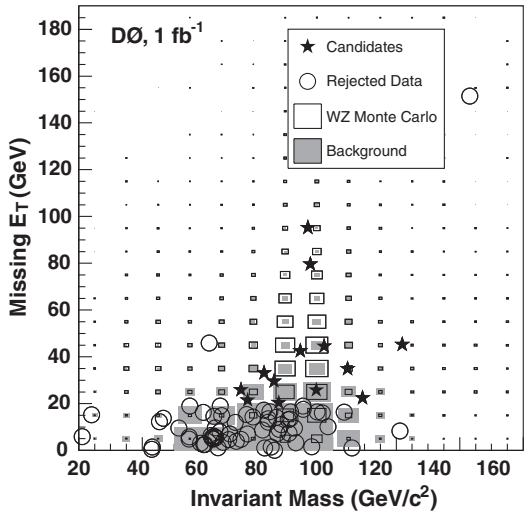

FIG. 24. $\not\!\!E_T$ vs dilepton invariant mass of $WZ \to \ell\ell\ell\nu$ candidate events in the D0 WZ analysis (Abazov *et al.*, 2007b). The open boxes represent the expected WZ signal. The filled boxes represent the sum of the estimated backgrounds. The stars are the data that survive all selection criteria. The open circles are data that either fail the dilepton invariant mass criterion or have $\not\!\!E_T < 20$ GeV.

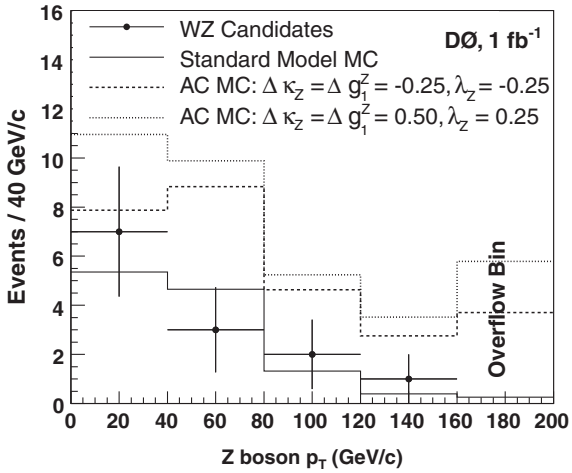

FIG. 25. The reconstructed Z boson p_T of the WZ candidate events for the D0 $WZ \to \ell\ell\ell\nu$ analysis (Abazov *et al.*, 2007b). The solid histogram is the expected sum of signal and background for the case of the WWZ coupling parameters set to their SM values. The dotted and double-dotted histograms are the expected sums of signal and background for two different cases of anomalous WWZ coupling parameter values.

TABLE XIV. One-dimensional 95% C.L. intervals on λ_Z, Δg_1^Z, and $\Delta\kappa_Z$ for two sets of form factor scale Λ for the D0 $WZ \to \ell\ell\ell\nu$ analysis (Abazov *et al.*, 2007b).

$\Lambda = 1.5$ TeV	$\Lambda = 2.0$ TeV
$-0.18 < \lambda_Z < 0.22$	$-0.17 < \lambda_Z < 0.21$
$-0.15 < \Delta g_1^Z < 0.35$	$-0.14 < \Delta g_1^Z < 0.34$
$-0.14 < \Delta\kappa_Z = \Delta g_1^Z < 0.31$	$-0.12 < \Delta\kappa_Z = \Delta g_1^Z < 0.29$

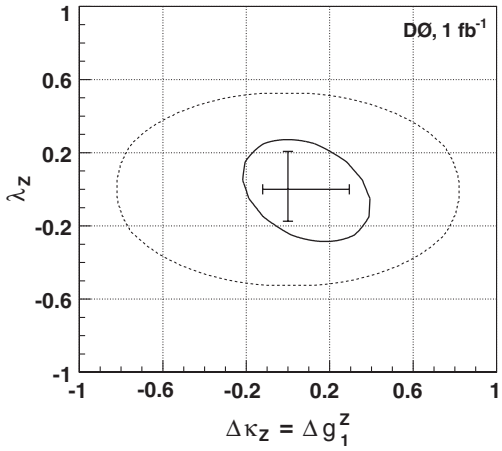

FIG. 26. Two-dimensional 95% C.L. contour limit in $\Delta g_1^Z = \Delta\kappa_Z$ vs $\Delta\lambda_Z$ space (inner contour) for the D0 $WZ \to \ell\ell\ell\nu$ analysis (Abazov *et al.*, 2007b). The form factor scale for this contour is $\Lambda = 2$ TeV. The physically allowed region (unitarity limit) is bounded by the outer contour. The cross hairs are the 95% C.L. one-dimensional limits.

6. ZZ

The production of Z pairs is predicted within the SM to have the smallest cross section among the diboson processes. It has been observed in e^+e^- collisions at LEP (Alcaraz *et al.*, 2006), but not in hadron collisions as of the start of the Tevatron Run-II. As a window to new physics, ZZ production is particularly interesting because of the absence of $ZZ\gamma$ and ZZZ couplings in the SM (see Fig. 27), and because of the very low backgrounds in the four charged-lepton channel. Higgs-boson decay can contribute to ZZ production; however, this channel is generally not competitive with $H \to WW^{(*)}$ as a discovery channel at the Tevatron collision energy and integrated luminosity.

As is the case for WW and WZ production, the ZZ state is most easily observed in the fully leptonic mode at a hadron collider. The $ZZ \to \ell\ell\ell\ell$ process is rare but predicted to be nearly background free in the SM, with Z + jets (jets reconstructed as charged leptons) as the only non-negligible background. Having large total charged-lepton acceptance in the experiments is crucial due to the high lepton multiplicity in the final state. The $ZZ \to \ell\ell\nu\nu$ process can also contribute sensitivity to the search for ZZ production although it suffers from large continuum WW backgrounds. The full SM process is $p\bar{p} \to Z/\gamma^* Z/\gamma^*$, where the two Z/γ^* interfere with one

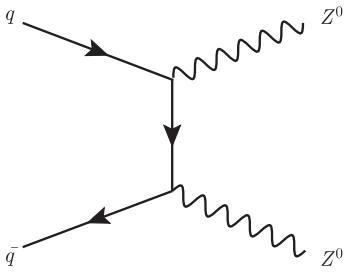

FIG. 27. Leading-order diagram for ZZ production at the Tevatron. The s-channel diagram involving the neutral TGC is absent in the SM.

another. For brevity, we denote $Z/\gamma^* Z/\gamma^*$ as ZZ throughout and indicate the dilepton invariant mass range(s), where applicable. The NLO ZZ cross section for $p\bar{p}$ collisions at $\sqrt{s} = 1.96$ TeV is 1.4 ± 0.1 pb in the zero-width Z boson approximation (Campbell and Ellis, 1999).

Using $\int \mathcal{L}dt = 1$ fb^{-1}, the D0 Collaboration searched for $ZZ \to \ell\ell\ell\ell$ production and set a limit on the cross section of $\sigma(ZZ) < 4.4$ pb at 95% C.L. (Abazov *et al.*, 2008c). They constrain possible $ZZ\gamma$ and ZZZ couplings based on the observed four lepton yield with the added requirement that $M(\ell\ell) > 50$ (70) for electrons (muons). The value of the cut was chosen based on the dilepton invariant mass resolution. This lower $M(\ell\ell)$ requirement was included because the Monte Carlo generator (Baur and Rainwater, 2000) used to constrain possible anomalous couplings does not include contributions from off-shell Z bosons. Without the $M(\ell\ell)$ cut, one $\mu\mu ee$ event is observed in the data. This event is removed by the $M(\ell\ell)$ cut used to constrain anomalous couplings. 1D and 2D limits on anomalous $ZZ\gamma$ and ZZZ couplings are determined using $\Lambda = 1.2$ TeV. The 95% C.L. 1D limits are $-0.28 < f_{40}^Z < 0.28$, $-0.26 < f_{40}^\gamma < 0.26$, $-0.31 < f_{50}^Z < 0.29$, and $-0.30 < f_{50}^\gamma < 0.28$. The 95% C.L. 2D contours f_{40}^γ vs f_{40}^Z, f_{40}^γ vs f_{50}^γ, f_{40}^Z vs f_{50}^Z, and f_{50}^γ vs f_{50}^Z are shown in Fig. 28.

The CDF Collaboration uses $\int \mathcal{L}dt = 1.9$ fb^{-1} to search for ZZ production in a combination of the $ZZ \to \ell\ell\ell\ell$ and $ZZ \to \ell\ell\nu\nu$ channels (Aaltonen *et al.*, 2008b). To maximize the acceptance, lepton candidates are constructed out of all reconstructed tracks and energy clusters in the EM section of the calorimeter. This is done with the same lepton identification criteria used in a previous CDF measurement of WZ production (Abulencia *et al.*, 2007b). The $ZZ \to \ell\ell\ell\ell$ candidates are selected from events with exactly four charged-lepton candidates and at least two same-flavor, opposite-sign lepton pairs are required for the event to be accepted. As in the WZ analysis, trackless electrons are considered to have either charge, and track-only leptons either flavor. One pair must have invariant mass $M_{\ell^+\ell^-}$ in the range $[76, 106]$ GeV$/c^2$, while the requirement for the other pair is extended to $[40, 140]$ GeV$/c^2$ to increase the acceptance for off-shell Z decays.

The $ZZ \to \ell\ell\ell\ell$ candidate events are separated into two exclusive categories based on whether or not they contain at least one forward electron without a track. This is done because the background from $Z\gamma$ + jets is much larger in candidates with a forward trackless electron. The expected signal, expected background, and observed yields are shown in Table XV.

The $ZZ \to \ell\ell\nu\nu$ candidates are selected from events with exactly two oppositely charged lepton candidates excluding events with forward electrons without a track which are contaminated by large $W\gamma$ backgrounds. Aside from ZZ production, other SM processes that can lead to two high-p_T leptons include events from DY, a W decay with photon ($W\gamma$) or jet (W + jets) misidentified as a lepton; and $t\bar{t}$, WW, and WZ production.

There are 276 events after the event selection (which contains a specialized high $\not{E}_T$ to suppress primarily DY) of which only 14 ± 2 are expected to be from the $ZZ \to \ell\ell\nu\nu$ process in the SM. Approximately half of the yield is

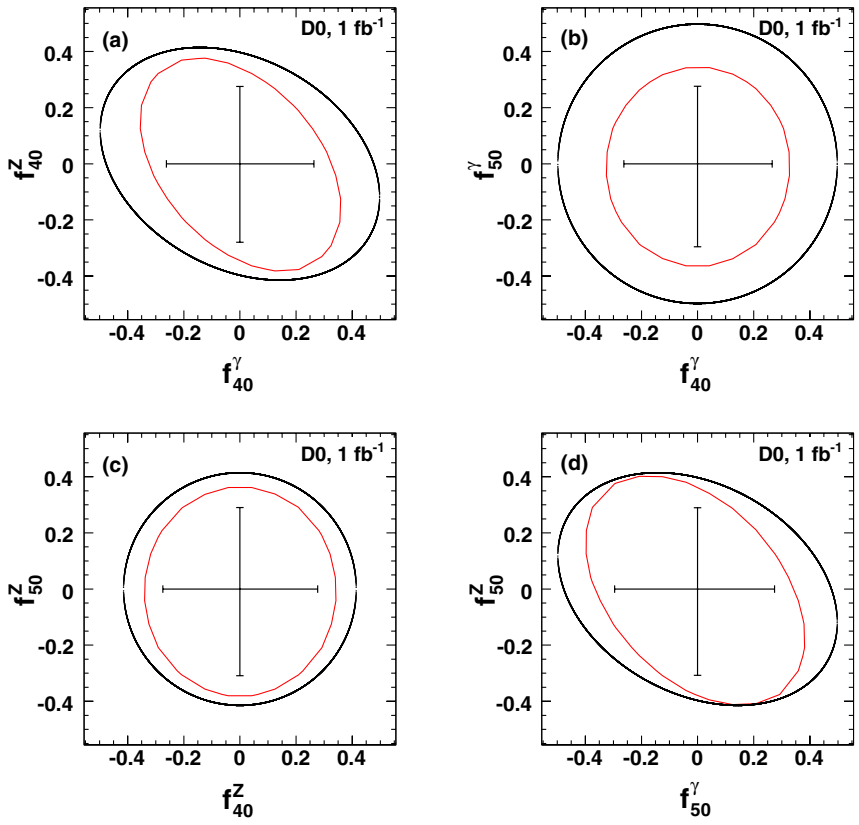

FIG. 28 (color online). Limits on anomalous couplings for $\Lambda = 1.2$ TeV for the D0 $ZZ \to \ell\ell\ell\ell$ analysis (Abazov *et al.*, 2008c): (a) f_{40}^{γ} vs f_{40}^{Z}, (b) f_{40}^{γ} vs f_{50}^{γ}, (c) f_{40}^{Z} vs f_{50}^{Z}, and (d) f_{50}^{γ} vs f_{50}^{Z}, assuming in each case that the other two couplings are zero. The inner and outer curves are the 95% C.L. 2 degree of freedom exclusion contour and the constraint from the unitarity condition, respectively. The inner cross hairs are the 95% C.L. 1 degree of freedom exclusion limits.

expected to be due to the WW process. However, $ZZ \to \ell\ell\nu\nu$ and WW have different kinematic properties which are exploited to statistically separate the contribution of these two processes to the data. The approach used by CDF is identical to that used in the WW cross-section measurement described in Sec. III.E.4. An event-by-event probability density is calculated for the observed lepton momenta and $\not{E}_T$ using leading-order calculations of the differential decay rate for the processes (Campbell and Ellis, 1999). A likelihood ratio discriminant LR is formed which is the signal probability divided by the sum of signal and background probabilities $LR = P_{ZZ}/(P_{ZZ} + P_{WW})$. The distribution of $\log_{10}(1 - LR)$ for the data compared to the summed signal and background expectation is shown in Fig. 29.

The $ZZ \to \ell\ell\ell\ell$ and $ZZ \to \ell\ell\nu\nu$ results were combined through a likelihood fit which includes the two 4-lepton bins and the $\log_{10}(1 - LR)$ distribution for the dileptons. The p value for the $ZZ \to \ell\ell\nu\nu$ alone is 0.12 and the combined p value is 5.1×10^{-6} corresponding to a significance equivalent to 4.4 standard deviations. The ZZ cross section is obtained by fitting the data for the fraction of the expected

TABLE XV. Expected and observed number of $ZZ \to \ell\ell\ell\ell$ candidate events for the CDF ZZ analysis (Aaltonen *et al.*, 2008b). The first uncertainty is statistical and the second one is systematic.

Category	Candidates without a trackless electron	Candidates with a trackless electron
ZZ	$1.990 \pm 0.013 \pm 0.210$	$0.278 \pm 0.005 \pm 0.029$
Z + jets	$0.014^{+0.010}_{-0.007} \pm 0.003$	$0.082^{+0.089}_{-0.060} \pm 0.016$
Total	$2.004^{+0.016}_{-0.015} \pm 0.210$	$0.360^{+0.089}_{-0.060} \pm 0.033$
Observed	2	1

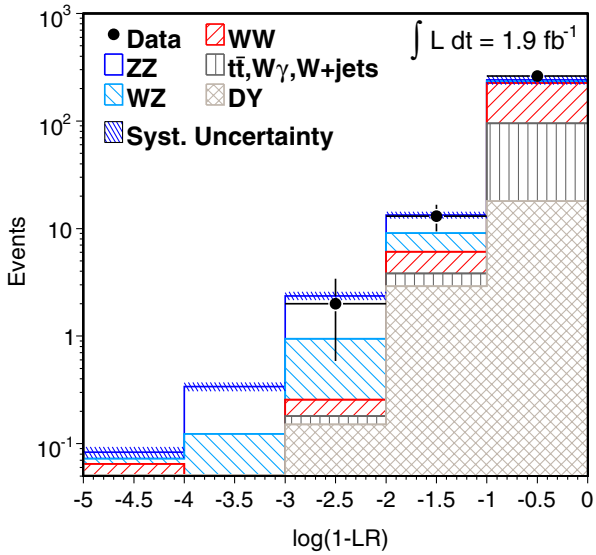

FIG. 29 (color online). Distribution of the discriminating variable $\log_{10}(1 - LR)$ for the CDF $ZZ \to \ell\ell\nu\nu$ search. From Aaltonen *et al.*, 2008b.

TABLE XVI. The integrated luminosity, expected number of signal ($Z/\gamma^* Z/\gamma^*$) and background events [$t\bar{t}$ and $Z(\gamma)$ + jets which includes all $W/Z/\gamma$ + jets contributions], and the number of observed candidates in the seven $ZZ \to \ell^+\ell^-\ell'^+\ell'^-$ subchannels for the D0 $ZZ \to \ell\ell\ell\ell$ analysis (Abazov *et al.*, 2008d). Uncertainties reflect statistical and systematic contributions added in quadrature.

Subchannel	$4e_{2C}$	$4e_{3C}$	$4e_{4C}$	4μ	$2\mu 2e_{0C}$	$2\mu 2e_{1C}$	$2\mu 2e_{2C}$
Luminosity (fb^{-1})	1.75 ± 0.11	1.75 ± 0.11	1.75 ± 0.11	1.68 ± 0.10	1.68 ± 0.10	1.68 ± 0.10	1.68 ± 0.10
Signal	0.084 ± 0.008	0.173 ± 0.015	0.140 ± 0.012	0.534 ± 0.043	$0.058^{+0.007}_{-0.006}$	0.352 ± 0.040	$0.553^{+0.045}_{-0.044}$
$Z(\gamma)$ + jets	$0.030^{+0.009}_{-0.008}$	$0.018^{+0.008}_{-0.007}$	$0.002^{+0.002}_{-0.001}$	0.0003 ± 0.0001	$0.03^{+0.02}_{-0.01}$	0.05 ± 0.01	$0.008^{+0.004}_{-0.003}$
$t\bar{t}$	...	...	...	...	$0.0012^{+0.0016}_{-0.0009}$	0.005 ± 0.002	$0.0007^{+0.0009}_{-0.0005}$
Observed events	0	0	2	1	0	0	0

SM yield in the full acceptance and scaling the zero-width Z boson approximation cross section by that fraction. The measured cross section is $\sigma(p\bar{p} \to ZZ) = 1.4^{+0.7}_{-0.6}$ pb, consistent with the SM expectation. This is the first evidence of a ZZ signal with greater than 4σ significance in hadron collisions.

The D0 Collaboration uses $\int \mathcal{L}dt = 1.7$ fb^{-1} to search for ZZ production in the $ZZ \to \ell\ell\ell\ell$ channel (Abazov *et al.*, 2008d). This analysis follows up the analysis from Abazov *et al.* (2008c) using more data and tighter dilepton invariant mass requirements but does not explicitly search for anomalous couplings. Four lepton events are selected using identified muons with $|\eta| < 2$ and electrons that are either central ($|\eta| < 1.1$) or forward $1.5 < |\eta| < 3.2$. It is required that one pair have the same flavor with invariant mass >70 GeV$/c^2$ and another pair have invariant mass >50 GeV$/c^2$.

Table XVI summarizes the expected signal and background contributions to each subchannel, as well as the number of candidate events in data. The total signal and background expectations are 1.89 ± 0.08 events and $0.14^{+0.03}_{-0.02}$ events, respectively. A total of three candidate events is observed, with two in the $4e_{4C}$ subchannel ("C" refers to the number of central leptons) and one in the 4μ subchannel. Figure 30 shows the distribution of the four lepton invariant mass for data and for the expected signal and background.

Using a log-likelihood ratio test statistic of the yields and pseudoexperiments, the p value is determined to be

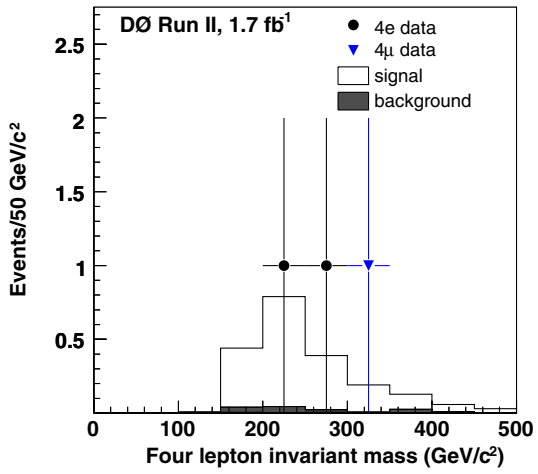

FIG. 30 (color online). Distribution of four lepton invariant mass in data, expected signal, and expected background for the D0 $ZZ \to \ell\ell\ell\ell$ analysis. From Abazov *et al.*, 2008d.

4.3×10^{-8} which corresponds to a 5.3σ observed significance (3.7σ expected). The measured cross section in the $ZZ \to \ell\ell\ell\ell$ channel is

$$\sigma(ZZ + X) = 1.75^{+1.27}_{-0.86}(\text{stat}) \pm 0.13(\text{syst}) \text{ pb}.$$

This result is combined with the results from an independent $ZZ \to \ell\ell\nu\nu$ search (Abazov *et al.*, 2008e), and the previous $ZZ \to \ell\ell\ell\ell$ analysis (Abazov *et al.*, 2008c) taking into account the systematic uncertainty correlations between subchannels and among analyses. The resulting p value is 6.2×10^{-9}, and the significance for observation of ZZ production increases to 5.7σ (4.8σ expected). This is the first observation of ZZ production at a hadron collider. The combined cross section is

$$\sigma(ZZ + X) = 1.60 \pm 0.63(\text{stat})^{+0.16}_{-0.17}(\text{syst}) \text{ pb},$$

consistent with the SM expectation.

7. WV ($V = W, Z$)

The production of vector boson pairs (WW, WZ, and ZZ) has been observed at the Tevatron in decay modes where both vector bosons decay leptonically. The semileptonic decay modes where one of the vector boson decays hadronically have larger branching fraction as compared to the fully leptonic modes but significantly larger backgrounds from jets produced in association with a W boson. As a result, simple event counting above background cannot be used to observe dibosons in semileptonic decay at the Tevatron and advanced analysis techniques utilizing multivariate (MV) event classification are required to statistically separate signal from background. Analysis of the $\ell\nu jj$ final state provides an excellent test bed for such advanced techniques to extract small signals from large backgrounds in real hadron collision data that has great relevance to Higgs-boson (e.g., $WH \to \ell\nu b\bar{b}$) and new physics searches in final states involving jets. In addition, semileptonic diboson decay can provide a more sensitive search for anomalous trilinear gauge couplings than fully leptonic decay modes since anomalous TGCs enhance production at high gauge boson momentum where the signal-to-background ratio improves.

The dijet mass resolution of the CDF and D0 detectors is not good enough to distinguish hadronically decaying W bosons and Z bosons. As a result, the search for diboson production in the $\ell\nu jj$ final state is a search for the sum of WW and WZ production. The experimental signature of the $WW + WZ$ signal in semileptonic decay is one isolated high

E_T charged lepton, large $\not\!\!E_T$ from the neutrino produced in W decay, and at least two high E_T jets.

In principle, one could search for SM $WZ + ZZ$ production in the $jj\ell\ell$ channel. Large Z + jets backgrounds makes this a very difficult channel to observe the SM signal, although the use of b tagging can improve the sensitivity. The use of the $b\bar{b}\ell\ell$ channel to search for associated Higgs-boson production is described in Sec. V.B.2.

Both D0 and CDF searched for $WW + WZ$ production and anomalous $WW\gamma$, WWZ couplings in the $\ell\nu jj$ final state (Aaltonen *et al.*, 2007a, 2010b; Abazov *et al.*, 2009f, 2009g). In these analyses, W + jets is the dominant background. Other significant backgrounds include Z + jets, $t\bar{t}$, single-top quark, and QCD multijet production. Backgrounds are suppressed by requiring a minimum W transverse mass $M_T(W)$ in each event, which is the transverse mass of the charged lepton and $\not\!\!E_T$ system.

The strategy for extracting the semileptonic $WW + WZ$ signal yield after basic event selection differs between the D0 and CDF analyses. In the D0 analysis (Abazov *et al.*, 2009f), thirteen kinematic variables (e.g., dijet mass) demonstrating a sensitivity to distinguish signal and background are used as input to a random forest (RF) (Breiman, 2001) multivariate event classifier using $\int \mathcal{L}dt = 1.1$ fb^{-1}. Figure 31 shows the

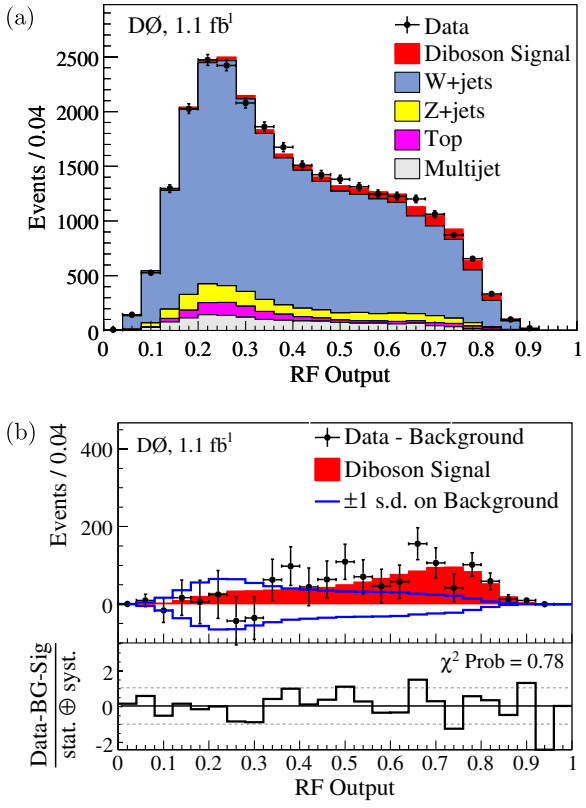

FIG. 31 (color online). For the D0 analysis (Abazov *et al.*, 2009f), (a) the RF output distribution from the combined $e\nu q\bar{q}$ and $\mu\nu q\bar{q}$ channels for data and simulated event predictions following the fit of simulation to data. (b) A comparison of the extracted signal (filled histogram) to background-subtracted data (points), along with the ±1 standard deviation (s.d.) systematic uncertainty on the background. The residual distance between the data points and the extracted signal, divided by the total uncertainty, is given at the bottom.

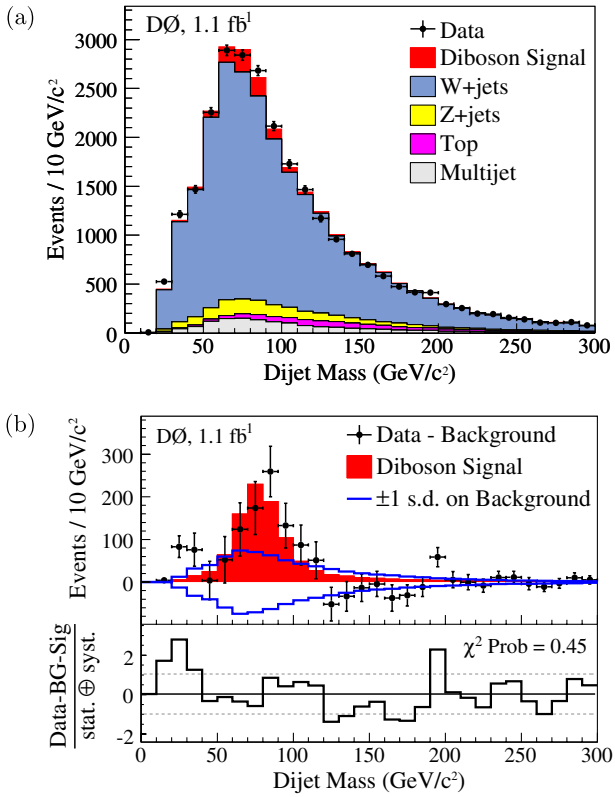

FIG. 32 (color online). For the D0 analysis, (a) the dijet mass distribution from the combined $e\nu q\bar{q}$ and $\mu\nu q\bar{q}$ channels for data and simulated event predictions following the fit to the RF output. (b) A comparison of the extracted signal (filled histogram) to background-subtracted data (points), along with the ±1 standard deviation (s.d.) systematic uncertainty on the background. The residual distance between the data points and the extracted signal, divided by the total uncertainty, is given at the bottom. From Abazov *et al.*, 2009f.

RF output distribution after a fit to the WV signal and W + jets background contributions. Figure 32 shows the dijet mass distribution using the results of the RF output fit. The dominant systematic uncertainties arise from the modeling of the W + jets background and the jet energy scale (JES). The probability for the background to fluctuate to give an excess as large as that observed in the data is $<5.4 \times 10^{-6}$, corresponding to a 4.4σ signal significance. This result is the first evidence for WV production in lepton + jets events at a hadron collider. The measured cross section is

$$\sigma(WV + X) = 20.2 \pm 4.5(\text{stat} + \text{syst})\ \text{pb}$$

consistent with the NLO SM cross section of 16.1 ± 0.9 pb (Campbell and Ellis, 1999).

In the CDF analysis (Aaltonen *et al.*, 2010b), two different methods are used to extract the $WW + WZ$ signal from the data. In the first method (“dijet method”), the dijet invariant mass M_{jj} is used to extract a signal peak from data corresponding to $\int \mathcal{L}dt = 3.9$ fb^{-1}. The second method (“ME method”) takes advantage of more kinematic information in the event by constructing a discriminant based on calculations of the differential cross sections of the signal and background processes data corresponding to $\int \mathcal{L}dt = 2.7$ fb^{-1}. The ME method was discussed in Sec. III.E.4 where

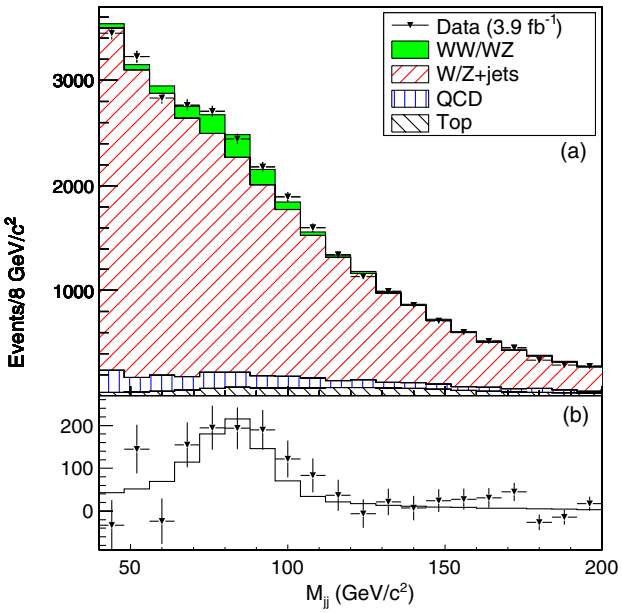

FIG. 33 (color online). For the CDF analysis, the (a) dijet invariant mass distribution of reconstructed $W/Z \to jj$ candidates compared to the fitted signal and background components, and (b) corresponding background-subtracted distribution. From Aaltonen *et al.*, 2010b.

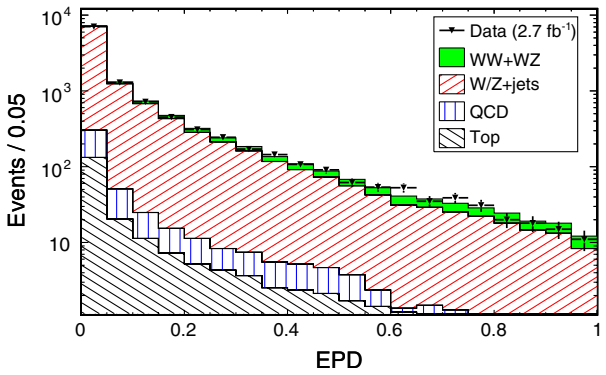

FIG. 34 (color online). Observed EPD distribution superimposed on distribution expected from simulated processes for the CDF analysis. From Aaltonen *et al.*, 2010b.

it was used in the $WW \to \ell\nu\ell\nu$ analysis and has been used in a number of different CDF and D0 analyses.

The normalization of the Z + jets background is based on the measured cross section (Acosta *et al.*, 2005d). The $t\bar{t}$ and single-top background normalizations are from the NLO predicted cross sections (Cacciari *et al.*, 2008). The efficiencies for the Z + jets, $t\bar{t}$, and single-top backgrounds are estimated from simulation. The normalization of the multijet background is estimated by fitting the $\not\!\!E_T$ spectrum in data to the sum of all contributing processes, where the multijet and W + jets normalizations float in the fit. In the final signal extractions from both methods, the multijet background is Gaussian constrained to the result of this $\not\!\!E_T$ fit and the W + jets background is left unconstrained.

In the dijet method, the signal fraction in the data is estimated by performing a χ^2 fit to the dijet invariant mass spectrum, separately for electron and muon events. Figure 33 shows the dijet invariant mass distribution of data compared to the fitted signal and background contributions. The observed (expected) signal significance using the dijet method is 4.6σ (4.9σ) for electrons and muons combined. The measured cross section is

$$\sigma(WV + X) = 14.4 \pm 3.1(\text{stat}) \pm 2.2(\text{syst}) \text{ pb}.$$

In the ME method, the calculated event probabilities are combined into an event probability discriminant EPD $= P_{\text{signal}}/(P_{\text{signal}} + P_{\text{background}})$, where $P_{\text{signal}} = P_{WW} + P_{WZ}$ and $P_{\text{background}} = P_{W+\text{jets}} + P_{\text{singletop}}$. Templates of the EPD generated for all signal and background processes are used in a binned likelihood fit for the signal yield observed in the data, as shown in Fig. 34. Figure 35 shows the dijet mass in bins of EPD, where it can be seen that the low EPD bin contains very little signal as compared to background. Events with EPD > 0.25 have a dijet mass peak close to the expected W/Z mass, and the signal-to-background ratio improves with increasing EPD. The observed (expected) signal significance using the ME method is 5.4σ (5.1σ) which represents the first observation of $WW + WZ$ production in the lepton + jets channel. The measured cross section using the ME method is

$$\sigma(WV + X) = 17.7 \pm 3.1(\text{stat}) \pm 2.4(\text{syst}) \text{ pb}.$$

In the M_{jj} method the largest systematic uncertainties are due to the modeling of the EW and multijet shapes, about 8% and 6%, respectively. In the ME method the uncertainty in the jet energy scale is the largest systematic uncertainty, at about 10%, which includes contributions from both the signal acceptance and the shapes of the signal templates. In the M_{jj} method this uncertainty is about 6%. The combined cross section for the dijet and ME methods, with consideration of statistical and systematic uncertainties, is

$$\sigma(WV + X) = 16.0 \pm 3.3(\text{stat} + \text{syst}) \text{ pb}.$$

Both of the CDF and D0 $WW + WZ$ cross-section measurements are consistent with the SM NLO expectations. In Aaltonen *et al.* (2007a), CDF searches for anomalous $WW\gamma$ and WWZ couplings using the observed spectrum of the charged lepton p_T from a W decay and $\int \mathcal{L}dt = 0.35$ fb^{-1}. Figure 36 shows good consistency between the SM expectation for W boson p_T and the data which are used to constrain possible anomalous couplings. In order to increase the sensitivity to anomalous couplings, these data are combined with the photon E_T spectrum from the $W\gamma$ analysis (Acosta *et al.*, 2005b) described in Sec. III.E.2 that constrains possible anomalous $WW\gamma$ couplings. Table XVII summarizes the resulting anomalous coupling limits under the assumption of equal $WW\gamma$ and WWZ couplings.

The D0 search for anomalous couplings in the $\ell\nu jj$ channel (Abazov *et al.*, 2009g) is based on the same data that were used to obtain the first evidence for semileptonic decays of WW/WZ boson pairs in hadron collisions (Abazov *et al.*, 2009f). In contrast to the CDF analysis just described, the D0 analysis uses the dijet p_T information

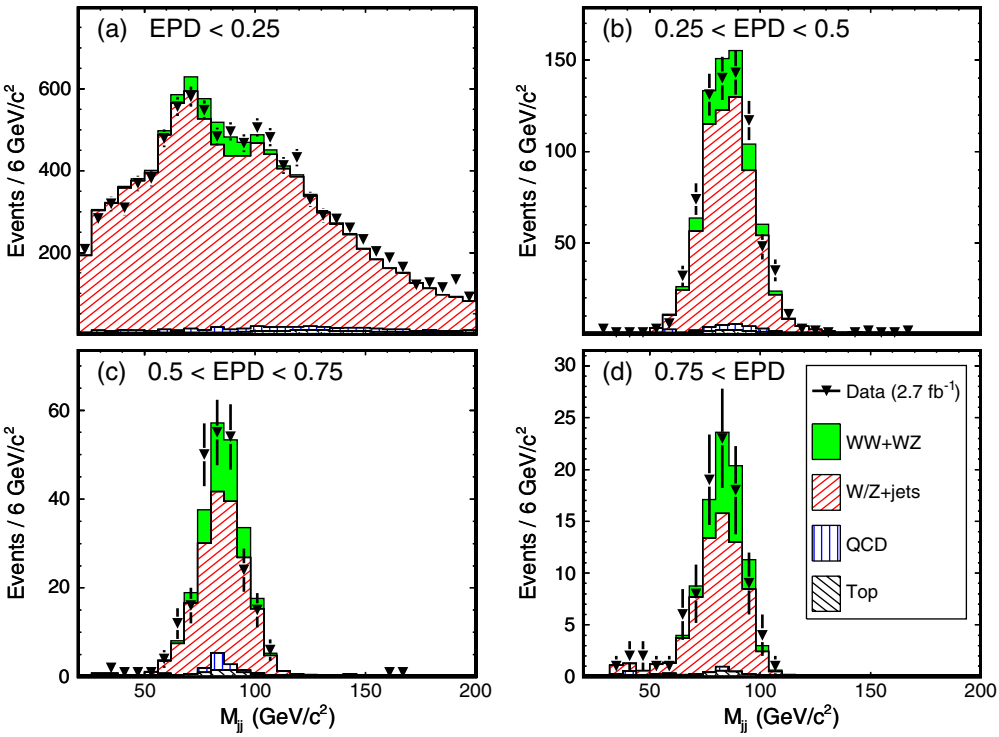

FIG. 35 (color online). For the CDF analysis, M_{jj} for events with (a) EPD <0.25, (b) $0.25<$ EPD <0.5, (c) $0.5<$ EPD <0.75, and (d) EPD >0.75. From Aaltonen *et al.*, 2010b.

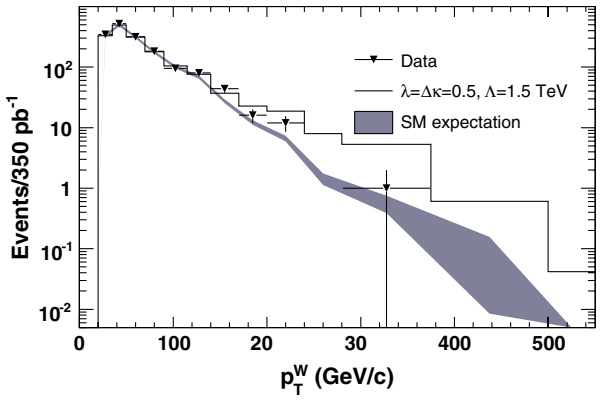

FIG. 36 (color online). The p_T^W distribution used for setting the anomalous TGC limits in the CDF analysis. Shown are the SM expectation, data points, and one anomalous coupling scenario with $\lambda=\Delta\kappa=0.5$ and $\Lambda=1.5$ TeV. From Aaltonen *et al.*, 2007a.

to place limits on $WW\gamma/Z$ anomalous couplings. Figure 37 shows the dijet p_T distribution after a fit for the individual signal and background contributions. No excess at high dijet p_T that would suggest that nonstandard couplings are present is evident in the data. The one-dimensional 95% C.L. limits for the $WW\gamma/Z$ anomalous coupling parameters under separate assumptions of $SU(2)_L\otimes U(1)_Y$ symmetry and equal $WW\gamma$ and WWZ couplings are shown in Table XVIII. The 2D limits under the assumption of $SU(2)_L\otimes U(1)_Y$ symmetry (Hagiwara *et al.*, 1993) are shown in Fig. 38 and for equal coupling assumption they are shown in Fig. 39.

8. VV ($V=W,Z$)

In Secs. III.E.4, III.E.5, and III.E.6, we summarized the observations of heavy vector boson pairs (WW, WZ, ZZ) when each boson decays to one or more charged leptons. In Sec. III.E.7, the measurements of a hadronically decaying heavy vector boson produced in association with a W boson that decays to a charged lepton and a neutrino were described. Observing diboson production in semileptonic decay mode required sophisticated analysis techniques because of overwhelming $W+$ jets in addition to the presence of a $WW+WZ$ signal. The approach of searching for diboson production in a more inclusive way can be taken a step further by dropping the requirement of a reconstructed charged lepton and instead looking at the $\not{E}_T+$ jets final state. This approach includes an additional contribution from $Z\to\nu\nu$ over the $WW/WZ\to\ell\nu jj$ mode so that it measures $WW+WZ+ZZ$ production and allows for an event with a diboson decay to be accepted even if one or more charged leptons fail a selection cut. The experimental challenge is that this mode requires a tighter $\not{E}_T$ cut as compared to $WW/WZ\to\ell\nu jj$

TABLE XVII. Allowed anomalous coupling ranges for $\Lambda=1.5$ TeV at 95% C.L., fixing the other coupling to the SM value and assuming equal $WW\gamma$ and WWZ couplings for the CDF analysis (Aaltonen *et al.*, 2007a).

	λ	$\Delta\kappa$
$\ell\nu jj$	$(-0.28, 0.28)$	$(-0.50, 0.43)$
$\ell\nu\gamma$[a]	$(-0.21, 0.19)$	$(-0.74, 0.73)$
Combined	$(-0.18, 0.17)$	$(-0.46, 0.39)$

[a]Acosta *et al.*, 2005b.

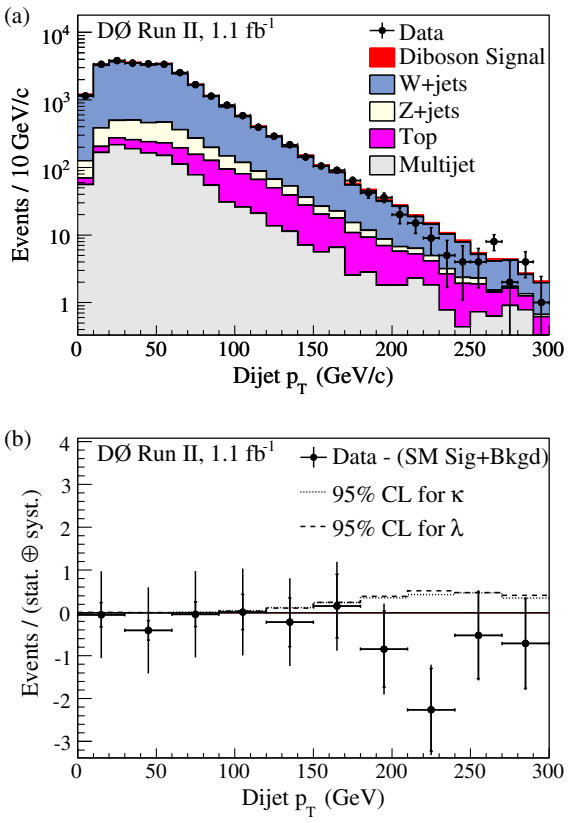

FIG. 37 (color online). For the D0 analysis, the (a) dijet p_T distribution of combined (electron + muon) channels for data and SM predictions following the fit of simulated events to data, and (b) the difference between data and simulation divided by the uncertainty (statistical and systematic) for the dijet p_T distribution. Also shown are the simulated signals for anomalous couplings corresponding to the 95% C.L. limits for $\Delta\kappa$ and λ in the LEP parametrization scenario. The full error bars on the data points reflect the total (statistical and systematic) uncertainty, with the ticks indicating the contribution due only to the statistical uncertainty. From Abazov *et al.*, 2009g.

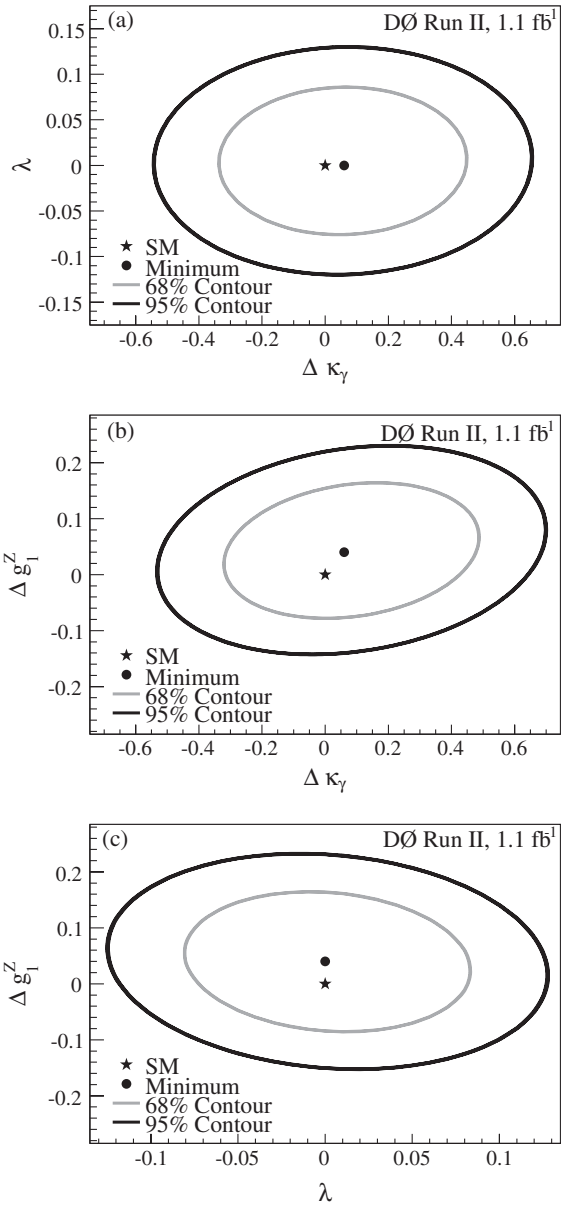

FIG. 38. The 68% C.L. and 95% C.L. two-parameter limits on the $\gamma WW/ZWW$ coupling parameters $\Delta\kappa_\gamma$, λ, and Δg_1^Z, in the LEP parametrization scenario and $\Lambda_{NP} = 2$ TeV for the D0 analysis. The dots indicate the most probable values of anomalous couplings from the two-parameter combined (electron + muon) fit and the star markers denote the SM prediction. From Abazov *et al.*, 2009g.

and a better overall understanding of high reconstructed $\not\!\!E_T$ tails from low true $\not\!\!E_T$ events with a large cross section such as QCD multijets.

The CDF Collaboration uses $\int \mathcal{L}dt = 3.5$ fb^{-1} to search for the production of heavy vector boson pairs (VV, $V = W$, Z) where one boson decays to a dijet final state (Aaltonen *et al.*, 2009a). The most significant

TABLE XVIII. The most probable values with total uncertainties (statistical and systematic) at 68% C.L. for κ_γ, λ, and g_1^Z along with observed 95% C.L. one-parameter limits on $\Delta\kappa_\gamma$, λ, and Δg_1^Z measured in 1.1 fb^{-1} of $WW/WZ \to \ell\nu jj$ events with $\Lambda_{NP} = 2$ TeV for the D0 analysis (Abazov *et al.*, 2009g).

68% C.L.	κ_γ	$\lambda = \lambda_\gamma = \lambda_Z$	g_1^Z
$SU(2)_L \otimes U(1)_Y$ symmetry	$\kappa_\gamma = 1.07^{+0.26}_{-0.29}$	$\lambda = 0.00^{+0.06}_{-0.06}$	$g_1^Z = 1.04^{+0.09}_{-0.09}$
Equal couplings	$\kappa_\gamma = \kappa_Z = 1.04^{+0.11}_{-0.11}$	$\lambda = 0.00^{+0.06}_{-0.06}$	
95% C.L.	$\Delta\kappa_\gamma$	$\lambda = \lambda_\gamma = \lambda_Z$	Δg_1^Z
$SU(2)_L \otimes U(1)_Y$ symmetry	$-0.44 < \Delta\kappa_\gamma < 0.55$	$-0.10 < \lambda < 0.11$	$-0.12 < \Delta g_1^Z < 0.20$
Equal couplings	$-0.16 < \Delta\kappa < 0.23$	$-0.11 < \lambda < 0.11$	

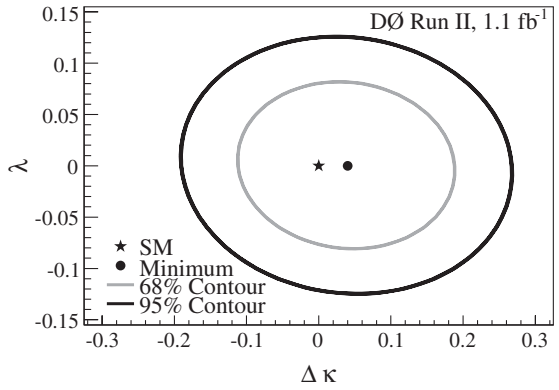

FIG. 39. The 68% C.L. and 95% C.L. two-parameter limits on the $\gamma WW/ZWW$ coupling parameters $\Delta\kappa$ and λ, in the equal couplings scenario and $\Lambda_{NP} = 2$ TeV for the D0 analysis. The dot indicates the most probable values of anomalous couplings from the two-parameter combined (electron + muon) fit and the star marker denotes the SM prediction. From Abazov *et al.*, 2009g.

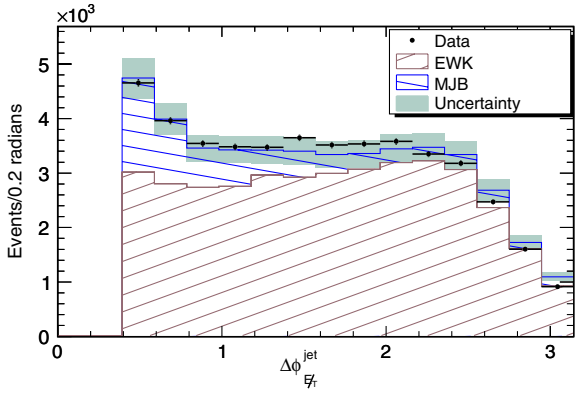

FIG. 40 (color online). Data compared with the sum of the predicted EW and multijet backgrounds for the $\Delta\phi^{\text{jet}}_{\not\!\!E_T}$ variable in the CDF analysis. The band represents the total systematic uncertainty on the background. The measured signal is included here in the EW contribution. From Aaltonen *et al.*, 2009a.

backgrounds to the diboson signal are $W(\ell\nu)$ + jets, $Z(\nu\nu)$ + jets, and QCD multijet production. Other less significant backgrounds include $Z(\ell\ell)$ + jets, $t\bar{t}$, and single t-quark production. The majority of events are collected using an inclusive $\not\!\!E_T$ trigger which requires $\not\!\!E_T > 45$ GeV. In the offline selection, events are required to have $\not\!\!E_T > 60$ GeV and exactly two reconstructed jets with $E_T > 25$ GeV and $|\eta| < 2.0$.

The shape and normalization of the multijet background are determined from the data. A tracking-based missing momentum vector $\vec{\not\!p}_T$, analogous to the calorimeter-based $\vec{\not\!\!E}_T$, is constructed from the vector sum of the transverse momenta of particles measured in the tracking system, and is largely uncorrelated to $\vec{\not\!\!E}_T$ for events where jets are misreconstructed. In the absence of $\not\!\!E_T$ arising from mismeasurement in the calorimeter, the $\vec{\not\!\!E}_T$ and $\vec{\not\!p}_T$ will be aligned in most events. At large values of $\Delta\phi(\vec{\not\!\!E}_T, \vec{\not\!p}_T)$, multijets are expected to be the dominant component of the data. The dijet mass shape and normalization for the multijet background that remains after the event selection are determined by selecting events with $\Delta\phi(\vec{\not\!\!E}_T, \vec{\not\!p}_T) > 1.0$ and subtracting out the nonmultijet backgrounds. The normalization is scaled up to account for the multijet background contamination in the region $\Delta\phi(\vec{\not\!\!E}_T, \vec{\not\!p}_T) < 1.0$. The shape of the multijet background is fit to an exponential in M_{jj} to derive a dijet mass template for use in the M_{jj} unbinned extended likelihood fit performed to extract the diboson signal. The distribution of $\Delta\phi^{\text{jet}}_{\not\!\!E_T}$ observed in the data is in good agreement with the expectations as shown in Fig. 40, giving confidence in the validity of the multijet background model.

Three M_{jj} template distributions are used in the fit: the first is V + jets and t-quark production and is taken from Monte Carlo simulation; the second is the multijet template, where the slope and normalization are Gaussian constrained to their previously measured values; and the third template describes the signal. The signal shape is comprised of the WW, WZ, and ZZ distributions obtained from a Gaussian + polynomial fit to the signal Monte Carlo simulation where the mean and the width of the Gaussian distribution are linearly dependent on the JES. The uncertainty associated with the JES is the dominant source of systematic uncertainty of the diboson cross-section measurement.

Figure 41 shows the fit result and a comparison between the expected signal and data after background subtraction. The signal significance is reported to be greater than 5.3σ from the background-only hypothesis. This represents the first observation in hadronic collisions of the production of weak gauge boson pairs where one boson decays to a dijet final state. The measured cross section is

$$\sigma(WW + WZ + ZZ + X) = 18.0 \pm 2.8(\text{stat}) \pm 2.4(\text{syst}) \pm 1.1(\text{lumi})\ \text{pb},$$

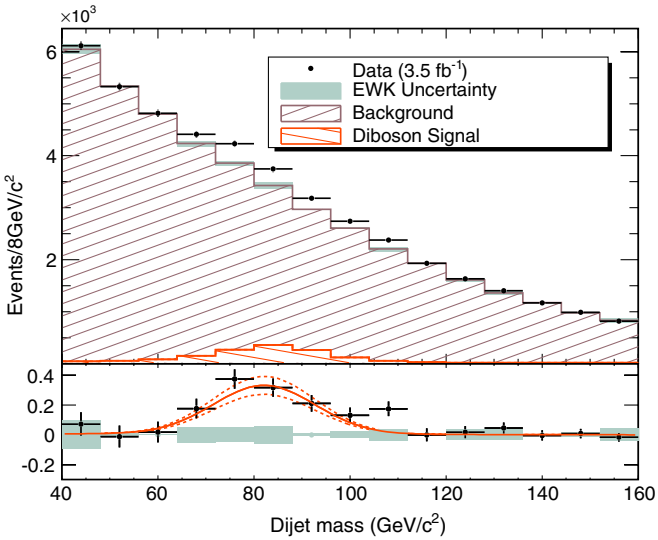

FIG. 41 (color online). Top: Comparison between data and fitted background only. The measured signal is shown unstacked. The band represents the systematic uncertainty due to the shape of EW background as described by Aaltonen *et al.* (2009a). Bottom: Comparison of the diboson signal (solid line) with the background-subtracted data (points). The dashed lines represent the $\pm 1\sigma$ statistical variations on the extracted signal. The band represents the systematic uncertainty due the EW shape.

TABLE XIX. A summary of EW gauge boson cross-section measurements and theory expectations during Run II and the Fermilab Tevatron.

Process	Channel	$\int \mathcal{L}dt$ (fb^{-1})	Cross section (pb) Theory	Cross section (pb) Measured	Expt. Ref.
$p\bar{p} \to W\gamma + X \to \ell\nu\gamma + X$					
$(E_T^\gamma > 7$ GeV, $\Delta R_{\ell,\gamma} > 0.7)$	$\ell\nu\gamma$	~0.2	19.3 ± 1.4[a]	18.1 ± 3.1(stat + syst)	CDF[b]
$(E_T^\gamma > 8$ GeV, $\Delta R_{\ell,\gamma} > 0.7)$	$\ell\nu\gamma$	~0.2	16.0 ± 0.4[a]	14.8 ± 1.9(stat + syst) ± 1.0(lumi)	D0[c]
$p\bar{p} \to Z\gamma + X \to \ell\ell\gamma + X$					
$(E_T^\gamma > 7$ GeV, $\Delta R_{\ell,\gamma} > 0.7$, $M_{\ell\ell} > 40$ GeV$/c^2)$	$\ell\ell\gamma$	~0.2	4.5 ± 0.3[d]	4.6 ± 0.6(stat + syst)	CDF[b]
$(E_T^\gamma > 7$ GeV, $\Delta R_{\ell,\gamma} > 0.7$, $M_{\ell\ell} > 30$ GeV$/c^2)$	$\ell\ell\gamma$	~1.1	4.7 ± 0.2[d]	5.0 ± 0.3(stat + syst) ± 0.3(lumi)	D0[e]
$p\bar{p} \to Z\gamma + X \to \nu\nu\gamma + X$ $(E_T^\gamma > 90$ GeV)	$\nu\nu\gamma$	3.6	0.039 ± 0.04[d]	0.032 ± 0.09(stat + syst) ± 0.02(lumi)	D0[f]
$p\bar{p} \to WW + X$	$\ell\nu\ell\nu$	3.6	11.7 ± 0.7[g]	$12.9 \pm 0.9(\text{stat})^{+1.6}_{-1.4}$(syst)	CDF[h]
	$\ell\nu\ell\nu$	~1.1		11.5 ± 2.1(stat + syst) ± 0.7(lumi)	D0[i]
$p\bar{p} \to WZ + X$	$\ell\ell\ell\nu$	1.1	3.7 ± 0.3[g]	$5.0^{+1.8}_{-1.4}$(stat) ± 0.4(syst)	CDF[j]
	$\ell\ell\ell\nu$	1.0		$2.7^{+1.7}_{-1.3}$(stat + syst)	D0[k]
$p\bar{p} \to ZZ + X$	$\ell\ell\ell\ell$, $\ell\ell\nu\nu$	1.9	1.4 ± 0.1[g]	$1.4^{+0.7}_{-0.6}$(stat + syst)	CDF[l]
	$\ell\ell\ell\ell$, $\ell\ell\nu\nu$	1.7		1.6 ± 0.6(stat) ± 0.2(syst)	D0[m]
$p\bar{p} \to WV + X(V \to W, Z)$	$\ell\nu qq$	2.7	16.1 ± 0.9[g]	16.0 ± 3.3(stat + syst)	CDF[n]
	$\ell\nu qq$	1.1		20.2 ± 4.5(stat + syst)	D0[o]
$p\bar{p} \to VV + X(V \to W, Z)$	$\ell\nu qq$, $\nu\nu qq$	3.5	16.8 ± 0.5[g]	18.0 ± 2.8(stat) ± 2.4(syst) ± 1.1(lumi)	CDF[p]

[a] Baur and Berger, 1993.
[b] Acosta *et al.*, 2005b.
[c] Abazov *et al.*, 2005a.
[d] Baur and Zeppenfeld, 1988.
[e] Abazov *et al.*, 2007a.
[f] Abazov *et al.*, 2009d.
[g] Campbell and Ellis, 1999.
[h] Aaltonen *et al.*, 2010a.
[i] Abazov *et al.*, 2009e.
[j] Abulencia *et al.*, 2007b.
[k] Abazov *et al.*, 2007b.
[l] Aaltonen *et al.*, 2008b.
[m] Abazov *et al.*, 2008d.
[n] Aaltonen *et al.*, 2010b.
[o] Abazov *et al.*, 2009f.
[p] Aaltonen *et al.*, 2009a.

consistent with the SM NLO prediction of 16.8 ± 0.5 pb (Campbell and Ellis, 1999).

9. Cross section and anomalous TGC summary

A summary of the diboson production cross sections at the Tevatron with comparisons to the theory expectations can be found in Table XIX and Fig. 42. A summary of limits on anomalous charged and neutral TGCs at the Tevatron can be found in Tables XX and XXI, respectively.

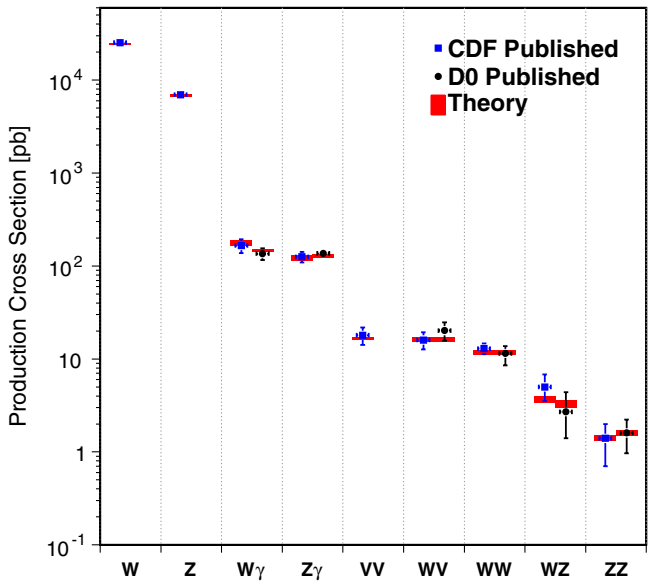

FIG. 42 (color online). A graphical summary of EW gauge boson cross-section measurements and theory expectations during Run II and the Fermilab Tevatron.

The experimental progress on diboson physics during Run II at the Fermilab Tevatron has been truly remarkable. This includes the first observation of WZ production and the first observation at a hadron collider of ZZ production and of weak gauge boson pair production in semileptonic decay. The associated diboson cross-section measurements (many of which are significantly improved from Run I) and detailed studies of their kinematic properties provide stringent tests of standard electroweak theory and constraints on possible new physics coupling to the EW gauge bosons.

IV. TOP QUARK

A. Top-quark mass

As discussed in Sec. V.A, constraints on the Higgs-boson mass from fits to data assuming the SM are limited by the experimental precision of the W boson and top-quark masses. Measurements of the top-quark mass thus have direct implications for the SM, and these measurements are a central component of the programs for both CDF and D0. As evidenced from Fig. 3, constraints on the Higgs mass are limited more by the uncertainty in the W boson mass than by the uncertainty in the top-quark mass, which reflects the tremendous progress that has been made on the top-quark mass measurement in Run II. In fact, the top-quark mass is now the most accurately known quark mass (as a percentage of its value), surpassing even its $SU(2)_L$ partner the b quark, whose mass is known to about 2.6% [$\bar{m}_b(\bar{m}_b) = 4.24 \pm 0.11$ GeV$/c^2$] (El-Khadra and Luke, 2002).

TABLE XX. A summary of anomalous charged TGC limits for different diboson processes and decay channels measured during Run II and the Fermilab Tevatron.

Mode	TGC(s)	$\int \mathcal{L}dt$ (fb^{-1})	Λ (TeV)	95% C.L. limits (model constraints in parentheses) λ_γ	$\Delta\kappa_\gamma$	λ_Z	Δg_1^Z	$\Delta\kappa_Z$	Expt. Ref.
$\ell\nu\gamma$	$WW\gamma$	~0.7	2.0	$-0.12, 0.13$	$-0.51, 0.51$	...	...	...	D0[a]
$\ell\nu\ell\nu$	$WW(\gamma, Z)$	3.6	1.5	$-0.16, 0.16$	$-0.63, 0.72$	λ_γ	$-0.24, 0.34$	$\Delta g_1^Z - \Delta\kappa_\gamma \tan^2\theta_W$	CDF[b]
			2.0	$-0.14, 0.15$	$-0.57, 0.65$	λ_γ	$-0.22, 0.30$	$\Delta g_1^Z - \Delta\kappa_\gamma \tan^2\theta_W$	CDF[b]
		~1.1	2.0	$-0.14, 0.18$	$-0.54, 0.83$	λ_γ	$-0.14, 0.30$	$\Delta g_1^Z - \Delta\kappa_\gamma \tan^2\theta_W$	D0[c]
			2.0	$-0.14, 0.18$	$-0.12, 0.35$	λ_γ	0	$\Delta\kappa_\gamma$	D0[c]
$\ell\ell\ell\nu$	WWZ	~1.0	1.5	...	...	$-0.18, 0.22$	$-0.15, 0.35$	$-0.14, 0.31$ ($\Delta\kappa_Z = \Delta g_1^Z$)	D0[d]
			2.0	...	...	$-0.17, 0.21$	$-0.14, 0.34$	$-0.12, 0.29$ ($\Delta\kappa_Z = \Delta g_1^Z$)	D0[d]
$\ell\nu qq$, $\ell\nu\gamma$	$WW(\gamma, Z)$	0.4	1.5	$-0.18, 0.17$	$-0.46, 0.39$	λ_γ	0	$\Delta\kappa_\gamma$	CDF[e]
		1.1	2.0	$-0.10, 0.11$	$-0.44, 0.55$	λ_γ	$-0.12, 0.20$	$\Delta g_1^Z - \Delta\kappa_\gamma \tan^2\theta_W$	D0[f]
				$-0.11, 0.11$	$-0.16, 0.23$	λ_γ	0	$\Delta\kappa_\gamma$	D0[f]
$\ell\nu\gamma$,$\ell\nu\ell\nu$,$\ell\ell\ell\nu$,$\ell\nu qq$	$WW(\gamma, Z)$	~1.0	2.0	$-0.08, 0.08$	$-0.29, 0.38$	λ_γ	$-0.07, 0.16$	$\Delta g_1^Z - \Delta\kappa_\gamma \tan^2\theta_W$	D0[g]
				$-0.08, 0.08$	$-0.11, 0.18$	λ_γ	0	$\Delta\kappa_\gamma$	D0[g]

[a] Abazov *et al.*, 2008b.
[b] Aaltonen *et al.*, 2010a.
[c] Abazov *et al.*, 2009e.
[d] Abazov *et al.*, 2007b.
[e] Aaltonen *et al.*, 2007a.
[f] Abazov *et al.*, 2009g.
[g] Abazov *et al.*, 2009b.

TABLE XXI. A summary of anomalous neutral TGC limits for different diboson processes and decay channels measured during Run II and the Fermilab Tevatron.

Mode	TGC(s)	$\int \mathcal{L}dt$ (fb^{-1})	Λ (TeV)	95% C.L. limits				Expt. Ref.
$\ell\ell\ell\ell$	ZZZ, $ZZ\gamma$	1.0	1.2	$-0.28 < f_{40}^\gamma < 0.28$	$-0.26 < f_{40}^\gamma < 0.26$	$-0.31 < f_{50}^Z < 0.29$	$-0.30 < f_{50}^Z < 0.28$	D0[a]
$\ell\ell\gamma$, $\nu\nu\gamma$	$Z\gamma\gamma$, $ZZ\gamma$	1.0, 3.6	1.5	$\lvert h_{30}^\gamma\rvert < 0.033$	$\lvert h_{40}^\gamma\rvert < 0.0017$	$\lvert h_{30}^Z\rvert < 0.033$	$\lvert h_{40}^Z\rvert < 0.0017$	D0[b]

[a] Abazov *et al.*, 2008c.
[b] Abazov *et al.*, 2009d.

The top-quark mass measured at the Tevatron corresponds closely to the pole mass. The pole mass is the mass the quark would have in the absence of confinement. Although the top quark decays on a time scale less than the time scale associated with confinement ($\Lambda_{\text{QCD}}^{-1}$), the top-quark pole mass is nevertheless affected by confinement (Smith and Willenbrock, 1997). The ambiguity in the top-quark pole mass is of order $\Lambda_{\text{QCD}} \approx 200$ MeV, which is considerably less than the present uncertainty. A more precise definition of mass will be needed if one attempts to measure the mass to an accuracy much less than 1 GeV$/c^2$.

Both CDF and D0 made measurements of the top-quark mass in a variety of final states and using different methods. The general procedure is to select events consistent with $t\bar{t}$ production in either the dilepton or lepton plus jets final state. In the SM, top quarks decay via $t \to Wb$ with a branching fraction of essentially 100%. The dilepton final state is that in which both W bosons from the $t\bar{t}$ pair decay to leptons, and the lepton + jets final state is that in which one W decays to leptons and the other to quarks. Measurements of the mass have also been made in the all jets final state in which both Ws decay to quarks, although this offers less precision because of significantly higher backgrounds.

An initial selection of candidate dilepton events is made, typically requiring two high p_T charged leptons, significant $\not\!\!E_T$ attributed to neutrinos, and at least two jets. Typical thresholds for the lepton and jet transverse momenta range between 15 and 20 GeV$/c$. The $\not\!\!E_T$ is attributed to the two neutrinos from $t\bar{t}$ decay, and the thresholds are higher, ranging between 35 and 50 GeV depending on topology. The initial selection of lepton + jets candidate events requires a single charged lepton, $\not\!\!E_T$, and at least three (and often four) jets. The lepton and jet thresholds are similar to the dilepton final state, but the $\not\!\!E_T$ threshold is typically relaxed giving requirements ranging from $\not\!\!E_T > 15$ to $\not\!\!E_T > 20$ GeV. Because the lepton + jets events have significant background from W + jet events, an additional requirement that one or more of the jets is consistent with B hadron production (b tagged) is often made. The typical tagging efficiency is 50%/jet with light quark misidentification rates of roughly 1%. The probability to misidentify a charm quark induced jet as being consistent with B hadron production is roughly 15%. Actual values vary somewhat depending on the b-tagging algorithm used. The values also depend on the signal-to-background requirements of the specific analysis which allow more or less restrictive tagging requirements.

TABLE XXII. Signal and background yields for preselected $t\bar{t}$ samples from a subset of the published results. The purity varies considerably depending on the final state and whether or not b-tagged jets are required.

Channel	$\int \mathcal{L}dt$ Channel	Expected signal yield	Estimated total yield	Observed yield	b tag required?	Expt. Ref.
$\ell\ell$	2	43.8 ± 4.4	215.8 ± 21.9	246	$\equiv 0$	CDF[a]
		78.0 ± 6.2	97.5 ± 7.2	98	≥ 1	
$\ell\ell$, $e\mu$	1	36.7 ± 2.4	44.5 ± 2.7	39	no	D0[b]
ee		11.5 ± 1.4	14.8 ± 1.5	17		
$\mu\mu$		8.3 ± 0.5	13.7 ± 0.7	13		
e + track		9.4 ± 0.1	10.3 ± 0.2	8	≥ 1	
μ + track		4.6 ± 0.1	5.5 ± 0.1	6		
ℓ + jets	1.9	183 ± 25	247 ± 29	284	$= 1$	CDF[c]
		69 ± 11	75 ± 11	87	≥ 2	
ℓ + jets	1	162 ± 11	57.2 ± 4.2(est)	200	≥ 1	D0[d]

[a]Aaltonen *et al.*, 2009b.
[b]Abazov *et al.*, 2009i.
[c]Aaltonen *et al.*, 2009c.
[d]Abazov *et al.*, 2008f.

These loose initial selections have minimal top-quark mass bias and form the basis for further analysis.

Typical signal and background estimates are given in Table XXII for various channels. In the selections, tradeoffs are made between signal acceptance and purity. In particular, the requirement that an event have one or more jets consistent with being initiated by b quarks considerably improves the signal purity.

After the initial selections, various methods are used to determine the top mass. Among these are (1) template methods in which data are fit to the predicted signal plus background distribution for a variable that is sensitive to the top mass, (2) ME methods similar to those discussed in Sec. III.E.4 in which $t\bar{t}$ event kinematics determined by matrix element calculations are convoluted with detector resolution functions to predict measured kinematic distributions as a function of the top mass used in the matrix element calculations, and (3) other weighting methods in which missing information is supplied by trying possible reconstructed jet and true $t\bar{t}$ decay parton assignments and computing a probability for the particular assignment as a function of top mass. The ME and various weighting methods compute event-by-event likelihoods as a function of top mass, and then compute the total likelihood for a data set as the products of the event likelihoods. Combinations of these methods are also used.

For lepton + jet events, the momenta of the four jets and the lepton are fully measured, and the neutrino momentum in the plane transverse to the beam is inferred from the event $\not\!\!E_T$. This gives 17 measured values. Two constraints are available. The first is that the invariant mass of one pair of reconstructed jets should be consistent with that of the W boson, and the second is that the reconstructed mass of the two top quarks should be consistent with each other. This information allows a 1 degree-of-freedom fit to be performed in which the top mass is a free parameter. The resulting event top mass values are not simply averaged to determine the mass, but provide an input variable to the various methods described above. The fit χ^2 can also be used to determine (or weight) the most likely parton-jet assignment in an event. Complications to this fit arise from the presence of intrinsic transverse momentum of the $t\bar{t}$ system $p_T^{t\bar{t}}$ and from final-state gluon radiation giving rise to additional jets. The $p_T^{t\bar{t}}$ can be incorporated by adding an additional variable for the unknown transverse momentum $\vec{X}$ to the fit and constraining it using *a priori* estimates of the spectrum. The impact of final-state radiation can be controlled by requiring exactly four reconstructed (good) jets in the event.

For dilepton events, the number of measurements minus the number of constraints does not give enough information to fully determine the final-state kinematics, and one assumption must be made. A variety of methods are used including ME weighting and neutrino weighting. The ME weighting method (Kondo, 1988, 1991; Dalitz and Goldstein, 1992) is related to the general ME method described below (and also used for ℓ + jets analyses). The neutrino weighting method (Abbott *et al.*, 1998, 1999) is unique to dilepton events. In this method, an event weight is defined as a function of hypothesized top-quark mass M_t using a comparison of the measured $\vec{\not\!\!E}_T$ to $\vec{\not\!\!E}_{Ti}$ values predicted for a set of possible neutrino pseudorapidity values $\eta_i^{(1)}$, $\eta_i^{(2)}$. Large weights correspond to situations in which the measured and predicted $\vec{\not\!\!E}_T$ are similar and thus give a probability for different η values for the neutrinos in each event.

The use of the ME approach has become widespread, especially for ℓ + jets final states. It is used either as the final analysis variable used to determine the measured mass or to provide information used in joint likelihoods for determining the top mass. In this approach, the probability that the jet momenta, lepton momentum, and missing transverse energy observed in a given event, assuming it arises from $t\bar{t}$ production and decay, is computed by (Abazov *et al.* (2008f)

$$P_{t\bar{t}} = \frac{1}{N} \int \sum d\sigma(y; M_t) dq1 dq2 f(q_1) f(q_2) W(y, x)$$

in which $d\sigma$ is the differential cross section for production of the final-state partons in (momentum) configuration y for a given M_t, $f(q_1)$ and $f(q_2)$ are the parton density functions for the proton and antiproton, $W(y, x)$ is the transfer function for

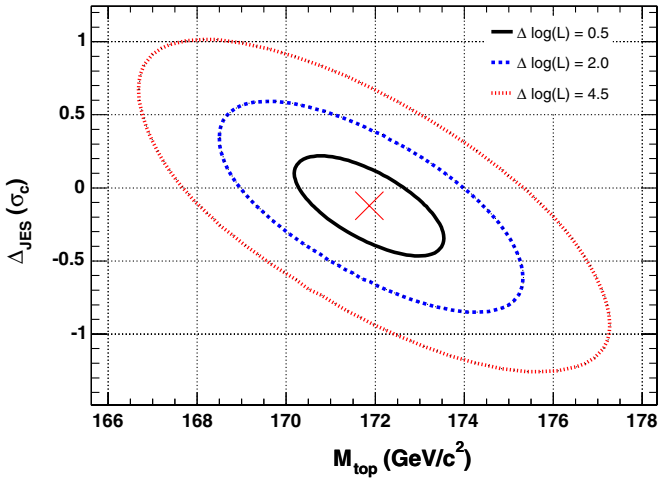

FIG. 43 (color online). Contours of constant-log(L) in the $\Delta_{\rm jes} \equiv k_{\rm jes} - 1$ vs M_t plane. A perfect *a priori* jet energy calibration used as input to this analysis results in $k_{\rm jes} = 1$ corresponding to $\Delta_{\rm jes} = 0$. From Aaltonen *et al.*, 2009d.

computing the probability that a partonic final state y gives the observed reconstructed final state x, and $1/N$ is a normalization factor equal to the expected observed cross section for a given M_t. For each event, this probability and the corresponding probability computed assuming the event is a background event $P_{\rm bkg}(x)$ are combined to give an event probability as a function of top mass

$$P(x; M_t) = A(x)[fP_{t\bar{t}}(x; M_t) + (1 - f)P_{\rm bkg}(x)]$$

in which $A(x)$ is a normalization factor incorporating acceptance and efficiency effects and f is the fraction of $t\bar{t}$ events in the total sample. The overall normalization of P is forced to unity so that it can be used as a probability density. The event probability is then used either as input to additional likelihoods or the joint likelihood for the entire sample is formed as the product of the event probabilities and minimized as a function of M_t.

The methods used in early Run II top mass measurements had systematic uncertainty from the energy calibration of reconstructed jets which, if unmodified, would have quickly surpassed the statistical uncertainty. A method was developed to incorporate an *in situ* calibration scale factor as a second fit parameter when determining the top mass. As an example, the ME method event probability definition was modified to the form now in general use. This form is

$$P(x; M_t, k_{\rm jes}) = A(x)[fP_{t\bar{t}}(x; M_t, k_{\rm jes}) + (1-f)P_{\rm bkg}(x; k_{\rm jes})]$$

in which $k_{\rm jes}$ is a scale factor applied to all jet energies. In this form the transfer functions also become dependent on the calibration $W(y, x, k_{\rm jes})$. The negative log likelihood minimized to determine the top mass thus becomes a function of two variables, $m_{\rm top}$ and $k_{\rm jets}$, both of which are varied during the minimization. As an example, Fig. 43 shows the 2D contour in the $\Delta_{\rm jes} \equiv k_{\rm jes} - 1$ versus $m_{\rm top}$ plane from the M_t measurement using the $\ell\ell$ and ℓ + jets final states simultaneously (Aaltonen *et al.*, 2009d).

TABLE XXIII. Summary of published Run II top-quark mass measurements. Additional preliminary results using up to $\int \mathcal{L}dt = 4$ fb^{-1} have been reported by both CDF and D0. The Particle Data Group average includes only some of these results, and the Tevatron average is based on a subset of the results in this table and additional preliminary results.

Channel	$\int \mathcal{L}dt$ (fb^{-1})	Analysis method	M_t (GeV/c^2)	Main systematic source	Uncertainty Value (GeV/c^2)	Expt. Ref.
$\ell\ell$ + (ℓ + jets)	1.9		171.9 ± 1.7(stat + JES) ± 1.1(syst)			CDF[a]
$\ell\ell$	2.9	ϕ WT	$165.5^{+3.4}_{-3.3}$(stat) ± 3.1(syst)	Jet calibration	2.2	CDF[b]
	2	Matrix	171.2 ± 2.7(stat) ± 2.9(syst)	Jet calibration	2.5	CDF[c]
	1.2	Template + M_t	$170.7^{4.2}_{-3.9}$(stat) ± 2.6(syst) ± 2.4(theo)	Jet calibration	1.8?	CDF[d]
	1	Matrix	164.5 ± 3.9(stat) ± 3.9(syst)	Jet calibration	3.5	CDF[e]
	1	Matrix + νWT	174.7 ± 4.4(stat) ± 2.0(syst)	Jet calibration	1.2	D0[f]
ℓ + jets	1.9	Matrix	172.7 ± 1.8(stat) ± 1.2(syst)	Generator, jet calib.	0.6, 0.5	CDF[g]
	1	Matrix	171.5 ± 1.8(stat + JES) ± 1.1(syst)	b/u, d,s, frag.	0.83	D0[h]
	0.7	Decay length	$180.7^{+15.5}_{-13.4}$(stat) ± 8.6(syst)	Bkg. shape	6.8	CDF[i]
	0.4	Ideogram	173.7 ± 4.4(stat + JES) ± 2.1(syst)	b/u, d, s calib.	1.7	D0[j]
	0.3	Template + DLL	$173.5^{+3.7}_{-3.6}$(stat + JES) ± 1.3(syst)	Signal model	1.1	CDF[k]
All jets	1	Line shape	174.0 ± 2.2(stat) ± 4.8(syst)	Jet calibration	4.5	CDF[l]
	1.0	Matrix	171.1 ± 3.7(stat + JES) ± 2.1(syst)	Parton shower, jet calib.	0.6, 0.5	CDF[m]
$\not\!\!E_T$ + jets	0.3	Spectra	$172.3^{10.8}_{-9.6}$(stat) ± 10.8(syst)	Jet calibration	9.6	CDF[n]
Tevatron (incl. prel.)			173.1 ± 0.6(stat) ± 1.1(syst)			CDF + D0[o]
Particle Data Group 2008			171.2 ± 2.1			PDG[p]

[a] Aaltonen *et al.*, 2009d.
[b] Aaltonen *et al.*, 2009e.
[c] Aaltonen *et al.*, 2009b.
[d] Aaltonen *et al.*, 2008c.
[e] Abulencia *et al.*, 2007c.
[f] Abazov *et al.*, 2009i.
[g] Aaltonen *et al.*, 2009c.
[h] Abazov *et al.*, 2008f.
[i] Abulencia *et al.*, 2007d.
[j] Abazov *et al.*, 2007c.
[k] Abulencia *et al.*, 2006a.
[l] Aaltonen *et al.*, 2007b.
[m] Aaltonen *et al.*, 2009f.
[n] Aaltonen *et al.*, 2007c.
[o] Tevatron Electroweak Working Group, 2009c.
[p] Amsler *et al.*, 2008.

Systematic uncertainties in top mass measurements arise from both experimental sources and theory. Although the contribution from calibration uncertainties has been significantly reduced as described in the previous paragraph, the dominant contributions to the systematic uncertainty from experimental sources are the absolute reconstructed jet energy calibration and the relative calibrations of jets initiated by b quarks and those from light quarks (u, d, s). Of these, the uncertainty from the jet calibrations dominates the experimental uncertainties. Uncertainties arising from theory include the production model as assessed by comparing event generators and fragmentation. The production model uncertainty becomes the dominant theory uncertainty when various measurements are combined.

Table XXIII and Fig. 44 give a summary of the published top mass results and a comparison with the 2008 Particle Data Group (PDG) (Amsler *et al.*, 2008) average. When multiple results from one experiment using the same method and final state were available, only the highest integrated luminosity measurement was reported. The result shown in Table XXIII with highest integrated luminosity used a $\int \mathcal{L}dt = 2.9$ fb^{-1} data sample. The Tevatron experiments have now reported *preliminary* results using up to 4 fb^{-1}, and these results have been included in a world average combination by the Tevatron Electroweak Working Group, with the most recent such combination (Tevatron Electroweak Working Group, 2009c) giving

$$M_t = 173.1 \pm 0.6(\text{stat}) \pm 1.1(\text{syst}) \text{ GeV}/c^2.$$

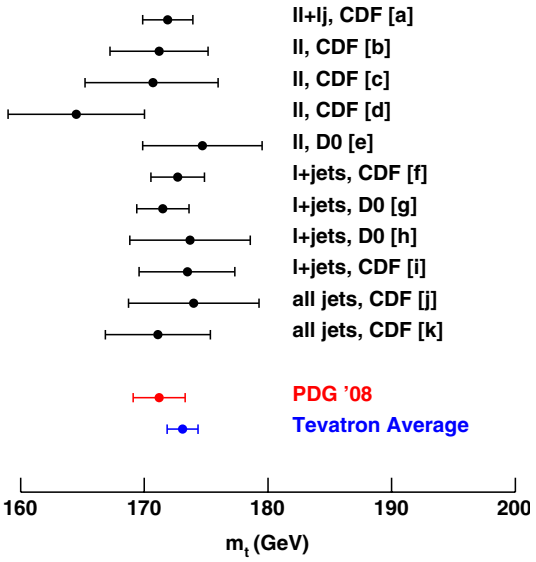

FIG. 44 (color online). Published top mass measurements. For a given experiment and final state, the results from different methods have a significant correlation. [a]Aaltonen *et al.* (2009d); [b] Aaltonen *et al.* (2009b); [c] Aaltonen *et al.* (2008c); [d] Abulencia *et al.* (2007c); [e] Abazov *et al.* (2009i); [f] Aaltonen *et al.* (2009c); [g] Abazov *et al.* (2008f); [h] Abazov *et al.* (2007c); [i] Abulencia *et al.* (2006a); [j] Aaltonen *et al.* (2007b); [k] Aaltonen *et al.* (2009f). Also shown are the most recent Tevatron combination (Tevatron Electroweak Working Group, 2009c) and the PDG world average (Amsler *et al.* (2008). Both of these include a subset of the measurements listed.

For this combination, which includes preliminary results, the systematic uncertainty is significantly larger than the statistical uncertainty. The dominant components of the systematic uncertainty arise from uncertainty on the *in situ* jet energy calibration, uncertainty related to the $t\bar{t}$ production and decay model, and uncertainty arising for color recombination. These contribute 0.48, 0.49, and 0.41 GeV$/c^2$ to the uncertainty, respectively.

An alternative method of measuring the top-quark mass makes use of the dependence of the production cross section on the mass. The top-quark $\overline{\text{MS}}$ mass may be extracted directly from such a method (Langenfeld, Moch, and Uwer, 2009).

By the end of the Tevatron running, the experiments expect to increase the data set by at least a factor of 4 compared to the published results and at least a factor of 2 for the data sets used in the combination. Thus, the statistical precision can be improved, but the systematic uncertainties will also need to be improved if the full statistical power of the final data set is to be realized.

B. W helicity from top-quark decays

In the SM, top quarks decay with a $V-A$ interaction through the process $t \to W^+ b$ with $B(t \to W + b) \approx 1$. The SM predicts a fraction $f_0 = 0.697 \pm 0.012$ of top-quark decays gives a longitudinally polarized W and a fraction $f_+ = 3.6 \times 10^{-4}$ gives a right-handed W. This leaves $f_- = 1 - f_0 - f_+$ giving left-handed Ws. Compared to the decay of lower mass quarks, the fraction of decays with longitudinally polarized W is significantly increased because of the large Yukawa coupling between the top quark and Higgs boson. Changes to the Lorentz $(V-A)$ structure of the decay will result in changed values for the polarization fractions. Indirect results from $b \to s\gamma$ measurements (Cho and Misiak, 1994; Fujikawa and Yamada, 1994) constrain f_+ to less than a few percent.

The angular distribution of the electron-type ($I_3 = -1/2$) W decay product in $t \to Wb$ is given by

$$\omega(c) = \tfrac{3}{8}[2(1-c^2)f_0 + (1-c)^2 f_- + (1+c)^2 f_+]$$

in which $c \equiv \cos\theta^*$ is the cosine of the decay angle in the W rest frame measured with respect to the top-quark direction. Both CDF (Aaltonen *et al.*, 2009i) and D0 (Abazov *et al.*, 2008g) measured the helicity fractions in top-quark decay. The CDF analysis uses $\int \mathcal{L}dt = 1.9$ fb^{-1}, and the D0 result is based on $\int \mathcal{L}dt = 1.0$ fb^{-1}.

Both experiments select events in the ℓ + jets topology, and D0 also uses the $\ell\ell + X$ topology. The initial selections are similar to those described earlier in Sec. IV.A. CDF uses a second selection with somewhat different requirements to perform an independent analysis. The CDF results are from the combination of the two methods.

All results rely on reconstructing the $\cos\theta^*$ distribution and comparing that to a set of predicted distributions each of which is generated with a different pair of f_0 and f_+ values. Several ambiguities arise in reconstructing $\cos\theta^*$. These include the assignment of the reconstructed jets to the quarks from W decay (for the hadronic side of ℓ + jets events) and the impact from the unmeasured η value for the neutrino

TABLE XXIV. W boson helicity fractions in $t\bar{t}$ decay determined from fits to data. The first two lines are the results from simultaneous fits for f_0 and f_+. The third line is the result from the fit for f_0 with $f_+ = 0$, and the fourth is from the fit for f_+ with f_0 set to the SM value. In all cases, the statistical uncertainty is shown first and the second uncertainty is the systematic uncertainty.

	CDF	D0
f_0	$0.66 \pm 0.16 \pm 0.05$	$0.425 \pm 0.166 \pm 0.102$
f_+	$-0.03 \pm 0.06 \pm 0.03$	$0.119 \pm 0.090 \pm 0.053$
f_0, $f_+ = 0$	$0.62 \pm 0.10 \pm 0.05$	$0.619 \pm 0.090 \pm 0.052$
f_+, $f_0 = 0.70$	$-0.03 \pm 0.04 \pm 0.03$	$-0.002 \pm 0.047 \pm 0.047$

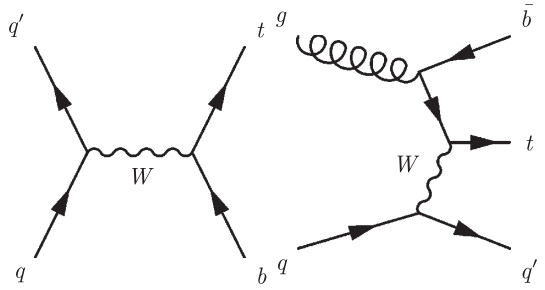

FIG. 45. The s-channel (left) and t-channel (right) diagrams for single-top production.

arising in leptonic W decay. These issues are handled differently in the three (two CDF, one D0) analyses. The CDF analyses use only the leptonic W decay. The D0 analysis also uses the jets from the hadronic W, but only $|\cos\theta^*|$ is reconstructed for these, not $\cos\theta^*$. Although this loses the ability to distinguish f_+ from f_- for the hadronic decay, f_0 is better constrained.

The results are extracted using likelihood fits to test $\cos\theta^*$ distributions. For one of the CDF methods and the D0 analysis, predicted reconstructed $\cos\theta^*$ distributions including signal and background contributions are generated using simulated events. The distributions are generated for a range of f_0 and f_+ values, and best values are extracted using likelihood comparisons to the data. For the second CDF method, the result is compared to a distribution generated by convoluting the true $\cos\theta^*$ distribution divided into six bins with a migration function which gives the probability that an event generated in a given true bin ends up as a given reconstructed bin. This function includes the effects of resolution and acceptance. Effects of helicity on the acceptance are considered in all cases.

The experimental results are summarized in Table XXIV. The results are consistent with each other and with the SM prediction. They are generally limited by the statistical precision of the data set and are expected to improve by a factor between $\times 2$ and $\times 10$ by the end of Run II, depending on the analysis and machine performance achieved. Even if there is no improvement in the systematic uncertainty, the final results will still be statistics limited, but the statistical and systematic uncertainties will be similar. The dominant systematic uncertainty in the D0 result comes from the $t\bar{t}$ production and decay model which was tested by comparing results from events generated using the PYTHIA generator (Sjostrand *et al.*, 2001) and with the default events generated using ALPGEN (Mangano *et al.*, 2003). The CDF result does not have a single dominant source of systematic uncertainty. Although the contributions vary somewhat, the uncertainties arising from jet calibration, the background prediction, and modeling of final-state radiation are roughly equivalent to each and provide most of the systematic uncertainty.

C. Single-top production and V_{tb}

The top quark was first observed in reactions mediated by the strong interaction process $p\bar{p} \to t\bar{t}$ (Abachi *et al.* (1995) and Abe *et al.* (1995), and nearly all measurements of the top-quark properties have been made using such events. However, top quarks can also be produced singly via the s-channel (Cortese and Petronzio, 1991; Stelzer and Willenbrock, 1995; Heinson *et al.*, 1997) and t-channel (Willenbrock and Dicus, 1986; Yuan, 1990; Ellis and Parke, 1992; Heinson *et al.*, 1997) electroweak diagrams shown in Fig. 45. These production modes involve the Wtb coupling and therefore cross-section measurements provide previously unmeasured information on the electroweak sector, particularly the CKM matrix element V_{tb}. In addition to providing information about V_{tb}, detecting these events demonstrates progress toward Higgs sensitivity for the WH associated production mode with the subsequent decay $H \to bb$.

The NLO cross sections for these processes are $\sigma_s = 1.12 \pm 0.05$ pb and $\sigma_t = 2.34 \pm 0.13$ pb (Smith and Willenbrock, 1996; Stelzer, Sullivan, and Willenbrock, 1997; Harris *et al.*, 2002; Campbell, Ellis, and Tramontano, 2004; Sullivan, 2004; Cao *et al.*, 2005; Cao, Schwienhorst, and Yuan, 2005; Frixione *et al.*, 2006; Kidonakis, 2006; Campbell *et al.*, 2009) for the s-channel and t-channel reactions, respectively, assuming $|V_{tb}| = 1$ and a top-quark mass of $M_t = 175\ \mathrm{GeV}/c^2$. While the total single-top cross section is slightly more than 40% of the $t\bar{t}$ cross section, the reduced parton multiplicity in the single-top events implies a signal-to-noise ratio which is roughly 25 times lower than in $t\bar{t}$ making these events much more difficult to identify. In the SM with three generations, existing measurements of $|V_{ub}|$ and $|V_{cb}|$ tightly constrain $|V_{tb}|$ to almost exactly unity (Amsler *et al.*, 2008). If there are more than three generations, however, $|V_{tb}|$ is almost entirely unconstrained.

Both D0 and CDF have long histories of searching for single-top production. The most recent results from both D0 (Abazov *et al.*, 2007d, 2008h) and CDF (Aaltonen *et al.*, 2008d) give clear evidence for single-top production and include results for the cross section and the CKM element $|V_{tb}|$. The D0 analysis uses a data sample corresponding to $\int \mathcal{L}dt = 2.3\ \mathrm{fb}^{-1}$. The CDF analysis uses up to $\int \mathcal{L}dt = 3.2\ \mathrm{fb}^{-1}$.

Candidate single top events are selected in the lepton + jets channel in which the W decays via either $W \to e\nu$ or $W \to \mu\nu$. The event topology is thus one high-p_T charged lepton, $\not{E}_T$ corresponding to the neutrino, and two or more jets. Events are required to have fired single electron, single muon, electron + jet, or muon + jet triggers. Both experiments use events with two or three reconstructed jets, and D0 also makes use of 4-jet events. Table XXV shows the yields

TABLE XXV. The integrated luminosity, predicted signal, backgrounds, and event yields in the W + jets (b tag) samples used in the CDF and D0 single-top analyses.

	D0			CDF	
$\int \mathcal{L}dt$	2.3 fb^{-1}			3.2 fb^{-1}	2.1 fb^{-1}
process	= 2 jets	= 3 jets	$\geq$ 4 jets	ℓ + jets	$\not\!\!E_T$ + jets
$tb + tqb$ signal	139 ± 18	63 ± 10	21 ± 5		
tb signal				77.3 ± 11.2	29.6 ± 3.7
tqb signal				113.8 ± 16.9	34.5 ± 6.1
W + jets	1, 829 ± 161	637 ± 61	180 ± 18	1551.0 ± 472.3	304.4 ± 115.5
Z + jets	229 ± 38	85 ± 17	26 ± 7	52.1 ± 8.0	128.6 ± 53.7
Diboson	in Z + jets	in Z + jets	in Z + jets	118.4 ± 12.2	42.1 ± 6.7
$t\bar{t}$	222 ± 35	436 ± 66	484 ± 71	686.1 ± 99.4	184.5 ± 30.2
Multijet	196 ± 50	73 ± 17	30 ± 6	777.9 ± 103.7	679.4 ± 27.9
Total predicted	2615 ± 192	1, 294 ± 107	742 ± 80	3376.5 ± 504.9	1404 ± 172
Yield	2579	1216	724	3315	1411

for the D0 and CDF initial selections in which events are required to have at least one jet having a b tag.

The final results for both experiments are based on combining results from MV techniques which exploit correlations among variables and event weighting methods based on calculated matrix elements for signal and background events.

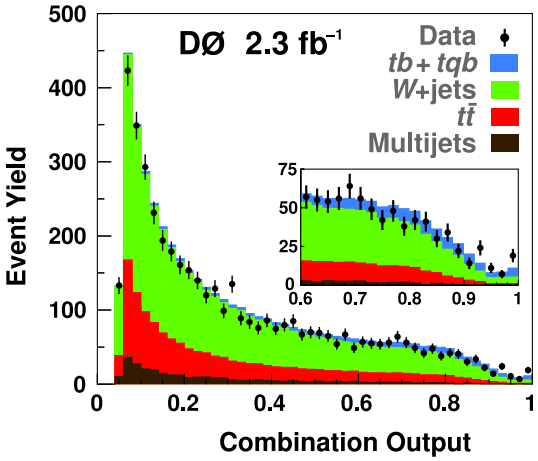

FIG. 46 (color online). The combined discriminant for the D0 analysis.

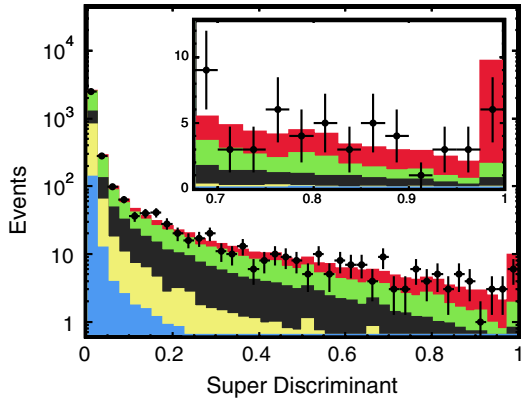

FIG. 47 (color online). The combined discriminant for the CDF analysis.

The methods are applied to events selected by the initial offline requirements. D0 uses three methods: (1) a ME method, (2) a Bayesian neural network (BNN) method, and (3) a boosted decision tree (BDT) method, and the final result comes from the combination of the individual results including correlations. CDF uses five methods: (1) a ME method, (2) a joint likelihood (LF) method, (3) a neural network (NN) method, (4) a BDT method, and (5) projected likelihood functions (LFS), and the final result is the combination of these including correlations among them.

Final results are determined using likelihood fits. Likelihoods are created from the multivariate outputs for each lepton flavor, jet multiplicity, and b-tag multiplicity for a given multivariate method. The joint likelihood formed by the product of the individual likelihoods for a given MV method is then maximized as a function of the signal cross sections with systematic correlations between lepton species, jet multiplicity, and b-tag multiplicity taken into account. The BLUE method (Lyons, Gibaut, and Clifford, 1988) is used by D0 to combine the results from each MV method into a single result. The CDF results are combined using a super discriminant (Aaltonen *et al.*, 2008d), in this case an additional neural

TABLE XXVI. Single-top cross-section measurements from the Tevatron (in pb). The D0 result used $M_t = 170$ GeV/c^2 in simulations and calculation. The CDF result used $M_t = 175$ GeV/c^2. The predicted cross section changes by 0.1 pb for a 5 GeV/c^2 change in M_t in this region.

	$\sigma_{st} = \sigma_s + \sigma_t$	
	D0	CDF
ME	$4.40^{+0.99}_{-0.79}$	$2.5^{+0.7}_{-0.8}$
LF	...	$1.6^{+0.8}_{-0.7}$
(B)NN	$4.70^{+1.18}_{-0.93}$	1.8 ± 0.6
BDT	$3.74^{+0.95}_{-0.79}$	$2.1^{+0.7}_{-0.8}$
LFS	...	$1.5^{+0.9}_{-0.8}$
$\not\!\!E_T$ + jets	...	$4.9^{+2.6}_{-2.2}$
Combined	3.94 ± 0.88	$2.3^{+0.6}_{-0.5}$
Predicted[a]	$\sigma_{st} = 3.46 \pm 0.18$ for $M_t = 170$ GeV/c^2	
Predicted[b]	$\sigma_{st} = 3.14 \pm 0.31$	

[a] Kidonakis, 2006.
[b] Harris *et al.*, 2002.

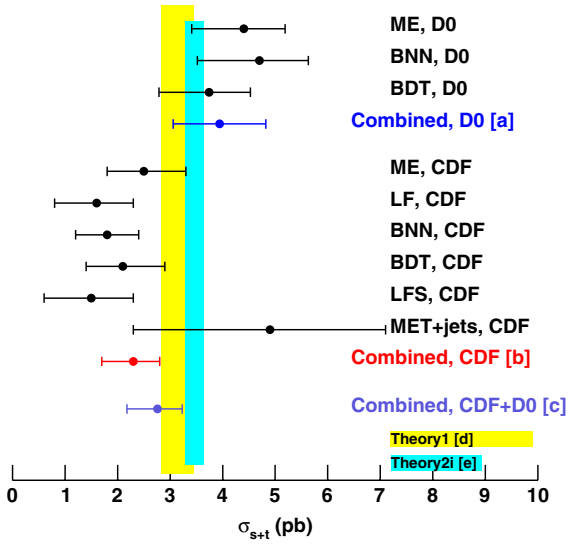

FIG. 48 (color online). Ideogram of the single-top cross-section measurements from D0 and CDF. [a] Abazov *et al.* (2008h); [b] Aaltonen *et al.* (2008d); [c] Tevatron Electroweak Working Group (2009a); [d] Smith and Willenbrock (1996); Harris *et al.* (2002); Campbell, Ellis, and Tramontano (2004); Sullivan (2004); Cao *et al.* (2005); Cao, Schwienhorst, and Yuan (2005); Frixione *et al.* (2006); Kidonakis (2006); [e] Stelzer, Sullivan, and Willenbrock (1997).

network trained on the outputs of the multivariate methods. Figure 46 shows the output of the three multivariate classifiers for D0, and Fig. 47 shows the same for three of the CDF classifiers. The cross sections for each MV method, the combined cross sections, and the fit probabilities are given in Table XXVI and in Fig. 48. The CDF and D0 results have also been combined by the Tevatron Electroweak Working Group (2009a).

The SM cross section is proportional to $|V_{tb}|^2$, so the cross-section results are used to measure $|V_{tb}|$. The only assumption is that $|V_{tb}| \gg |V_{ts}|$, $|V_{td}|$ such that there is not a significant contribution to the signal from initial-state s or d quarks being transformed into top quarks via a t-channel W boson. These results are shown in Table XXVII. The measured single-top cross section is in good agreement with the SM prediction with $|V_{tb}| \simeq 1$.

The precision of these results is limited by the statistics of the data samples. Both experiments are expected to continue these analyses through the end of the Tevatron running. In the most optimistic scenario this will result in analyzed data samples of up to 10 fb^{-1}. Assuming the results in Table XXVII scale as $1/\sqrt{\int \mathcal{L} dt}$, the uncertainty on $|V_{tb}|$ will be reduced approximately twofold.

TABLE XXVII. $|V_{tb}|$ values extracted from the single-top cross-section measurements. The first row is the 95% C.L. result when no constraint is placed on $|V_{tb}|$, and the second row is the result with the SM constraint $0 \leq |V_{tb}| \leq 1$.

D0	CDF
$\|V_{tb}\| > 0.78$	$\|V_{tb}\| > 0.71$
$\|V_{tb}\| = 1.07 \pm 0.12$	$\|V_{tb}\| = 0.9 \pm 0.11$

V. HIGGS BOSON

A. Precision electroweak constraints

As discussed in Secs. II.A and II.B, the standard model, with the $SU(2)_L \otimes U(1)_Y$ symmetry spontaneously broken via the vacuum-expectation value of a single Higgs-doublet field, is consistent with precision electroweak data. These data are so precise that they are sensitive to the mass of the Higgs boson at one loop, despite the fact that the Higgs mass enters only logarithmically. Figure 49 shows the constraints on the Higgs-boson mass from both precision electroweak measurements (the wide shaded band) and direct searches (the shaded areas). The precision data depend on the extrapolation of the fine-structure constant α from its measured value at low energy up to high energy, which suffers from an uncertainty associated with the contribution of low-energy QCD to the extrapolation. The solid line indicates the central value, and the shaded band takes into account all uncertainties. An alternative central value, associated with a different treatment of low-energy QCD, is indicated by the dashed line. The effect on the central value by including the NuTeV data, which has some tension with the other precision electroweak data, is shown by the dotted line.

It is striking that the precision data strongly prefer a Higgs-boson mass in the 100 GeV/c^2 region, while a purely theoretical analysis accommodates a Higgs boson as heavy as about 700 GeV/c^2 (Luscher and Weisz, 1988). Taken at face value, the precision data indicate the Higgs boson is not much heavier than the current lower bound of $m_H > 114$ GeV/c^2. It is also remarkable that the Tevatron experiments succeeded in excluding the region $163 < m_H < 166$ GeV/c^2.

B. Direct searches

The experimental strategy and sensitivity to discover the standard model Higgs boson at the Tevatron through direct searches depends strongly on the value of m_H. For direct searches, the sensitive range is limited to $m_H \lesssim 250$ GeV/c^2

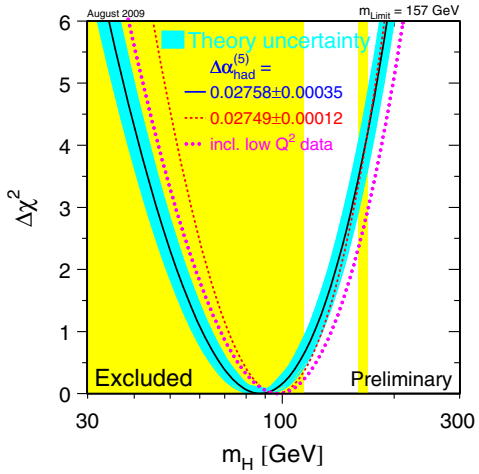

FIG. 49 (color online). The $\Delta\chi^2$ as a function of assumed Higgs mass resulting from fits to data assuming the SM. The exclusion regions from direct searches are also shown.

TABLE XXVIII. The production cross section and cross section times branching fraction for the low mass ($m_H < 135$ GeV/c^2) Higgs-boson search. Cross sections are in femtobarns. For the final states denoted $\ell\nu$ and $\ell\ell$, the branching fraction used is the sum of $\ell = e\mu$.

m_H (GeV/c^2)	$\sigma(p\bar{p} \to WH)$	$\sigma \times B(W \to \ell\nu)$	$\sigma(p\bar{p} \to ZH)$	$\sigma \times B(Z \to \ell\ell)$	$\sigma \times B(Z \to \nu\nu)$
100	286	63.6	167	11.2	33.4
110	209	46.4	124	8.35	24.8
120	153	34.0	92.7	6.24	18.5
130	115	25.5	70.9	4.77	14.2

where there exists sufficient center-of-mass collision energy at the parton level for an appreciable rate of Higgs-boson production via the gluon fusion (ggH) process which proceeds via a virtual quark loop (dominated by the top quark) (Djouadi, 2008).

For $m_H \lesssim 135$ GeV/c^2 (the "low mass Higgs" region), the dominant Higgs decay is to b-quark pairs. The next largest contribution to the Higgs decay in the low mass Higgs region is $H \to \tau\tau$ which has a branching ratio of $\sim 7\%$. In the case of $H \to bb$, the ggH production is not useful to the direct Higgs search even using the bb invariant mass because of overwhelming continuum bb production. Instead, the associated vector boson (VH) process where the Higgs boson is produced in association with a W or Z boson is used. The additional leptons which can result from decay of the vector boson via $W \to \ell\nu$, $Z \to \ell\ell$, or $Z \to \nu\nu$ with $\ell = e$, μ (Stange, Marciano, and Willenbrock, 1994a, 1994b), whether detected directly or indirectly through $\not\!\!E_T$, can be used to suppress backgrounds at the expense of a lower cross section for VH as compared to ggH.

The cross section and cross section times branching fraction for several Higgs masses in the low mass Higgs region (Tevatron New Phenomena and Higgs Working Group, 2009) are shown in Table XXVIII. In addition to the modes listed in Table XXVIII, the $WH \to WWW \to \ell^{\pm}\ell^{+'}\ell^{-'}$ channel provides some sensitivity in the transition region around $m_H \approx 135$ GeV/c^2 and vector boson fusion (VBF) $qq \to qqH$ and ggH modes provide sensitivity in $\tau\bar{\tau}$ final states.

For the low mass associated production channels VH in which the W or Z boson decay involves one or two charged lepton(s), an initial sample consistent with production of a vector boson decaying to charged and/or neutral leptons and having at least two jets is selected. This sample has a very low signal-to-noise ratio but is already dominated by vector boson events and therefore provides a control sample used to validate detector modeling and rate predictions of the dominant backgrounds in the final analysis.

The requirement that one or more of the jets in the event is consistent with production of a B hadron is added to the selection, dramatically reducing the contribution from the initially dominant Vjj background and increasing the signal purity. Nonlinear multivariate techniques for each final state are used to combine kinematic properties into a (typically) single variable in which a potential Higgs signal and backgrounds populate different regions. The distributions of these variables are then used as input to binned likelihood fits in which signal and background fractions are allowed to float within constraints of the total yield, predicted background contributions, and all uncertainties. The absence (presence) of a significant signal resulting from the fits determines the mass limit (indicates discovery).

The low mass Higgs searches using the $ZH \to \nu\nu bb$ channel and final states involving one or two τ lepton decays follow different strategies. The $ZH \to \nu\nu bb$ channel has significant background from multijet QCD processes without real vector boson decay[2] in which mismeasurement of jets results in significant $\not\!\!E_T$. In this channel, an additional step (described later in this section) is added to improve an understanding of this background. The search using final states that involve either one or two τ leptons does not make use of b-jet identification since the τ leptons can arise either from Higgs-boson decay or from W or Z decay.

The latest low mass Higgs searches from CDF and D0 are described in Sec. V.B.5. The most recent combination of low mass results, which includes some preliminary results not presented here, is described in Secs. V.C.

For $m_H \gtrsim 135$ GeV/c^2 (the "high mass Higgs" region), the dominant Higgs decay is to W boson pairs with the next largest contribution being $H \to ZZ^{(*)}$. Aside from a region around $m_H = 150$ GeV/c^2 where BR($H \to ZZ^{(*)}$) peaks to $\sim 10\%$, the $H \to WW^{(*)}$ decay where one of the final-state W bosons is off shell for M_H less than twice the W mass completely dominates over the sensitive region of the Tevatron. The Higgs production cross section and branching fractions for several Higgs masses in the high mass region are shown in Table XXIX. The standard model Higgs-boson branching fraction to WW^* varies from 7.5% at 115 GeV/c^2 to 73.5% at 200 GeV/c^2 with a maximum of 96.5% at ≈ 170 GeV/c^2 (Djouadi, 2008). For $M_H \sim 170$ GeV/c^2, the standard model Higgs boson decays almost exclusively to two on-shell W bosons, making this a region where the Tevatron has the best chance at a discovery or an exclusion.

At the Tevatron, the most sensitive Higgs search channel over the range $135 \lesssim m_H \lesssim 200$ GeV/c^2 is $gg \to H \to WW^{(*)} \to \ell\nu\ell\nu$, where the two charged leptons in the final state are of opposite charge (Han, Turcot, and Zhang, 1999; Han and Zhang, 1999). The $\ell\nu\ell\nu$ final state represents 6.0% of all WW^* decays, where ℓ is either an electron or a muon, including those from τ leptons produced in the W decays. Over the last few years, the experimental search for a high mass Higgs in decay to WW at the Tevatron has evolved substantially to include powerful multivariate techniques and additional $H \to WW^{(*)}$ processes such as VBF $H \to WW^{(*)}$ and $VH(\to WW^{(*)})$. The latest high mass Higgs searches in the $H \to WW^{(*)}$ channel from CDF and D0 are described in

[2]Such backgrounds are also present in the other channels, but at a much lower fraction of the total background.

TABLE XXIX. The production cross section and cross-section times branching fraction for the high mass ($m_H > 135$ GeV/c^2) Higgs-boson search. Cross sections are in femtobarns.

m_H (GeV/c^2)	$\sigma(gg \to H)$	σ (VBF)	$B(H \to WW)$
150	548	45.7	0.682
160	439	38.6	0.901
170	349	33.6	0.965
180	283	28.6	0.934

Sec. V.B.5. A combination of these results is described in Sec. V.C.

The following sections describe the individual channels used in the Higgs search starting with the low mass channels $WH \to \ell\nu bb$, $ZH \to \ell\ell bb$, $ZH \to \nu\nu bb$, and τ final states, and finishing with the high mass $H \to WW^{(*)} \to \ell\nu\ell\nu$ search. The Higgs-boson section concludes with a presentation of the most recent set of CDF and D0 combined limits.

1. $WH \to \ell\nu bb$ final state

This final state has the largest cross section times branching ratio of the entries shown in Table XXVIII, and it also gives the most sensitivity to Higgs-boson production for $M_H \lesssim 135$ GeV/c^2. Both CDF (Aaltonen *et al.*, 2009g) and D0 (Abazov *et al.*, 2009j) carried out searches in this final state. The currently published results for D0 use a sample of $\int \mathcal{L}dt = 1.0$ fb^{-1}. The CDF published results use a sample of $\int \mathcal{L}dt = 2.1$ fb^{-1}, and preliminary results have been reported by both collaborations which use up to $\int \mathcal{L}dt = 4$ fb^{-1}. The search strategies used by the two collaborations in the WH channel are generally similar.

The initial event selection requires one high-p_T electron or muon, large $\not\!\!E_T$, and two or more jets. This selection mirrors the ℓ, ν, and bb pair present in the final state. CDF requires the events to be selected by a trigger based on the presence of a high-energy electron or muon.[3] The D0 analysis requires $\ell = e$ events to be selected by single-electron or electron plus jet triggers. For the muon final state D0 uses a two phase trigger selection. In the first phase, the events are required to be selected based on at least one of a set of single-lepton or single-lepton plus jet triggers, and all yields are predicted and compared with data. After establishing agreement in this pass, the analysis is repeated allowing events to be selected by any trigger. The yield increases by an amount predicted by the inefficiency of the triggers for the first pass and all kinematic distributions remain in agreement after a simple yield scaling to 100% trigger efficiency.

At this stage, the dominant event source is W + jets with the jets arising from light quark (u, d, s, c) production. The signal-to-background ratio is then improved by requiring one or two of the jets in the event to be identified as consistent with b quark production. The D0 b identification algorithm (Scanlon, 2006) uses a NN. The NN is trained and verified on a combination of data and simulation, with the critical efficiencies and misidentification rates determined from data control samples. The CDF analysis used three different b identification algorithms. Jets are b tagged by one or more algorithms based on the presence of a secondary vertex (SECVTX) (Acosta *et al.*, 2005e), a neural network (Aaltonen *et al.* (2008e), or signed impact parameters (JP) (Abulencia *et al.*, 2006b).

The signal purity is greatest when two b jets are required, but this introduces significant efficiency loss compared to the case in which only one b jet is required. To gain the most sensitivity, both categories of events, single b tagged and double b tagged, are retained, but they are analyzed separately. Optimization studies indicate that for the single-tag channel, a rather restrictive tagging requirement is needed to control the background contribution from events with light-flavor (lf) jets misidentified as b jets while for the double-tag channel, a less stringent requirement suffices thereby giving increased per jet tagging efficiency. The D0 single-tag analysis uses a b-tag operating point which gives a typical efficiency of 48% with misidentification rate of 0.5% and an operating point for the double-tag analysis which gives an efficiency of 59% and a misidentification rate of 1.7%. The CDF event selection divides events into three exclusive categories based on which algorithms identify a jet as b tagged. The first category contains events which have two jets tagged by the SECVTX algorithm. The second category contains events not selected into the first category which have one jet identified by the SECVTX algorithm and one by the jet probability algorithm. The third category contains events which are not selected into either of the other two categories and have one jet identified by both the SECVTX and NN algorithms.

The sensitivity of the analyses is further improved by using kinematic properties of the events to distinguish signal and background events. The most important variable is the mass of the dijet system corresponding to the Higgs decay. For single-tagged events, the mass is computed using the tagged jet and the highest p_T jet remaining, and for the double-tagged events the mass is computed using the two tagged jets. In addition to the mass, other variables can also distinguish signal and background on a statistical basis. To make best use of these, both experiments use a neural network to enhance the separation of signal and background in the final step of the analysis. The CDF neural network has six input variables and the D0 network has seven input variables.[4] The variables used by each experiment are listed in Table XXX for comparison. Because of limited statistics in the $W + 3$ jet sample, D0 uses the NN only for the $W + 2$ jet case and uses the dijet mass for the $W + 3$ jet case. Backgrounds to the WH search include W + jets production [including jets arising from heavy-flavor (hf) production], $t\bar{t}$, single-top, diboson production (WW, WZ, and ZZ) and a small contribution from multijet events in which either the lepton is actually a jet misidentified as a lepton or the lepton arises from heavy-flavor decay and the jet energy is not reconstructed so the lepton appears to be isolated. Both experiments estimate the $t\bar{t}$, single-top, and diboson yields using the product of the theoretical (N)NLO cross section for each process, the luminosity and acceptance times efficiency for each process. Corrections are applied

[3]The event selection in recent preliminary results from CDF include additional events in this channel which are selected by $\not\!\!E_T$ triggers.

[4]Recent preliminary results also used the matrix element method adapted from the top mass measurement and decision trees for the multivariate technique instead of neural networks.

TABLE XXX. The neural network inputs for the CDF and D0 WH analyses. Here J_i denotes the ith jet in a list ordered by jet E_T in which J_1 is the highest E_T jet in the event. $M^{\min}_{\ell\nu j}$ is the mass of the lepton, $\not\!\!E_T$, and the jet (J_1 or J_2) which gives the lower mass value. Finally, $\nu_{\max}$ is the three momentum of the neutrino in which $|p_Z|$ is the larger of the two values calculated when forcing the lepton and neutrino system to have a mass equal to the W boson mass.

CDF	D0
M_{JJ+} invariant mass of J_1 and J_2 and the closest loose jet if $\Delta R(J, J_{\text{loose}}) < 0.9$	M_{JJ} invariant mass of J_1 and J_2
ΣE_T (loose jets)	$E_T(J_1)$
$p_T(J_1) + p_T(J_2) + pT(\ell) - \not\!\!E_T$	$E_T(J_2)$
$M^{\min}_{\ell\nu j}$	$\Delta R(J_1, J_2)$
$\Delta R(\ell, \nu_{\max})$	$\Delta\phi(J_1, J2)$
$\lvert\vec{p}_T(\ell) + \vec{p}_T(\not\!\!E_T) + \vec{p}_T(J_1) + \vec{p}_T(J_2)\rvert$	$\lvert\vec{p}_T(\ell) + \vec{p}_T(\not\!\!E_T)\rvert$
	$\lvert\vec{p}_T(J_1) + \vec{p}_T(J_2)\rvert$

based on comparison of data and simulated control samples. The W + jets background cross sections are poorly known, and data-driven approaches are used to estimate these yields. The multijet background is hard to model from simulation, so data-driven methods are also used for this background. The two experiments use different data-driven methods as outlined below.

The total W + jets background after b tagging in the CDF result is estimated separately for W + lf events and W + hf events. The W + lf contribution is estimated by applying data-derived mistag probabilities to untagged W + jets samples. Three different tagging algorithms are used in the analysis, and the mistag probability determination differs for each of these. For the SECVTX and JP tagging algorithms, the mistag probability (Acosta *et al.*, 2005e; Abulencia *et al.*, 2006b) is derived using events with a negative decay length with a correction applied to account for the heavy-flavor content of the control sample used to determine the mistag probability. For the JP algorithm, the mistag probability is parametrized as a function of η, primary vertex z position, jet E_T, scalar transverse energy, and vertex and track multiplicity. For the NN-based tagging algorithm, a light-flavor rejection factor derived from control data samples is used. The W + hf contribution is determined by measuring the heavy-flavor faction in W + jets events and applying a b-tagging efficiency to these events. The initial heavy-flavor fraction is derived from ALPGEN and PYTHIA simulation and is corrected by a factor of 1.4 ± 0.4 derived from a jet control data sample. The b-tagging efficiencies are determined from simulation and checked using control data samples.

The W + jets background yields after b tagging in the D0 result are fixed by normalizing the simulated events to the untagged W + jets data after subtracting the other backgrounds from the data. The relative contributions of the W + lf, $W + c\bar{c}$, and $W + bb$ in the untagged sample are fixed to the cross-section ratios predicted by MCFM. The yields in the b-tagged sample are then computed by applying flavor-based (mis)identification probabilities to the jets in simulated events. The probabilities (one for u-, d-, and s-quark initiated jets, one for c-quark initiated jets and for b-quark initiated jets) are derived using data control samples (Scanlon, 2006) and are parametrized as functions of jet p_T and η.

The small background from multijet events is difficult to simulate accurately, so this component is also determined from control data samples. For CDF, a control sample is selected using events which have nonisolated leptons and low $\not\!\!E_T$, and the yield in the signal sample is determined by extrapolating the yield from this sample into the signal region having isolated leptons and high $\not\!\!E_T$. For D0, this background is determined by selecting a multijet dominated control sample with kinematics similar to the WH events, and then applying a probability that these events would be misidentified and appear in the signal sample. The multijet control sample is selected by requiring lepton candidates which pass very loose isolation requirements, and the background yield is computed by applying the event-by-event probability that these loose-isolation events would pass the standard isolation requirement and thus appear in the signal sample.

Table XXXI shows the data yields and background and signal predictions for the CDF analysis, and Table XXXII shows the yields for the D0 analysis. The predicted Higgs yield includes not only WH events, but also a small contribution from $ZH \to \ell\ell bb$ events in which one of the leptons

TABLE XXXI. The predicted and observed yields for the CDF 2 fb^{-1} WH search separated by the detector region. From Aaltonen *et al.* (2009g).

	Central region			Plug region		
Pretag events	32242			5879		
b tagging	ST + ST	ST + JP	ST + NN	ST + ST	ST + JP	ST + NN
Mistag	3.88 ± 0.35	11.73 ± 0.92	107.1 ± 9.38	1.00 ± 0.18	3.18 ± 0.49	28.47 ± 3.30
Wbb	37.93 ± 16.92	31.15 ± 14.03	215.6 ± 92.34	7.40 ± 3.96	6.23 ± 3.37	43.09 ± 12.33
Wcc	2.88 ± 1.25	7.87 ± 3.43	167.0 ± 62.14	0.96 ± 0.49	1.53 ± 0.81	33.37 ± 9.55
$t\bar{t}$(6.7 pb)	19.05 ± 2.92	15.56 ± 2.39	60.68 ± 9.30	2.14 ± 0.34	1.79 ± 0.31	7.17 ± 1.00
Single top (s-ch)	6.90 ± 1.00	5.14 ± 0.75	14.38 ± 2.09	0.69 ± 0.10	0.51 ± 0.08	1.53 ± 0.20
Single top (t-ch)	1.60 ± 0.23	1.87 ± 0.27	29.57 ± 4.33	0.22 ± 0.04	0.24 ± 0.04	3.54 ± 0.47
WW	0.17 ± 0.02	0.93 ± 0.11	15.45 ± 1.91	0.01 ± 0.01	0.12 ± 0.04	3.00 ± 0.20
WZ	2.41 ± 0.26	1.84 ± 0.20	7.59 ± 0.81	0.58 ± 0.06	0.42 ± 0.05	1.62 ± 0.09
ZZ	0.06 ± 0.01	0.08 ± 0.01	0.31 ± 0.03	0.00 ± 0.01	0.01 ± 0.01	0.02 ± 0.00
$Z \to \tau\tau$	0.25 ± 0.04	1.29 ± 0.20	7.27 ± 1.12	0.00 ± 0.01	0.01 ± 0.01	0.24 ± 0.03
non-W QCD	5.50 ± 1.00	9.55 ± 1.73	184.7 ± 33.04	1.16 ± 0.44	1.51 ± 0.55	18.34 ± 5.54
Total background	80.6 ± 18.8	87.0 ± 18.0	809.6 ± 159.4	14.2 ± 4.0	15.5 ± 3.6	140.4 ± 16.9
WH signal (120 GeV/c^2)	0.85 ± 0.10	0.60 ± 0.07	1.70 ± 0.14	0.09 ± 0.01	0.06 ± 0.01	0.20 ± 0.01
Observed events	83	90	805	11	13	138

TABLE XXXII. The predicted and observed yields for the D0 1 fb^{-1} WH search. From Abazov *et al.* (2009j).

	$W+2$ jet $1b$ tag	$W+2$ jet $2b$ tag	$W+3$ jet $1b$ tag	$W+3$ jet $2b$ tag
WH	2.8 ± 0.3	1.5 ± 0.2	0.7 ± 0.1	0.4 ± 0.1
WZ	34.5 ± 3.7	5.3 ± 0.6	9.1 ± 1.0	1.7 ± 0.2
$Wb\bar{b}$	268 ± 67	54 ± 14	87 ± 22	22.7 ± 5.7
W + jets	347 ± 87	14.0 ± 4.4	96 ± 24	8.5 ± 2.7
$t\bar{t}$	95 ± 17	37.4 ± 7.0	156 ± 29	81 ± 15
Single t	49.4 ± 9.0	12.4 ± 2.3	15.7 ± 2.9	6.7 ± 1.2
m jet	104 ± 29	8.9 ± 2.1	54 ± 15	8.7 ± 2.1
Total	896 ± 177	132 ± 27	418 ± 76	129 ± 24
Data	885	136	385	122

(ℓ) is not identified and thus generates $\not\!\!E_T$ and a final state consistent with the WH final state.

Both CDF and D0 derive their final result by comparing the predicted and observed spectra using binned likelihoods. For both experiments, the single-tag and double-tag samples are separated and their likelihoods combined for the final results.

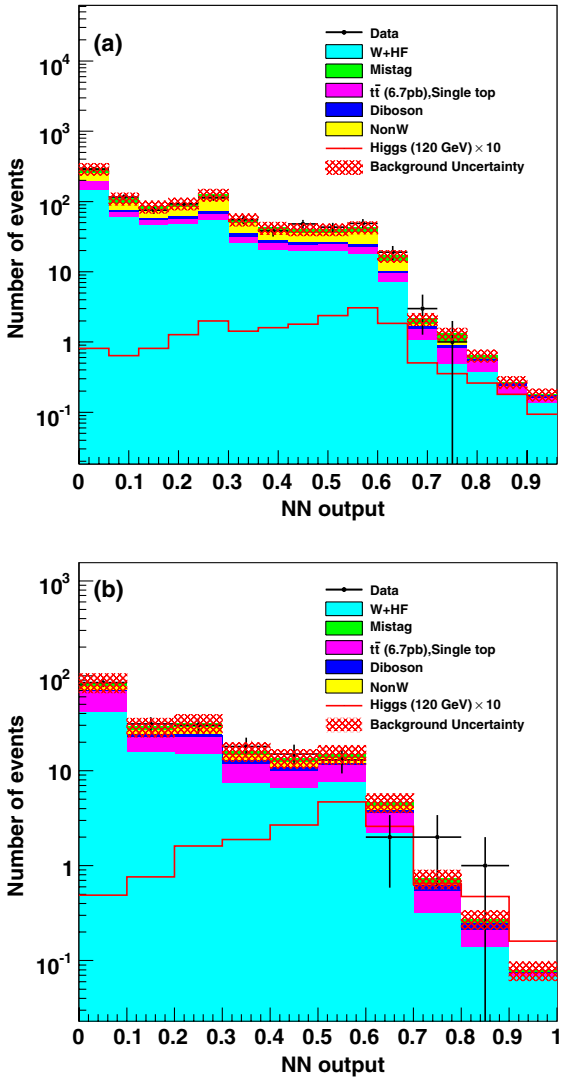

FIG. 50 (color online). The NN output distributions for (a) single- (ST + NN) and (b) double-tagged (ST + ST, ST + JP) events from the CDF 2 fb^{-1} WH search.

D0 further separates the samples into events with exactly two jets and events with three jets. When determining the final result, CDF uses the dijet mass as the input to their likelihood. D0 uses the NN output for the two jet events and the dijet mass for three jet events. The likelihood methods are described in Sec. V.C.

Systematic uncertainties are evaluated by both experiments for trigger efficiency, lepton identification efficiency, b-jet (mis)identification efficiency, the jet identification efficiency and jet energy calibration, multijet background calculation method, luminosity, and theory cross sections used for background and signal event yield calculations. CDF additionally reports uncertainties from parton density functions and initial- and final-state radiation modeling. D0 reports an additional systematic from the W + jets simulation derived by comparing shapes of distributions of data and simulated events before b tagging.

The CDF NN output distributions for the tagged event selections are shown in Fig. 50. The D0 NN output distribution (two jet events) and dijet mass distribution (three jet events) are shown in Fig. 51. The CDF and D0 cross-section limits for the $WH \to \ell\nu bb$ final state only are shown in Figs. 52 and 53, respectively. The result from combining the results for all low mass final states is shown in Sec. V.C.

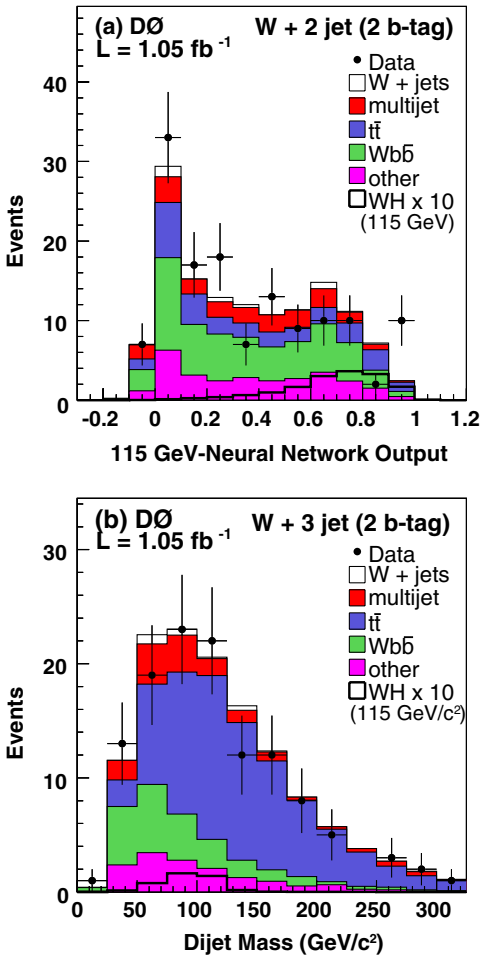

FIG. 51 (color online). (a) The NN output for double-tagged dijet events and (b) the dijet mass for double-tagged three jet events from the D0 WH search.

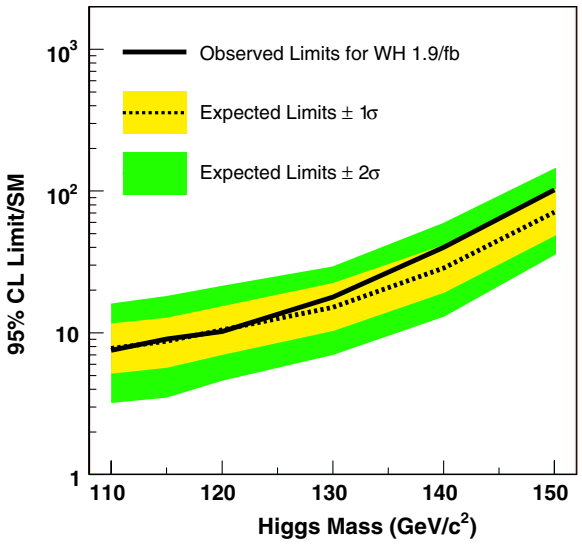

FIG. 52 (color online). The cross-section limits from the CDF WH search.

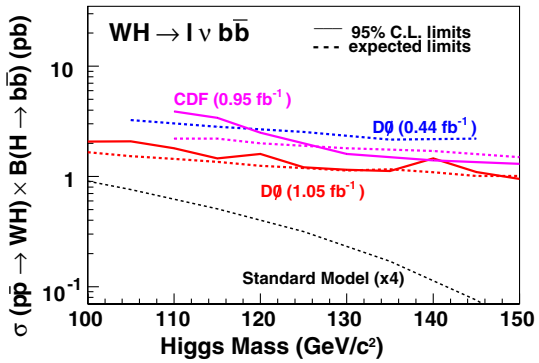

FIG. 53 (color online). The cross-section limits from the D0 WH search.

2. $ZH \to \ell\ell bb$ final state

The final state from $ZH \to \ell\ell bb$ events has the lowest production rate among those shown in Table XXVIII but has the highest purity. A similar strategy is taken for this final state as for the WH final state. An initial sample of Z + dijet events is selected, the purity is improved by requiring b jets, and the final result is determined by using either the invariant mass distribution or the output of a neural network as inputs to a shape-based limit setting program. Both D0 (Abazov *et al.* (2007e) and CDF (Aaltonen *et al.*, 2008f) published results in this final state. The D0 publication uses a data sample corresponding to $\int \mathcal{L}dt = 0.45$ fb^{-1}. The CDF published results correspond to $\int \mathcal{L}dt = 1.0$ fb^{-1}.

The initial selections for both experiments require events with two leptons whose invariant mass is consistent with a Z boson and two additional jets. The backgrounds in this channel arise from Z + jets, $t\bar{t}$ events, diboson production, and from jets misidentified as leptons or a lepton + jet system being misidentified as an isolated lepton. They are determined using a combination of simulated events and data control samples in essentially the same manner as for the WH channel. One difference with respect to the WH calculation is that sidebands of the $\ell\ell$ invariant mass distribution are used by D0 to determine the misidentification and false isolation background. Both experiments identify b jets using secondary vertex algorithms.[5] The CDF result splits the final tagged sample into single- and double-tagged samples as in the WH analysis, but the D0 result does not. The D0 result is derived using the dijet mass distribution only, while the CDF result is based on the binned likelihood of a NN output. The sources of systematic uncertainties for these channels are the same as for the WH result. Table XXXIII shows the yields for the single- and double-tag analyses from CDF, and Table XXXIV shows the yields for the dijet and double-tagged samples for D0, respectively. Figure 54 (Fig. 55) shows the dijet invariant mass (neural network output) distribution from the D0 (CDF) analysis. This distribution is used as the input to the limit setting program.

Systematic uncertainties are included for trigger and lepton identification efficiencies, parton density functions, background cross sections, b-tagging efficiencies, jet energy reconstruction, and the methods used to estimate instrumental backgrounds. The CDF result also includes a systematic from the top mass uncertainty. The systematic uncertainties for the D0 measurement range between 2% and 20% expressed as a fraction of the total background. The systematic uncertainties for the CDF measurement range between 1% and roughly 25% of the total background. The largest contribution for both experiments is from the background cross sections.

TABLE XXXIII. Single- and double-tagged yields for the CDF 1.0 fb^{-1} $ZH \to \ell\ell bb$ search.

Source	Single tagged	Double tagged
$Z + bb$	35.1 ± 14.6	6.3 ± 2.5
$Z + c\bar{c}$	21.8 ± 8.5	1.0 ± 0.4
$Z + q\bar{q}$	32.3 ± 5.5	1.0 ± 0.2
$t\bar{t}$	5.2 ± 1.0	2.8 ± 0.6
ZZ	4.0 ± 0.8	1.3 ± 0.3
WZ	1.2 ± 0.2	0.04 ± 0.01
Non-Z	1.9 ± 1.4	0.2 ± 0.2
Total expected	101.5 ± 32	12.7 ± 4.1
Observed	100	11
Signal yield	0.44	0.23

TABLE XXXIV. Dijet and double-tagged sample yields for the D0 0.45 fb^{-1} $ZH \to \ell\ell bb$ search.

Source	Dijet	Double tagged
$Z + bb$	17.4	3.3
$Z + jj$	851	3.8
$t\bar{t}$	12.3	3.9
$WZ + ZZ$	30.6	0.74
Non-Z	44.1	0.59
Total exp.	956	12.3
Observed	1008	15

[5]For D0 this differs from the WH case because the published ZH results predate the availability of the NN tagger. More recent D0 preliminary results use the same NN tagger described in the WH analysis.

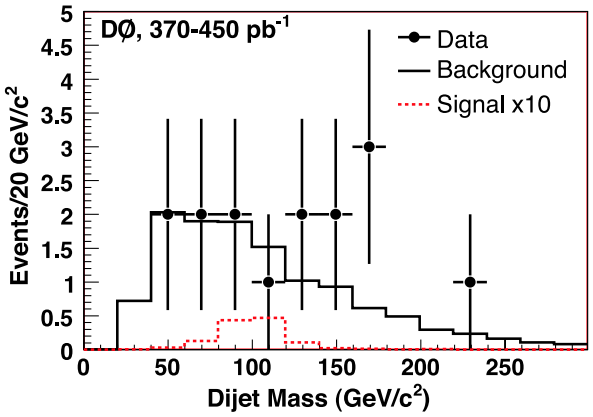

FIG. 54 (color online). Dijet mass distribution for the D0 1.0 fb^{-1} $ZH \to \ell\ell bb$ analysis.

The final limits, derived using the same methods as the WH results, are shown for CDF in Fig. 56 and for D0 in Fig. 57. As expected these channels have considerably less sensitivity than the WH channels because of the significantly lower signal cross section times branching fraction.

3. $ZH \to \nu\nu bb$ and related final states

The $ZH \to \nu\nu bb$ final state has a production rate intermediate between the WH and $ZH \to \ell\ell bb$ final states. This final state also has a significant contribution from the process $WH \to \ell\nu bb$ in which the charged lepton ℓ escapes detection. This is particularly true for the case $\ell = \mu$ because the muon leaves very little energy in the calorimeter and thus results in event $\not\!\!E_T$ similar to that from $Z \to \nu\nu$ decay.

Unlike either of the previously discussed final states, the $ZH \to \nu\nu bb$ final state has no charged leptons from vector boson decay. This implies a significantly increased background from SM multijet events in which $\not\!\!E_T$ arises from mismeasurement. This background is difficult to model from simulation, and analyses of this final state must develop techniques to measure it using data control samples. Both CDF (Aaltonen *et al.*, 2008g) and D0 (Abazov *et al.*, 2010a) published results in this final state. The two experiments developed different methods for controlling and estimating the multijet background.

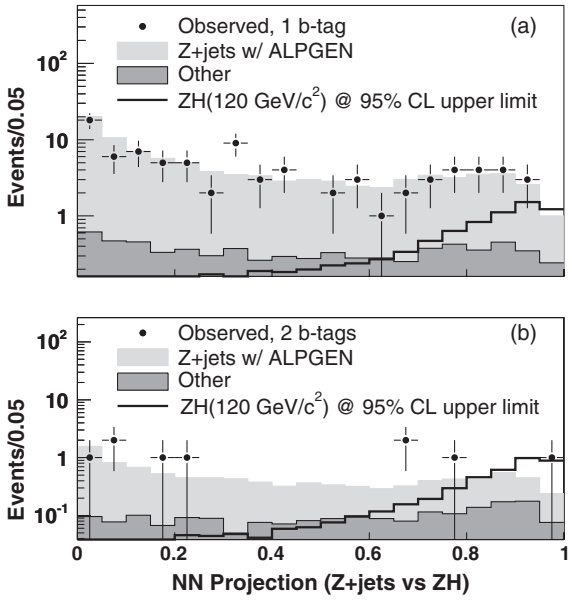

FIG. 55. NN distributions for the (a) single-tagged and (b) double-tagged samples from the CDF 1.0 fb^{-1} $ZH \to \ell\ell bb$ analysis. The 95% C.L. upper bound cross section is 19× the SM prediction.

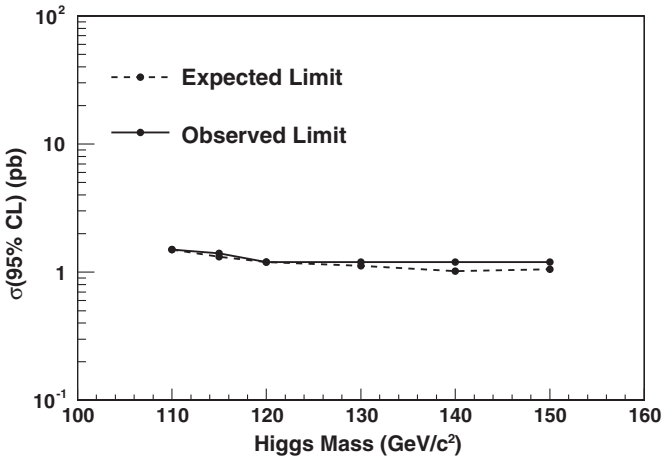

FIG. 56. Expected and observed limits for the CDF 1.0 fb^{-1} $ZH \to \ell\ell bb$ analysis.

a. CDF search

The CDF analysis uses a data sample corresponding to 1 fb^{-1} and begins with selection of events passing a $\not\!\!E_T$ trigger with level one $\not\!\!E_T > 25$ GeV, a level two requirement of two jet clusters having $E_T > 10$ GeV, and a level three requirement of $\not\!\!E_T > 35$ GeV. At least one of the level two jets must also satisfy $\eta < 1.1$. The initial offline selection ("pretag") requires events to have $MET > 50$ GeV and exactly two jets with $E_T > 20$ GeV. One of the jets must have $E_T > 35$ GeV, and the other must have $E_T > 25$ GeV. Additionally, one of the jets must satisfy $|\eta| < 0.9$, and the other jet must satisfy $|\eta| < 2.4$. The two jets must also have $\Delta\phi > 1.0$ rad, and events with high p_T, isolated leptons are vetoed. Finally, at least one of the jets is required to have a secondary vertex b tag.

All nonmultijet backgrounds, $t\bar{t}$, W + jets, Z + jets, and diboson production are modeled using simulated events. The

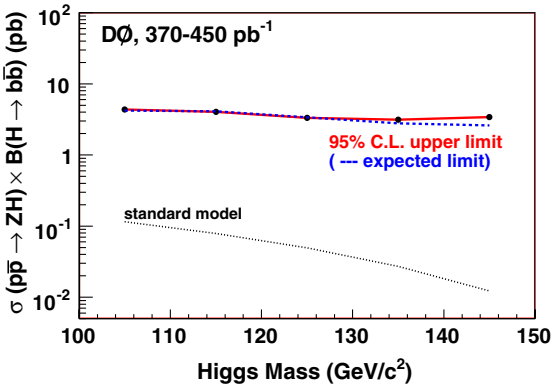

FIG. 57 (color online). Expected and observed limits for the D0 0.45 fb^{-1} $ZH \to \ell\ell bb$ analysis.

TABLE XXXV. Definitions of the three regions (CR1, CR2, and Signal) in the CDF $VH \to \not\!\!E_T bb$ search. $\Delta\Phi(\vec{E}_{T1(2)}, \not\!\!\vec{E}_T)$ is the angle between the $\not\!\!E_T$ and the jet with the highest (second highest) E_T.

Region	Dominant source	Selection
CR1	Multijet	Leptons vetoed
		$\Delta\Phi(\vec{E}_{T2}, \not\!\!\vec{E}_T) < 0.4$
CR2	EW, $t\bar{t}$	Lepton required
		$\Delta\Phi(\vec{E}_{T2}, \not\!\!\vec{E}_T) > 0.4$
Signal		Leptons vetoed
		$\Delta\Phi(\vec{E}_{T1}, \not\!\!\vec{E}_T) > 0.4$
		$\Delta\Phi(\vec{E}_{T2}, \not\!\!\vec{E}_T) > 0.4$

multijet background is studied by dividing the sample into two control regions and a signal region. The regions are defined in Table XXXV. The multijet background in all regions is divided into two components: (1) events with only light-flavor (u, d, and s) quarks in which one or more of the jets is misidentified with a secondary vertex, and (2) events with c and b quarks. The contribution from light-flavor jets is determined using a control sample with no tags to which a misidentification factor is applied. The heavy-flavor contribution is determined using simulated events with

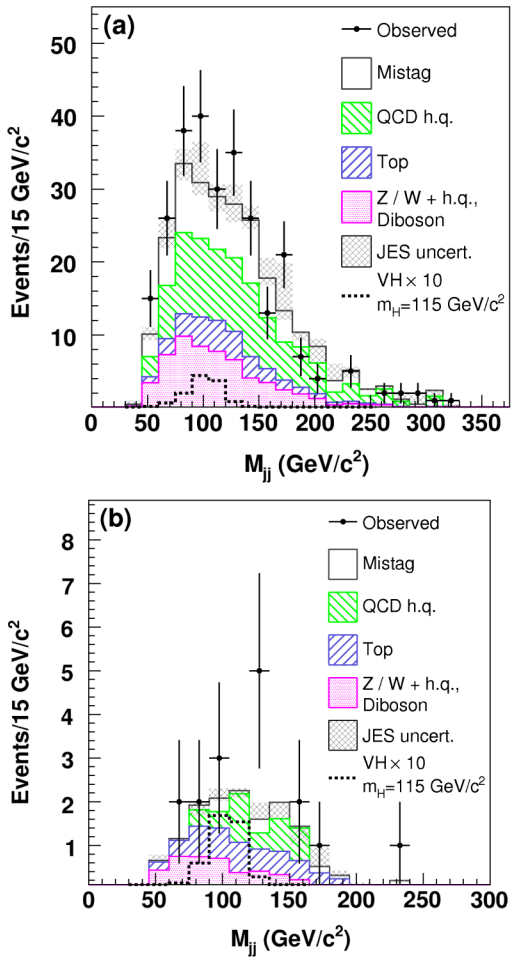

FIG. 58 (color online). The dijet invariant mass distributions for the (a) single-tagged and (b) double-tagged CDF searches in the $VH \to \not\!\!E_T bb$ final state.

TABLE XXXVI. Yields in the CDF $VH \to \not\!\!E_T bb$ analysis.

Source	Single tagged	Double tagged
Multijet	93 ± 23	3.74 ± 1.27
$t\bar{t}$	27.3 ± 3.8	4.88 ± 0.8
Diboson	7.0 ± 1.4	0.79 ± 0.19
W + hf	33.4 ± 16.2	1.65 ± 0.86
Z + hf	18.3 ± 8.1	1.67 ± 0.77
Mistags	69 ± 9	1.64 ± 0.48
Total	248 ± 43	14.4 ± 2.7
Observed	268	16

normalization factors for single-tag and double-tag topologies determined by forcing the data yields and the sum of all backgrounds to agree (before dividing the sample into the three regions). The scale factors are 1.30 ± 0.4 (1.47 ± 0.07) for the single (double) b-tagged events.

The final analysis selection is determined by optimizing $S/\sqrt{(B)}$ where S is the total signal yield, including the contribution from $WH \to \ell\nu bb$ in which the lepton is not identified, and B is the total background. The optimization is carried out only for the signal region. The final selection then requires $\Delta\phi(j_1, j_2) > 0.8$, $H_T/H_T > 0.454$, $E_T^{j_1} > 60$ GeV, and $\not\!\!E_T > 70$ GeV. Here H_T is the scalar sum of the jet E_T values, H_T is the magnitude of the vector sum, and j_1 (j_2) denotes the jet with the highest (second highest) E_T.

The systematic uncertainties arise from a number of sources. For the CDF analysis the dominant uncertainty in the jet energy calibration which varies between 10% and 26% for multijet and V + jets (including heavy-flavor) backgrounds, but is only 8% for signal events. The other dominant systematic arises from the calculated cross sections used to normalize backgrounds. This ranges between 11% and 40% for a given source depending on the samples. The total systematic is 17% for the single-tagged analysis and 19% for the double-tagged analysis.

Figure 58 shows dijet invariant mass for the single- and double-tagged events in the signal region. The yields are given in Table XXXVI. The limits on Higgs production are calculated using the same procedure as for the previous two channels, and they are shown in Fig. 59.

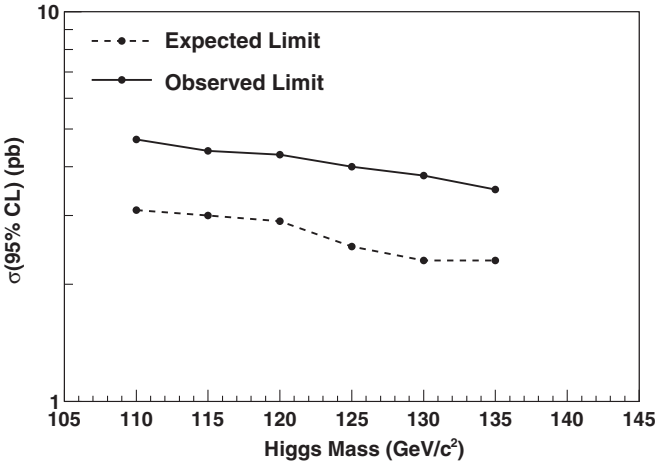

FIG. 59. Expected and observed 95% C.L. upper bounds on the VH production cross section for the CDF $\not\!\!E_T + bb$ search.

TABLE XXXVII. The predicted and observed yields for the D0 $VH \to \not{E}_T bb$ analysis for the untagged control sample and the single- and double-tagged analysis samples after applying the multijet BDT selection.

Sample	ZH	WH	W + jets	Z + jets	Top	VV	Multijet	Total background	Observed
Preselection	13.73 ± 1.37	11.64 ± 1.17	19 069	9432	1216	1112	1196	32025 ± 4037	31 718
Single tagged	4.16 ± 0.42	3.60 ± 0.37	802	439	404	60	125	1830 ± 255	1712
Double tagged	4.66 ± 0.58	4.00 ± 0.50	191	124	199	24	<8	538 ± 87	514

b. D0 search

The published D0 analysis uses a data sample corresponding to $\int \mathcal{L} dt = 5.2$ fb^{-1}. Events selected for this analysis must satisfy a trigger requiring two acoplanar jets and $\not{E}_T$ in which the kinematic thresholds varied as a function of the instantaneous luminosity. The primary requirements of the initial offline event preselection are at least two jets with $E_T > 20$ GeV and $|\eta| < 2.5$, $\Delta\phi(j_1, j_2) < 165°$, and $\not{E}_T > 20$ GeV. This is divided into four samples: (1) a signal sample defined by the additional requirements of $\not{E}_T > 40$ GeV, $S > 5$, $D < \pi/2$, and a veto of events with high-p_T, isolated leptons; (2) an electroweak test sample enhanced in $W \to \mu\nu$ events and defined similarly as for the signal sample, but requiring the presence of a high p_T, isolated muon; (3) a multijet modeling sample defined similarly to the signal sample except $D > \pi/2$; and (4) a multijet enriched sample used to confirm the background model predicted using the multijet modeling sample and defined by $\not{E}_T > 30$ GeV and no requirement on S. Here S is the significance of the $\not{E}_T$ and $D \equiv \Delta\phi(\vec{\not{E}}_T, \vec{\not{T}}_T = \phi_{\not{E}_T} - \phi_{\not{T}_T})$ in which $\not{T}_T$ is the magnitude of the vector sum of the transverse momentum of the tracks in the event and ϕ_i is the azimuthal angle of either $\not{E}_T$ or $\not{T}_T$.

The presence of b hadrons from the $H \to bb$ signal decay is used to improve the signal-to-noise ratio. Events were additionally required to have a least one of the two highest E_T jets identified as being consistent with a b hadron jet as determined by a high purity (tight) b-jet identification requirement. Events are then categorized as double tagged if the remaining one of the two highest E_T jets satisfies a lower purity (loose) identification requirement. Events without an additional tag are denoted as single tagged. For the tight requirement, the per jet identification efficiency is 50% with a misidentification probability of 0.5%. The loose requirement has an efficiency of 70% with a misidentification probability of 6.5%. Table XXXVII shows the data yield and prediction for the initial preselection and for the single- and double-tagged samples and the expected Higgs-boson signal for a Higgs boson of mass 115 GeV/c^2.

The backgrounds from $t\bar{t}$, W + jets, Z + jets, and diboson processes are estimated using simulated events. These results are validated using the EW enriched control sample. The shape of the multijet background is taken from the multijet modeling sample, and the normalization is determined by forcing the number of multijet events plus the number of SM predicted background events to equal the data yield in the preselection sample. This procedure is validated by comparing the prediction with the multijet enriched sample.

The signal-to-background separation is then further improved using BDTs. For each m_H considered, a multijet boosted decision tree (MJ BDT) with 23 input variables is trained on Higgs signal and multijet backgrounds. Events which have a MJ BDT output greater than 0.6 are retained. These events are then input to a second BDT (SM BDT) trained on the remaining backgrounds and Higgs signal events using the same 23 variables input to the MJ BDT. Figure 60 shows the BDT outputs for the data, predicted background, and signal. The agreement between data and prediction is good. Limits are extracted by fitting signal and background SM BDT outputs to the data distribution using the same modified frequentist algorithm as was used for the previously described D0 results. Figure 61 shows the Higgs cross-section limits from the D0 analysis.

The systematic uncertainties for the D0 result are dominated by similar sources as for the CDF analysis. The D0 jet energy calibration systematic is <10%, and the background normalization systematic varies between 6% and 20%. D0 also reports additional systematic uncertainties from luminosity, trigger, and identification efficiencies and b-tagging

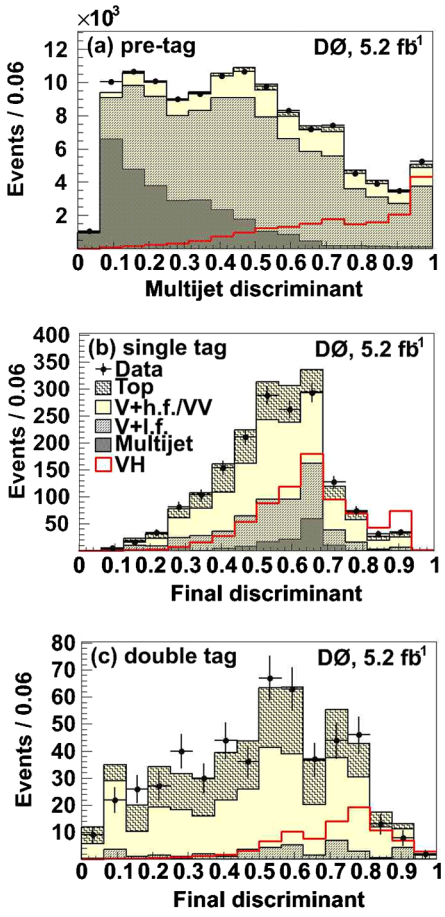

FIG. 60 (color online). The outputs for the (a) MJ BDT, (b) the SM BDT for the single-tagged channel, and (c) the SM BDT for the double-tagged channel for the D0 $VH \to \not{E}_T bb$ analysis.

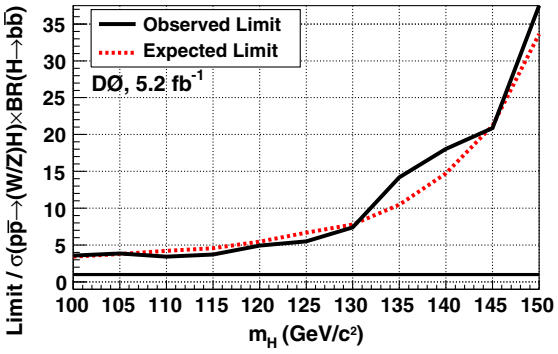

FIG. 61 (color online). The expected and observed 90% C.L. upper bounds on the Higgs-boson production cross section in the D0 $VH \to \not{E}_T bb$ search.

TABLE XXXVIII. Expected and observed yields for the D0 $VH \to \tau\nu bb$ and $VH \to \tau\tau jj$ searches. Only statistical uncertainties are shown.

Source	Search channel $\tau\nu bb$	$\tau\tau jj$
W + lf	0.5 ± 0.0	5.1 ± 0.3
W + hf	10.9 ± 0.3	0.9 ± 0.1
Z + lf	<0.2	43.8 ± 0.6
Z + hf	0.4 ± 0.0	10.1 ± 0.7
$t\bar{t}$	9.5 ± 0.1	2.8 ± 0.0
Diboson	0.7 ± 0.0	2.1 ± 0.2
Multijet	1.3 ± 0.1	6.5 ± 2.8
Total	23.3 ± 0.4	71.2 ± 3.0
Data	13	58
Signal	0.216	0.293

efficiency. These sources have an uncertainty of roughly 5% for each.

4. τ + jets and $\tau\tau$ + jets final states

The searches described earlier for the processes $WH \to \ell\nu bb$ and $ZH \to \ell\ell bb$ required $\ell = e, \mu$, but corresponding channels exist with $\ell = \tau$ leptons in the final state. In addition, $B(H \to \tau\tau) \approx 7\%$ in the SM, the most important mode after $H \to bb$. D0 (Abazov *et al.*, 2009k) published searches for Higgs production in the modes $VH \to \tau bb \to \tau_h \nu$ and $VH \to \tau\tau jj \to \mu\nu\nu_\tau\tau_h jj$, $p\bar{p} \to VVjj \to Hjj \to \tau\tau jj \to \mu\nu\nu_\tau\tau_h jj$, and $gg \to Hjj \to \tau\tau jj \to \mu\nu\nu_\tau\tau_h jj$ using a data sample corresponding to 1.0 fb^{-1}. Here τ_h represents a τ decay to hadrons.

The primary signal contribution to the $\tau\nu\nu bb$ final state comes from $WH \to \tau\nu bb$, but roughly 7% of the final signal acceptance comes from $ZH \to \tau\tau bb$ in which one τ is not identified. The identified τ is required to decay to hadrons (Abazov *et al.*, 2009d). Candidate events are initially selected using a trigger requiring a high p_T jet and large $\not{E}_T$. The offline selection requires a hadronic τ decay, with a minimum transverse energy from 12 to 20 GeV/c, with the range depending on which of two decay topologies the τ lepton is reconstructed. The topologies correspond roughly to single charged-hadron τ lepton decays (type 1) and single charged-hadron with multiple neutral-hadron decays (type 2). In addition to the τ lepton candidate, the basic offline selection requires $\not{E}_T > 30$ GeV, the presence of at least two candidate b jets with $p_T > 20$ GeV/c and $|\eta| < 2.5$, ≤ 3 jets with p_T(GeV/c), and a veto of events with a high-p_T electron or muon to keep orthogonality with the other searches. Events are also required to pass $\Delta\phi(\not{E}_T, \not{T}_T) < \pi/2$, $H_T < 200$ GeV, $50 < M_{JJ} < 200$ GeV/c^2, and $\Delta\phi(\tau, \not{E}_T) < 0.02(\pi - 2)(\not{E}_T - 30) + 2$. In addition, for events with type 2 tau decay, the transverse mass of the $\vec{\tau}$ and $\vec{\not{E}}_T$ must satisfy $M_T < 80$ GeV/c^2.

The $\tau\tau jj$ final-state search has signal contributions from a variety of processes: $ZH \to \tau\tau bb$, $ZH \to q\bar{q}bb$ (in which $H \to \tau\tau$, VBF $p\bar{p} \to VVjj \to Hjj \to \tau\tau jj \to \mu\nu\nu_\tau\tau_h jj$, and gluon fusion $gg \to Hjj \to \tau\tau jj \to \mu\nu\nu_\tau\tau_h jj$). Unlike other low mass channels, some of these processes have no b quarks in the decay chain. Consequently, no b-jet identification is required for this search. One of the τ leptons is required to decay to hadrons, and the other τ lepton is required to decay to a muon. Here three topologies are used. Two of these are the same as in the $\tau\nu bb$ search, and the third corresponds roughly to τ lepton decays to three charged hadrons. Candidate events are initially selected by requiring at least one trigger from a set of single muon and muon plus jet triggers. The initial offline selection requires a muon with $p_T > 12$ GeV/c and $\eta < 2.0$, a hadronic τ lepton decay candidate with a minimum transverse energy from 15 to 20 GeV (again depending on topology) and at least two jets with $p_T > 15$ GeV/c and $\eta| < 2.5$. No b-jet

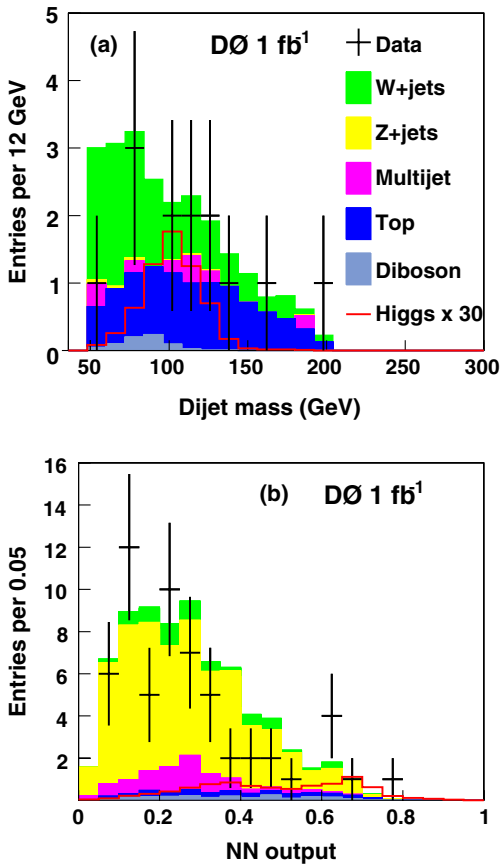

FIG. 62 (color online). (a) The dijet invariant mass distribution for the D0 $VH \to \tau\nu bb$ search, and (b) the NN output for the $VH \to \tau\tau jj$ search.

TABLE XXXIX. Expected and observed 95% C.L. signal cross-section upper limits for the D0 $VH \to \tau\nu bb$ and $VH \to \tau\tau jj$ searches. The limits are given as a ratio of the cross-section limit to the SM cross-section prediction.

	$\tau\nu bb$		$\tau\tau jj$		Combined	
M_H (GeV/c^2)	Exp.	Obs.	Exp.	Obs.	Exp.	Obs.
105	33	27	39	36	24	20
115	42	35	43	47	28	29
125	62	60	60	65	40	44
135	105	106	87	61	63	50

identification is used. Signal and background separation is then improved using a set of neutral networks. A separate neutral network is trained for each of the four signal sources [WH, $ZH(H \to bb)$, $ZH(H \to \tau\tau)$, and VBF], paired with each of the main backgrounds (W + jets, Z + jets, $t\bar{t}$, and multijet). In addition, separate networks are trained for low mass (105, 115, and 125 GeV/c^2) and high mass (135, 145 GeV/c^2) giving a total of 32 networks. Each network uses six or seven input variables chosen such that each one individually improves the $S/\sqrt{B}$ when it is added as the last variable. The same choice of input variables is made at all masses for each signal and background pairing.

All backgrounds except those from multijet events in which jets are misidentified as τ leptons are estimated using simulated events processed through a detailed detector simulation with corrections based on comparison of data and simulated control samples. The absence of electrons and muons from direct W or Z decay results in a significantly higher multijet background in this search than in most. The multijet background is estimated from using a control data sample enriched in τ-like hadronic jet events. Systematic uncertainty sources include trigger efficiency, lepton and jet identification efficiencies, jet energy calibration, and production cross-section uncertainties for backgrounds determined using simulated events.

As for the other analyses, systematic uncertainties are divided into those which affect only normalization and those which affect the shape. Sources affecting the normalization include the integrated luminosity, the trigger efficiency, muon identification efficiency, τ lepton identification efficiency, jet identification efficiency, the τ lepton energy calibration, and background cross sections. The systematic uncertainties which affect the shape for the $\tau\nu bb$ analysis are the jet energy resolutions, the jet energy calibration, and the b-tagging efficiencies. For the $\tau\tau jj$ analysis only the multijet background had a shape dependence. The systematic uncertainties, expressed as a fraction of the related source, range between 3% and 30%. For example, the W + hf cross-section systematic is 30% of the W + hf background, but because the background is roughly 50% of the total background in the $\tau\nu bb$ channel, the effective systematic is roughly 15%.

Predicted background and signal levels and observed yields for the two searches are shown in Table XXXVIII assuming a signal mass of $M_H = 115$ GeV/c^2. The distributions or M_{JJ} and the output from the Z + jets NN NN_Z are used as inputs to the limit setting program for the $\tau\nu bb$ and $\tau\tau jj$ searches, respectively. The distributions are shown in Fig. 62, and the resulting limits are shown in Table XXXIX.

5. $H \to WW^*$

For $m_H \gtrsim 135$ GeV/c^2, the dominant Higgs decay is to W boson pairs. Below the W pair production threshold, one of the W bosons will be off shell which leads to lower p_T leptons from the W^* decay. The most sensitive high mass Higgs channel is $gg \to H \to WW^{(*)} \to \ell\nu\ell\nu$, where the two charged leptons in the final state are of opposite charge. In addition to the dominant ggH process, other Higgs production processes that contribute at the Tevatron are VBF and VH, where $V \equiv (W, Z)$.

Early Tevatron Run II searches for a high mass Higgs boson (Abulencia *et al.*, 2006c; Abazov *et al.*, 2006b) focused mainly on the ggH process and exploiting the angular correlation between final-state charged leptons due to the scalar (spin-0) nature of the SM Higgs. In a more recent analysis (Aaltonen *et al.*, 2009h), CDF used a NN technique to search for a Higgs-boson signal in dilepton + $\not\!\!E_T$ events having either zero or one reconstructed jet. Several kinematic variables, including the results of matrix element calculations that combined charged-lepton and $\not\!\!E_T$ information, were used as inputs to the NN.

The CDF and D0 searches for $H \to WW^{(*)}$ by Aaltonen *et al.* (2010c) and Abazov *et al.* (2010b), respectively, significantly increase their sensitivities compared to previous results through the use of additional data, topologies arising

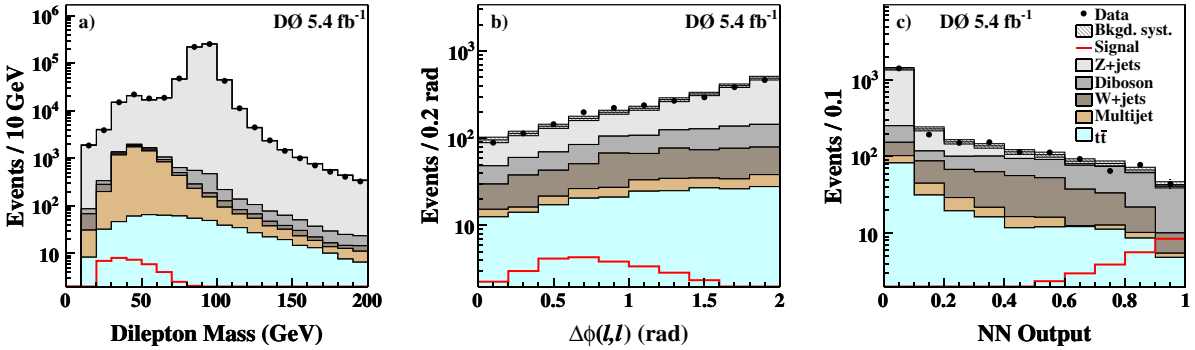

FIG. 63 (color online). For the D0 $H \to WW^{(*)}$ analysis (Abazov *et al.*, 2010b), the (a) dilepton invariant mass after preselection; (b) $\Delta\phi(\ell, \ell)$ angle after final selection; and (c) neural network output after final selection. The signal is shown for $m_H = 165$ GeV. The systematic uncertainty is shown after the fit.

TABLE XL. Expected and observed event yields in each channel after preselection and at the final selection for the D0 $H \to WW^{(*)}$ analysis (Abazov *et al.*, 2010b). The systematic uncertainty after fitting is shown for all samples at final selection.

	$e^{\pm}\mu^{\mp}$		e^+e^-		$\mu^+\mu^-$	
	Preselection	Final selection	Preselection	Final selection	Preselection	Final selection
$Z/\gamma^* \to e^+e^-$	120	<0.1	274 886	158 ± 13	...	...
$Z/\gamma^* \to \mu^+\mu^-$	89	4.3 ± 0.3	...	...	373 582	1247 ± 37
$Z/\gamma^* \to \tau^+\tau^-$	3871	7.1 ± 0.5	1441	0.7 ± 0.1	2659	12.0 ± 0.7
$t\bar{t}$	312	93.8 ± 8.3	159	47.0 ± 4.4	184	74.6 ± 6.8
W + jets/γ	267	112 ± 9	308	122 ± 11	236	91.5 ± 6.5
WW	455	165 ± 6	202	73.9 ± 6.4	272	107 ± 9
WZ	23.6	7.6 ± 0.2	137	11.5 ± 1.0	171	21.5 ± 2.0
ZZ	5.4	0.6 ± 0.1	117	9.3 ± 0.9	147	18.0 ± 1.8
Multijet	430	6.4 ± 2.5	1370	1.0 ± 0.1	408	53.8 ± 10.3
Signal (m_H = 165 GeV)	18.8	13.5 ± 1.5	11.2	7.2 ± 0.8	12.7	9.0 ± 1.0
Total background	5573	397 ± 14	278 620	423 ± 19	377 659	1625 ± 41
Data	5566	390	278 277	421	384 083	1613

from VBF and VH channels, and analysis improvements such as increased charged-lepton acceptance (D0).

In the D0 analysis (Abazov *et al.*, 2010b), an integrated luminosity of 5.4 fb^{-1} is used to search for $H \to WW^{(*)}$ in events with two oppositely charged leptons e^+e^-, $e^{\pm}\mu^{\mp}$, or $\mu^+\mu^-$. Electrons are required to have $|\eta| < 2.5$ (< 2.0 in the e^+e^- channel) and $E_T^e > 15$ GeV. Muons are required to have $|\eta| < 2.0$ and $p_T^{\mu} > 10$ GeV/c (in the $\mu^+\mu^-$ channel, one of the two muons is required to have $p_T^{\mu} > 20$ GeV/c). In addition, the dilepton invariant mass is required to exceed 15 GeV/c^2. Reconstructed jets are required to have $E_T^{\text{jet}} > 15$ GeV and $|\eta| < 2.4$; however, no jet-based event selection is applied since the number of jets in the event is used as input to an NN to help discriminate signal from background. The dilepton invariant mass after this "preselection" is shown in Fig. 63(a).

Additional cuts are made to suppress Z/γ^* production. These include requiring $\not{E}_T > 20$ GeV (> 25 GeV in the $\mu^+\mu^-$ channel), high-quality $\not{E}_T$ measurement, a minimum W transverse mass to be >20 GeV (> 30 GeV in the e^+e^- channel), and azimuthal opening angle between the two leptons $\Delta\phi(\ell, \ell) < 2.0$ rad.

To improve the separation between signal and background, a NN optimized for several m_H values between 115 and 200 GeV/c^2 is used in each of the three channels. Several discriminant variables are used as inputs to the NN: the transverse momenta of the leptons, a variable indicating the quality of the leptons' identification, the transverse momentum and invariant mass of the dilepton system, minimum W transverse mass, $\not{E}_T$, $\not{E}_T$ quality, $\Delta\phi(\ell, \ell)$, $\Delta\phi(\ell_1, \not{E}_T)$, $\Delta\phi(\ell_2, \not{E}_T)$, the number of identified jets, and the scalar sum of the transverse momenta of the jets.

Figure 63 shows the agreement between data and Monte Carlo simulation after final selection for the $\Delta\phi(\ell, \ell)$ angle and the neural network output. The expected and observed event yields are shown in Table XL.

No significant excess of signal-like events is observed for any test value of m_H after the final selection. The NN output distributions are used to set upper limits on the SM Higgs-boson production cross section. Figure 64(a) shows a

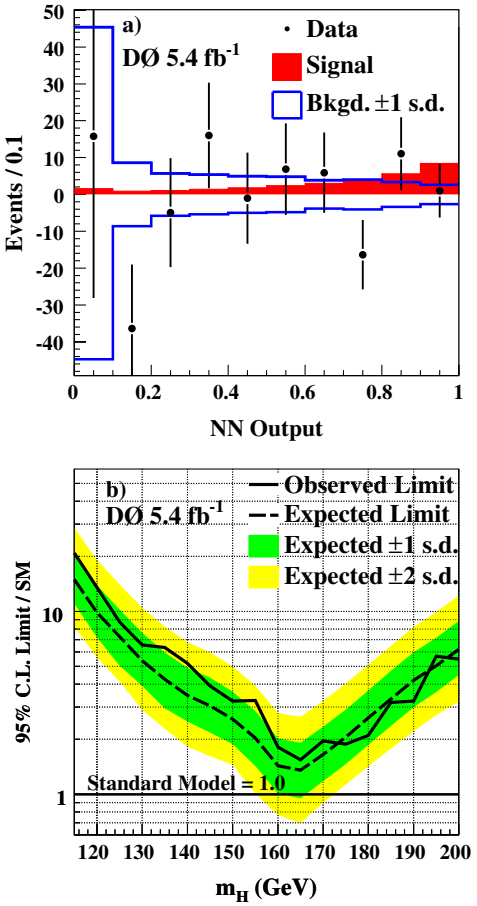

FIG. 64 (color online). For the D0 $H \to WW^{(*)}$ analysis (Abazov *et al.*, 2010b), the (a) data after subtracting the fitted background (points) and SM signal expectation (filled histogram) as a function of the NN output for $m_H = 165$ GeV/c^2. Also shown is the ±1 standard deviation (s.d.) band on the total background after fitting. (b) Upper limit on Higgs-boson production cross section at 95% C.L. expressed as a ratio to the SM cross section. The 1 and 2 s.d. bands around the curve corresponding to the background-only hypothesis are also shown.

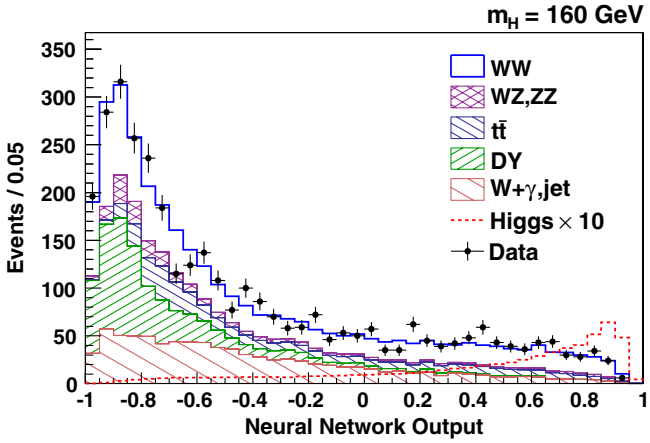

FIG. 65 (color online). The combined distribution of NN scores for backgrounds and a $M_H = 160$ GeV/c^2 Higgs boson compared to the observed data shown with statistical uncertainties for the CDF $H \to WW^{(*)}$ analysis. The Higgs-boson distribution is normalized to 10 times the SM expectation. From Aaltonen *et al.*, 2010c.

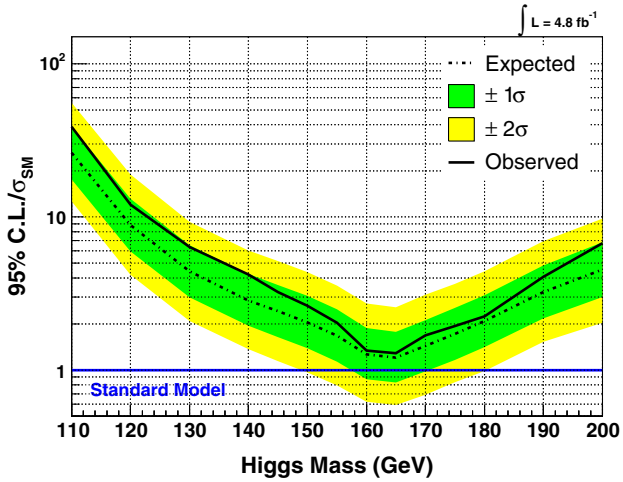

FIG. 66 (color online). Expected and observed upper limits at the 95% C.L. on σ_H presented as a ratio to the predicted SM values as a function of M_H for the CDF $H \to WW^{(*)}$ analysis (Aaltonen *et al.*, 2010c). The dashed line represents the median expected limits, the bands represent the estimated 1σ and 2σ probability bands for the distribution of expectations, and the solid line represents the observed limit.

comparison of the NN distribution between background-subtracted data and the expected signal for $m_H = 165$ GeV/c^2 hypothesis. Figure 64(b) shows the expected and observed upper limits as a ratio to the expected SM cross section. Assuming $m_H = 165$ GeV/c^2, the observed (expected) upper limit at 95% C.L. on Higgs-boson production is a factor of 1.55 (1.36) times the SM cross section.

In the CDF analysis (Aaltonen *et al.*, 2010c), an integrated luminosity of 4.8 fb^{-1} is used to search for $H \to WW^{(*)}$ in events with either an opposite-sign (OS) or same-sign (SS) charged-lepton pair. This is an inclusive search that expands the signal acceptance by 50% for $m_H = 160$ GeV/c^2 compared to searching for only the ggH production process as published previously by CDF (Aaltonen *et al.*, 2009h).

The CDF analysis uses physics objects identified as jets, electrons, and muons as well as the $\not\!\!E_T$ in events. The search is based on the requirement that events contain two charged leptons resulting from the decays of the final-state vector bosons which are OS except in the case of the VH channel where they can be SS. At least one charged lepton is required to match the lepton found in the trigger and have $E_T(p_T) >$ 20 GeV (GeV/c) for electrons (muons). The second charged lepton is required to have $E_T(p_T) > 10$ GeV (GeV/c) except in events with same charge leptons, where both leptons are required to have $E_T(p_T) > 20$ GeV (GeV/c). Requirements on the event $\not\!\!E_T$ indicative of the presence of neutrinos from W boson decay are made in opposite-charge dilepton events. Backgrounds due to Drell-Yan processes and heavy flavor are suppressed by requiring that the invariant mass of the lepton pair be greater than 16 GeV/c^2. The Higgs-boson signature can also involve jets of hadrons produced from the decay of one of the vector bosons in the VH process, forward quarks in the VBF process, or from the radiation of gluons.

In order to increase the sensitivity to the various Higgs production processes in the SM, candidate events are subdivided into six analysis channels based on jet multiplicity, lepton categories, and lepton charge combinations. Five of the channels have signatures with OS leptons and the other is for SS leptons.

Discrimination of signal from background is based on NNs trained in each analysis channel and at each of 14 hypothesized m_H values in the range $110 \le m_H \le 200$ GeV/c^2. The NN inputs are based on kinematic quantities selected to exploit features such as the spin correlation between the W bosons in Higgs-boson decay, the presence of large $\not\!\!E_T$ from the neutrinos; the transverse mass of the Higgs boson (calculated using the leptons' four-momenta and $\not\!\!E_T$ vector); and the modest total energy of the Higgs-boson decay products compared to $t\bar{t}$ decay. In the zero jet categories, we additionally classify events by evaluating the observed kinematic configuration in a likelihood ratio of the signal probability density divided by the sum of the signal and background probability densities. These probability densities are determined from LO matrix element calculations of the cross

TABLE XLI. Expected and observed upper limits at 95% C.L. for Higgs-boson production cross section expressed as a ratio to the cross section predicted by the SM for a range of test Higgs-boson masses.

	m_H (GeV)	120	130	140	145	150	155	160	165	170	175	180	190	200
D0 (Abazov *et al.*, 2010b)	Limit (exp.)	9.74	5.40	3.48	3.07	2.58	2.02	1.43	1.36	1.65	2.06	2.59	4.20	6.23
	Limit (obs.)	13.6	6.63	5.21	3.94	3.29	3.25	1.82	1.55	1.96	1.89	2.11	3.27	5.53
CDF (Aaltonen *et al.*, 2010c)	Limit (exp.)	8.85	4.41	2.85	2.43	2.05	1.67	1.26	1.20	1.44	1.72	2.09	3.24	4.53
	Limit (obs.)	12.04	6.38	4.21	3.23	2.62	2.04	1.34	1.29	1.69	1.94	2.24	4.06	6.74

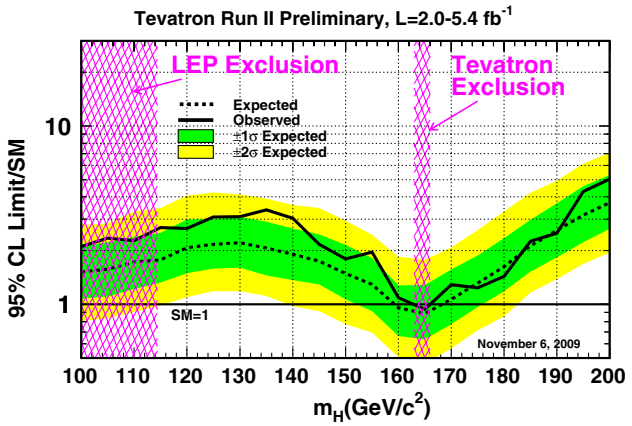

FIG. 67 (color online). The 95% C.L. upper bounds on the Higgs production cross section divided by the predicted cross section. This result includes both published and preliminary results from CDF and D0.

sections of each process (Aaltonen *et al.*, 2009h) (see also Sec. III.E.4 for the case of SM WW).

An example NN discriminant distribution for the combination of all categories is shown in Fig. 65, where signal and background expectations for a 160 GeV$/c^2$ Higgs boson are compared to the observed data.

No significant excess of events beyond SM background expectations in the NN discriminant are observed. The 95% confidence limits on σ_H, expressed as a ratio to the expected SM rate as a function of m_H, are determined from the data. The median expected and observed upper limits on σ_H as a function of m_H are shown in Fig. 66.

The expected and observed upper limits at 95% C.L. for Higgs-boson production cross section expressed as a ratio to the cross section predicted by the SM as a function of m_H for the CDF and D0 searches for $H \to WW^{(*)}$ in Aaltonen *et al.* (2010c) and Abazov *et al.* (2010b), respectively, are shown in Table XLI.

C. Combined limits

Results for individual search final states are combined by the Tevatron New-Phenomena and Higgs Working Group. The combinations are updated roughly every six months to one year using the most up to date preliminary and published results. The combination is performed using a joint probability density incorporating each channel as an individual result with systematic uncertainties and their correlations included. Two algorithms are used for the combination. One is a Bayesian approach (Aaltonen *et al.*, 2010c), and the other is a modified frequentist approach (Junk, 1999; Fisher, 2006). In both algorithms, the impact of systematic uncertainties is reduced by treating these as nuisance parameters. Results for the 95% C.L. upper bound on the Higgs production cross section from the two algorithms agree to within 10%.

The most recent combination (Tevatron Electroweak Working Group, 2009b) incorporates published and preliminary results based on samples ranging from $\int \mathcal{L} dt = 2.1$ to $\int \mathcal{L} dt = 5.4$ fb^{-1}, and combined $H \to WW$ limits are at Aaltonen *et al.* (2010d). The cross-section upper bounds are a factor of 2.7 higher than the SM prediction for $m_H = 115$ GeV$/c^2$ and production of a SM Higgs is excluded at the 95% C.L. in the region $163 < m_H < 166$ GeV$/c^2$. The results are shown in Fig. 67 expressed as a ratio of the 95% C.L. upper bound cross section divided by the SM prediction.

VI. SUMMARY AND OUTLOOK

The SM has been tested extensively over the last 40 years. The only significant deviation from its predictions is the existence of neutrino mass. Ongoing studies of the SM are being carried out by the Tevatron experiments, CDF, and D0. This paper presents results of these tests and discusses prospects for the remainder of the Tevatron running and the transition from the Tevatron to the LHC.

CDF and D0 presented a wide variety of results relating to the EW sector. Among the results are observation of all SM diboson processes involving W, Z, and γ, including for the first time WZ production, observation of EW production of single-top quarks and the corresponding measurement of $|V_{tb}|$, the world's best measurements of the top-quark and W boson masses allowing improved indirect constraints on the Higgs-boson mass, and ongoing searches for the Higgs boson which have begun to exclude mass values outside of the existing limits. In addition to testing the SM, some of these are benchmark measurements eventually to be compared with corresponding results from the LHC. Others, such as the top-quark and W boson masses, are likely to be legacy measurements from the Tevatron.

With additional luminosity still to come for CDF and D0, many of these measurements will significantly improve before the end of Run II at the Tevatron. This is an exciting time in particle physics as the field transitions from the era of the Tevatron to an era of the LHC as the machine to probe physics at the energy frontier.

ACKNOWLEDGMENTS

The many beautiful experimental measurements summarized in this paper are the result of the work of thousands of people from the Fermilab accelerator division, CDF and D0. The authors wish to thank those involved in making these possible. In addition, the authors thank Andrew Askew, Tom Diehl, Reinhard Schwienhorst, and Junjie Zhu for useful discussion and clarification.

REFERENCES

Aaltonen, T, *et al.*, 2007a, Phys. Rev. Lett. **99**, 151801.
Aaltonen, T., *et al.*, 2007a, Phys. Rev. D **76**, 111103.
Aaltonen, T., *et al.*, 2007b, Phys. Rev. D **76**, 072009.
Aaltonen, T., *et al.*, 2007c, Phys. Rev. D **75**, 111103.
Aaltonen, T., *et al.*, 2008a, Phys. Rev. Lett. **100**, 071801.
Aaltonen, T., *et al.*, 2008b, Phys. Rev. Lett. **100**, 201801.
Aaltonen, T., *et al.*, 2008c, Phys. Rev. Lett. **100**, 062005.
Aaltonen, T., *et al.*, 2008d, Phys. Rev. Lett. **101**, 252001.
Aaltonen, T., *et al.*, 2008e, Phys. Rev. D **78**, 032008.
Aaltonen, T., *et al.*, 2008f, Phys. Rev. Lett. **101**, 251803.
Aaltonen, T., *et al.*, 2008g, Phys. Rev. Lett. **100**, 211801.
Aaltonen, T., *et al.*, 2009a, Phys. Rev. Lett. **103**, 091803.
Aaltonen, T., *et al.*, 2009b, Phys. Rev. Lett. **102**, 152001.

Aaltonen, T., *et al.*, 2009c, Phys. Rev. D **79**, 072001.
Aaltonen, T., *et al.*, 2009d, Phys. Rev. D **79**, 092005.
Aaltonen, T., *et al.*, 2009e, Phys. Rev. D **79**, 072005.
Aaltonen, T., *et al.*, 2009f, Phys. Rev. D **79**, 072010.
Aaltonen, T., *et al.*, 2009g, Phys. Rev. D **80**, 012002.
Aaltonen, T., *et al.*, 2009h, Phys. Rev. Lett. **102**, 021802.
Aaltonen, T., *et al.* (CDF), 2009i, Phys. Lett. B **674**, 160.
Aaltonen, T., *et al.*, 2010a, Phys. Rev. Lett. **104**, 201801.
Aaltonen, T., *et al.*, 2010b, Phys. Rev. Lett. **104**, 101801.
Aaltonen, T., *et al.*, 2010c, Phys. Rev. Lett. **104**, 061803.
Aaltonen, T., *et al.*, 2010d, Phys. Rev. Lett. **104**, 061802.
Abachi, S., *et al.*, 1995, Phys. Rev. Lett. **74**, 2632.
Abazov, V. M., *et al.*, 2002a, Phys. Rev. D **66**, 012001.
Abazov, V. M., *et al.*, 2002b, Phys. Rev. D **66**, 032008.
Abazov, V. M., *et al.*, 2005a, Phys. Rev. D **71**, 091108.
Abazov, V. M., *et al.*, 2005b, Phys. Rev. Lett. **94**, 151801.
Abazov, V. M., *et al.*, 2005c, Phys. Rev. Lett. **95**, 141802.
Abazov, V. M., *et al.*, 2006a, Nucl. Instrum. Methods Phys. Res., Sect. A **565**, 463.
Abazov, V. M., *et al.*, 2006b, Phys. Rev. Lett. **96**, 011801.
Abazov, V. M., *et al.*, 2007a, Phys. Lett. B **653**, 378.
Abazov, V. M., *et al.*, 2007b, Phys. Rev. D **76**, 111104.
Abazov, V. M., *et al.*, 2007c, Phys. Rev. D **75**, 092001.
Abazov, V. M., *et al.*, 2007d, Phys. Rev. Lett. **98**, 181802.
Abazov, V. M., *et al.*, 2007e, Phys. Lett. B **655**, 209.
Abazov, V. M., *et al.*, 2008a, Phys. Rev. Lett. **101**, 191801.
Abazov, V. M., *et al.*, 2008b, Phys. Rev. Lett. **100**, 241805.
Abazov, V. M., *et al.*, 2008c, Phys. Rev. Lett. **100**, 131801.
Abazov, V. M., *et al.*, 2008d, Phys. Rev. Lett. **101**, 171803.
Abazov, V. M., *et al.*, 2008e, Phys. Rev. D **78**, 072002.
Abazov, V. M., *et al.*, 2008f, Phys. Rev. Lett. **101**, 182001.
Abazov, V. M., *et al.*, 2008g, Phys. Rev. Lett. **100**, 062004.
Abazov, V. M., *et al.*, 2008h, Phys. Rev. D **78**, 012005.
Abazov, V. M., *et al.*, 2009a, Phys. Rev. Lett. **103**, 141801.
Abazov, V. M., *et al.*, 2009b, Phys. Rev. Lett. **103**, 231802.
Abazov, V. M., *et al.*, 2009c, Nucl. Instrum. Methods Phys. Res., Sect. A **609**, 250.
Abazov, V. M., *et al.*, 2009d, Phys. Rev. Lett. **102**, 201802.
Abazov, V. M., *et al.*, 2009e, Phys. Rev. Lett. **103**, 191801.
Abazov, V. M., *et al.*, 2009f, Phys. Rev. Lett. **102**, 161801.
Abazov, V. M., *et al.*, 2009g, Phys. Rev. D **80**, 053012.
Abazov, V. M., *et al.*, 2009h, arXiv:0907.4952.
Abazov, V. M., *et al.*, 2009i, Phys. Rev. D **80**, 092006.
Abazov, V. M., *et al.*, 2009j, Phys. Rev. Lett. **102**, 051803.
Abazov, V. M., *et al.*, 2009k, Phys. Rev. Lett. **102**, 251801.
Abazov, V. M., *et al.*, 2010a, Phys. Rev. Lett. **104**, 071801.
Abazov, V. M., *et al.*, 2010b, Phys. Rev. Lett. **104**, 061804.
Abbiendi, G., *et al.*, 2006a, Eur. Phys. J. C **45**, 307.
Abbiendi, G. P., *et al.* (The ALEPH, DELPHI, L3, OPAL, SLD Collaborations, the LEP Electroweak Working Group, the SLD Electroweak and Heavy Flavour Groups), 2006b, Phys. Rep. **427**, 257.
Abbott, B., *et al.*, 1998, Phys. Rev. Lett. **80**, 2063.
Abbott, B., *et al.*, 1999, Phys. Rev. D **60**, 052001.
Abdallah, J., *et al.*, 2008, Eur. Phys. J. C **55**, 1.
Abe, F., *et al.*, 1995, Phys. Rev. Lett. **74**, 2626.
Abe, F., *et al.*, 1997, Phys. Rev. Lett. **78**, 4536.
Abulencia, A., *et al.*, 2006a, Phys. Rev. Lett. **96**, 022004.
Abulencia, A., *et al.*, 2006b, Phys. Rev. D **74**, 072006.
Abulencia, A., *et al.*, 2006c, Phys. Rev. Lett. **97**, 081802.
Abulencia, A., *et al.*, 2007a, J. Phys. G **34**, 2457.
Abulencia, A., *et al.*, 2007b, Phys. Rev. Lett. **98**, 161801.
Abulencia, A., *et al.*, 2007c, Phys. Rev. D **75**, 031105.
Abulencia, A., *et al.*, 2007d, Phys. Rev. D **75**, 071102.
Achard, P., *et al.*, 2006, Eur. Phys. J. C **45**, 569.
Acosta, D., *et al.*, 2005a, Phys. Rev. D **71**, 052002.
Acosta, D., *et al.*, 2005b, Phys. Rev. Lett. **94**, 041803.
Acosta, D., *et al.*, 2005c, Phys. Rev. Lett. **94**, 211801.
Acosta, D., *et al.*, 2005d, Phys. Rev. Lett. **94**, 091803.
Acosta, D., *et al.*, 2005e, Phys. Rev. D **71**, 052003.
Affolder, A., *et al.*, 2001, Phys. Rev. D **64**, 052001.
Affolder, T., *et al.*, 2000, Phys. Rev. Lett. **85**, 3347.
Alcaraz, J., *et al.*, 2006, arXiv:hep-ex/0612034.
Alcaraz, J., *et al.*, 2009, arXiv:0911.2604.
Amsler, C., *et al.*, 2008, Phys. Lett. B **667**, 1.
Arnison, G., *et al.*, 1983a, Phys. Lett. B **122**, 103.
Arnison, G., *et al.*, 1983b, Phys. Lett. B **126**, 398.
Bagnaia, P., *et al.*, 1983, Phys. Lett. B **129**, 130.
Banner, M., *et al.*, 1983, Phys. Lett. B **122**, 476.
Baur, U., and E. L. Berger, 1990, Phys. Rev. D **41**, 1476.
Baur, U., and E. L. Berger, 1993, Phys. Rev. D **47**, 4889.
Baur, U., S. Errede, and G. L. Landsberg, 1994, Phys. Rev. D **50**, 1917.
Baur, U., T. Han, and J. Ohnemus, 1993, Phys. Rev. D **48**, 5140.
Baur, U., T. Han, and J. Ohnemus, 1998, Phys. Rev. D **57**, 2823.
Baur, U., and D. L. Rainwater, 2000, Phys. Rev. D **62**, 113011.
Baur, U., and D. Zeppenfeld, 1988, Phys. Lett. B **201**, 383.
Breiman, L., 2001, Mach. Learn. **45**, 5.
Brodsky, S., and R. Brown, 1982, Phys. Rev. Lett. **49**, 966.
Brown, R. W., D. Sahdev, and K. O. Mikaelian, 1979, Phys. Rev. D **20**, 1164.
Buchmuller, W., and D. Wyler, 1986, Nucl. Phys. B **268**, 621.
Cacciari, M., *et al.*, 2008, J. High Energy Phys. 09, 127.
Campbell, J., R. K. Ellis, and F. Tramontano, 2004, Phys. Rev. D **70**, 094012.
Campbell, J., R. Frederix, F. Maltoni, and F. Tramontano, 2009, Phys. Rev. Lett. **102**, 182003.
Campbell, J. M., and R. K. Ellis, 1999, Phys. Rev. D **60**, 113006.
Cao, Q.-H., R. Schwienhorst, J. A. Benitez, R. Brock, and C.-P. Yuan, 2005, Phys. Rev. D **72**, 094027.
Cao, Q.-H., R. Schwienhorst, and C.-P. Yuan, 2005, Phys. Rev. D **71**, 054023.
Cho, P., and M. Misiak, 1994, Phys. Rev. D **49**, 5894.
Cortese, S., and R. Petronzio, 1991, Phys. Lett. B **253**, 494.
Dalitz, R., and G. Goldstein, 1992, Phys. Rev. D **45**, 1531.
De Rujula, A., M. B. Gavela, P. Hernandez, and E. Masso, 1992, Nucl. Phys. B **384**, 3.
Djouadi, A., 2008, Phys. Rep. **457**, 1.
El-Khadra, A. X., and M. Luke, 2002, Annu. Rev. Nucl. Part. Sci. **52**, 201.
Ellis, K., and S. Parke, 1992, Phys. Rev. D **46**, 3785.
Fisher, W., 2006, Report No. FERMILAB-TM-2386-E.
Frixione, S., E. Laenen, P. Motylinski, and B. R. Webber, 2006, J. High Energy Phys. 03, 092.
Fujikawa, K., and A. Yamada, 1994, Phys. Rev. D **49**, 5890.
Goebel, C. J., F. Halzen, and J. P. Leveille, 1981, Phys. Rev. D **23**, 2682.
Hagiwara, K., S. Ishihara, R. Szalapski, and D. Zeppenfeld, 1993, Phys. Rev. D **48**, 2182.
Hagiwara, K., R. D. Peccei, D. Zeppenfeld, and K. Hikasa, 1987, Nucl. Phys. B **282**, 253.
Hagiwara, K., J. Woodside, and D. Zeppenfeld, 1990, Phys. Rev. D **41**, 2113.
Hamberg, R., W. L. van Neerven, and T. Matsuura, 1991, Nucl. Phys. B **359**, 343.
Han, T., A. S. Turcot, and R.-J. Zhang, 1999, Phys. Rev. D **59**, 093001.
Han, T., and R.-J. Zhang, 1999, Phys. Rev. Lett. **82**, 25.

Harris, B., E. Laenen, L. Phaf, Z. Sullivan, and S. Weinzierl, 2002, Phys. Rev. D **66**, 054024.
Heinson, A. P., *et al.*, 1997, Phys. Rev. D **56**, 3114.
Junk, T., 1999, Nucl. Instrum. Methods Phys. Res., Sect. A **434**, 435.
Kidonakis, N., 2006, Phys. Rev. D **74**, 114012.
Kober, M., B. Koch, and M. Bleicher, 2007, Phys. Rev. D **76**, 125001.
Kondo, K., 1988, J. Phys. Soc. Jpn. **57**, 4126.
Kondo, K., 1991, J. Phys. Soc. Jpn. **60**, 836.
Langenfeld, U., S. Moch, and P. Uwer, 2009, Phys. Rev. D **80**, 054009.
Luscher, M., and P. Weisz, 1988, Phys. Lett. B **212**, 472.
Lyons, L., D. Gibaut, and P. Clifford, 1988, Nucl. Instrum. Methods Phys. Res., Sect. A **270**, 110.
Mangano, M. L., M. Moretti, F. Piccinini, R. Pittau, and P. Polosa, 2003, J. High Energy Phys. 07, 001.
Martin, A. D., R. G. Roberts, W. J. Sterling, and R. S. Thorne, 2004, Phys. Lett. B **604**, 61.
Mikaelian, K. O., M. A. Samuel, and D. Sahdev, 1979, Phys. Rev. Lett. **43**, 746.
Pumplin, J., *et al.*, 2002, J. High Energy Phys. 07, 012.
Quigg, C., 2009, Annu. Rev. Nucl. Part. Sci. **59**, 505.
Read, A. L., 2002, J. Phys. G **28**, 2693.
Rosner, J., M. Worah, and T. Takeuchi, 1994, Phys. Rev. D **49**, 1363.
Scanlon, T., 2006, Report No. FERMILAB-THESIS-2006-43.
Schael, S., *et al.*, 2006, Eur. Phys. J. C **47**, 309.
Sirlin, A., 1980, Phys. Rev. D **22**, 971.
Sjostrand, T., *et al.*, 2001, Comput. Phys. Commun. **135**, 238.
Smith, M., and S. Willenbrock, 1996, Phys. Rev. D **54**, 6696.
Smith, M., and S. Willenbrock, 1997, Phys. Rev. Lett. **79**, 3825.
Stange, A., W. J. Marciano, and S. Willenbrock, 1994a, Phys. Rev. D **49**, 1354.
Stange, A., W. J. Marciano, and S. Willenbrock, 1994b, Phys. Rev. D **50**, 4491.
Stelzer, T., Z. Sullivan, and S. Willenbrock, 1997, Phys. Rev. D **56**, 5919.
Stelzer, T., and S. Willenbrock, 1995, Phys. Lett. B **357**, 125.
Sullivan, Z., 2004, Phys. Rev. D **70**, 114012.
Tevatron New-Phenomena and Higgs Working Group, 2009, arXiv:0911.3930.
Tevatron Electroweak Working Group (CDF and D0 Collaborations), 2009a, arXiv:0908.2171.
Tevatron Electroweak Working Group, 2009b, arXiv:0908.1374.
Tevatron Electroweak Working Group, 2009c, arXiv:0903.2503.
Valassi, A., 2003, Nucl. Instrum. Methods Phys. Res., Sect. A **500**, 391.
Weinberg, S., 1979, Phys. Rev. Lett. **43**, 1566.
Willenbrock, S., and D. Dicus, 1986, Phys. Rev. D **34**, 155.
Yuan, C. P., 1990, Phys. Rev. D **41**, 42.
Zeller, G. P., *et al.*, 2002, Phys. Rev. Lett. **88**, 091802.
Zeppenfeld, D., and S. Willenbrock, 1988, Phys. Rev. D **37**, 1775.